THE ESTABLISHMENT, CHARACTERIZATION, AND USE OF A ROTATING

ELECTRODE SYSTEM FOR THE GENERATION OF URANIUM ALLOY

MICROSPHERES

A Thesis

by

DANIEL WALTER GALICKI

Submitted to the Office of Graduate and Professional Studies of
Texas A&M University
in partial fulfillment of the requirements for the degree of

MASTER OF SCIENCE

Chair of Committee,	Sean M. McDeavitt
Committee Members,	Lin Shao
	Raymundo Arroyave
Head of Department,	Yassin A. Hassan

December 2014

Major Subject: Nuclear Engineering

ABSTRACT

Various proposed metallic nuclear fuel designs for fast reactors may require powder fabrication methods and the reactive nature of uranium metal creates unique challenges. Spherical powder is desired in some fuel concepts over flaky or irregular powder because it will enable predictable packing fractions, even for low density fuels. A previously-established method for powder production is the Rotating Electrode Process (REP) which produces microsphere shaped powder by melting the tip of a rotating cylinder via electric arc. As droplets of molten metal are expelled radially outward, they solidify into spherical particles. A new REP system, named the TAMU Rotating Electrode System (TAMU RES), was developed at Texas A&M University in a previous study. This RES apparatus was placed inside of an inert atmosphere glovebox for this present study to enable uranium powder manufacture. The RES is based on previous designs by Starmet Co. and the Idaho National Laboratory (INL). It is capable of melting a metal rod up to 12.7 cm (5 inches) in length and 1.27 cm (0.5 inches) in diameter as it rotates up to 19,000 RPM. The RES is capable of operating at speeds up to 40,000 RPM provided no mechanical instabilities are present in the rotating cylinder. Varying the RPM alters the diameter of the spheres produced in a predictable fashion, but in a manner that is unique to each material melted by the RES.

The RES is capable of producing repeatable powder size distributions. Copper, depleted uranium (DU), and U-10 wt% Zr (U-10Zr) powders were produced using the RES and their size distributions were characterized as a function of RPM for rotational speeds varying between 10,000 and 19,000 RPM. The copper powders were produced in both air and argon atmospheres, while the uranium and U-10Zr powders were produced under an argon atmosphere to prevent oxidation of the microspheres. Problems and areas of concern

like material flaking and rotational instability issues were overcome by the installation of a helium cooling line inside the catch pan, and by selecting mechanically straight rods for melting. Continued characterization work of powders produced by the RES is also addressed.

DEDICATION

I dedicate this thesis to my future children. Dear future children, please do not read this manuscript in its entirety. There are absolutely no secret messages hidden within the text that will most certainly begin you on a grand adventure. It would be absurd to think that your dear old dad led anything other than a modest, normal life during his college years. Please pay no attention to the spike in mysterious reports filed with the authorities between 2008 and 2014. What does it matter that they correspond exactly with the six years your dad was enrolled here? It means nothing future children of mine. Oh, and don't even think of printing out these pages to ceremoniously burn them in an attempt to use the ashes to summon my undead spirit from the grave. I wouldn't hear of it! It simply shouldn't be tried.

Enjoy your dedication O future children. Before reading on, it occurs to me that it would not be untoward of you to pack a small travel bag with all the essentials: toothbrush, toothpaste, thick socks, a towel, maybe a few torches, hunting knife, medical supplies… You know. The usual. It's up to you. Probably nothing will happen anyway.

ACKNOWLEDGEMENTS

NOMENCLATURE

BCC	Body Centered Cubic
BOL	Beginning Of Life
DU	Depleted Uranium
EBR	Experimental Breeder Reactor
FCCI	Fuel Clad Chemical Interaction
FCMI	Fuel Clad Mechanical Interaction
FCML	Fuel Cycle and Materials Laboratory
FIMA	Fissions per Initial Metal Atom
FNPT	Female National Pipe Thread
INL	Idaho National Laboratory
PPE	Personal Protection Equipment
REP	Rotating Electrode Process
RES	Rotating Electrode System
RPM	Rotations Per Minute
SFP	Solid Fission Product
TAMU	Texas A&M University
TWR	Traveling Wave Reactor
VFD	Variable Frequency Drive
XRD	X-Ray Diffraction

TABLE OF CONTENTS

LIST OF FIGURES

x

xi

LIST OF TABLES

1. INTRODUCTION

The motivation for and scope of the experiments performed using the Fuel Cycle and Materials Laboratory (FCML) Rotating Electrode System (RES) are summarized in this chapter. The objectives of the work reported here were to 1) establish the existing RES [1] in an inert atmosphere glovebox (with some modification), 2) use the inert atmosphere RES to create copper, depleted uranium (DU), and uranium-10 wt% zirconium (U-10Zr) microspheres, and 3) the characterization of the resulting powders. Section 1.1 presents a brief description of the background context for pursuing powder fuel. Section 1.2 introduces the scope of experiments involved in characterizing the RES and analysis of the powder produced by the Rotating Electrode Process (REP).

1.1   Motivation

TerraPower LLC is currently designing a fast spectrum nuclear reactor called the Traveling Wave Reactor (TWR) wherein the fuel for sustained operation is created *in situ* during the reactor's operation. The objective is to develop a reactor that is capable of producing power for up to 40 years without the need to refuel and without the need to have a regular enrichment infrastructure [2]. Current Pressurized Water Reactors (PWR) and Boiling Water Reactors (BWR) require a re-fueling outage every 18-24 months and fuel enrichments that range from 3 to 5 atom percent U-235. The ultra-long lifetime of the TWR would mitigate the need for lengthy refueling outages but the system will depend on a novel nuclear fuel concept optimized for high burn up. The long fuel residence time also creates material degradation challenges.

One of the most desired characteristic for any nuclear fuel element is its ability to achieve high burn-up without failure. This extends the life of the fuel element and reduces waste, which make the fuel more economical to both produce and dispose of. Because of their high fissile/fertile atomic densities, metallic fuels are capable of satisfying this high burn-up requirement and possess additional characteristics which continue to garner attention. Metallic fuels typically have good thermal conductivity, breeding potential, and are easier to reprocess [3, 4]. However, early metallic fuels were not seriously considered for fast reactor, high-burnup designs because of their anisotropic swelling and fission gas build up, both of which caused cladding rupture at relatively low burn-up percentages [4].

It has been calculated that fuel for the TWR would need to achieve a burn up of at least 20% fissions per initial metal atom (FIMA) in order to achieve its long lifetime, no re-fuel, and power production goals [5]. The only experimental fuel type to have achieved this kind of high burn up was the U-10Zr fuel used in the Experimental Breeder Reactor-II (EBR-II) from 1964 until its shutdown in 1994 [6]. Due mainly to its favorable properties at very high burn up, current research points to metal U-Zr alloys, especially for Zr contents at or below 10 wt. %, as the front runner fuel for the TWR [2]. Alloying uranium with zirconium increases its melting temperature and lowers the temperature of the BCC gamma phase boundary of uranium. Both of these effects allow for larger safety margins during reactor operation, and operating in an isotropic phase ensures that any swelling that occurs in the fuel is isotropic [3]. Zirconium in particular has the added benefit of reducing inter-diffusion between cladding and fuel elements. Walters et al have performed a comprehensive review of the various metallic fuels developed and studied in the EBR I and EBR II reactors, from 1951 through the late 1970's [4].

2

Two major hindrances when attempting to reach high burn-ups in metallic fuels are the fuel-clad mechanical interactions (FCMI) and the fuel-clad chemical interactions (FCCI) between the fuel and the cladding material. Solid fission products (SFP) tend to migrate to the periphery of the fuel element and react with the cladding material chemically, while gaseous fission products interact with defects in the fuel's atomic structure and gather to create bubbles. These bubbles dominate fuel swelling and induce mechanical stress on the cladding at low burn-ups (1-2 atomic %). It was previously mentioned that alloying uranium with zirconium helped reduce the chemical interaction between the cladding and solid fission products. It was discovered in 1973 that reducing the smear density of a metallic fuel element from 85% to 75% allowed the fuel to achieve higher burn-ups before rupture occurred (smear density is defined as the percent of a volume occupied by the fuel [7]). A 75% smear density allowed the fuel element to expand by 35%. This expansion allowed for fission-gas bubbles within the fuel to interconnect and eventually escape from the fuel, rather than be trapped in high pressure bubbles. The resulting porous fuel could be easily constrained by the cladding [8]. Solid fission product swelling has been viewed as negligible in commercial oxide system that only reach 3 to 6 atom % burnup (or, 30 to 60 GWd/MT). However, the loose correlation for this type of swelling is a volumetric strain of about 1.0 to 1.5 % per atom percent burnup [9]. The TWR design is targetin burnups significantly higher than those previously achieved with metallic fuels; this puts SFP swelling into an undocumented regime that could include phase changes, restructuring, and unforeseen metallurgical reactions.

In addition to (and somewhat exacerbated by) swelling, fuel cladding mechanical and chemical interactions will be limiting challenges. At elevated temperatures and high pressures, fuel clad chemical interactions (FCCI) and fuel clad mechanical interactions

(FCMI) can occur. These chemical reactions occur between the cladding and the fuel or its fission products. Some of the reactions, such as eutectics formed with rare earth fission products, are very deleterious to the cladding material and are only enhanced by physical pressing of the fuel against the clad.

With all of these challenges, the establishment of a low smear density fuel has been considered for the beginning of life (BOL) of the TWR [10]. Multiple means are possible to generate such a low density fuel form, but one potential design concept comprises the packing of microspheres in a relatively low density fuel form [11]. The RES and the work presented below were intended to assist in the evaluation of the properties associated with low density nuclear fuel. Challenges associated with the performance of packed spheres makes the implementation of a packed bed of microspheres an unlikely fuel form but the powders that can be produced by the RES may be useful for further experiments.

1.2   Experiment Scope & Procedure

The objectives of the present study were to establish the existing TAMU RES [1] in an inert atmosphere glovebox, use the inert atmosphere RES to create copper, uranium, and uranium-10 wt% zirconium (U-10Zr) microspheres, and to characterize the resulting powders. A complete characterization of U-Zr powder produced using the REP does not exist in current literature. However, the laboratory scale fuel atomizer and researchers at the Idaho National Laboratories (INL) did partially characterize alloys of U-Mo and the Starmet Corporation has melted pure uranium using the REP [12]. For these reasons and for its low cost and ease of use, the rotating electrode process was chosen to produce uranium alloy powder over other types of atomizing processes.

4

During the rotating electrode process, a metal alloy rod is rotated at high RPM and melted at one end by a heat source, typically a weld type electrode or plasma. The molten metal formed during the melting process is cast radially away from the rod where surface tension forces re-form the metal droplet into a sphere before it solidifies and is collected. In this study, powder from the RES was collected and filtered into sixteen size groups using fifteen wire mesh sieves. The filtered powder was then viewed under a digital microscope, and in the case of copper powder, analyzed by X-ray diffraction (XRD) techniques. Figure 1-1 depicts the TAMU RES established in an argon atmosphere glovebox.
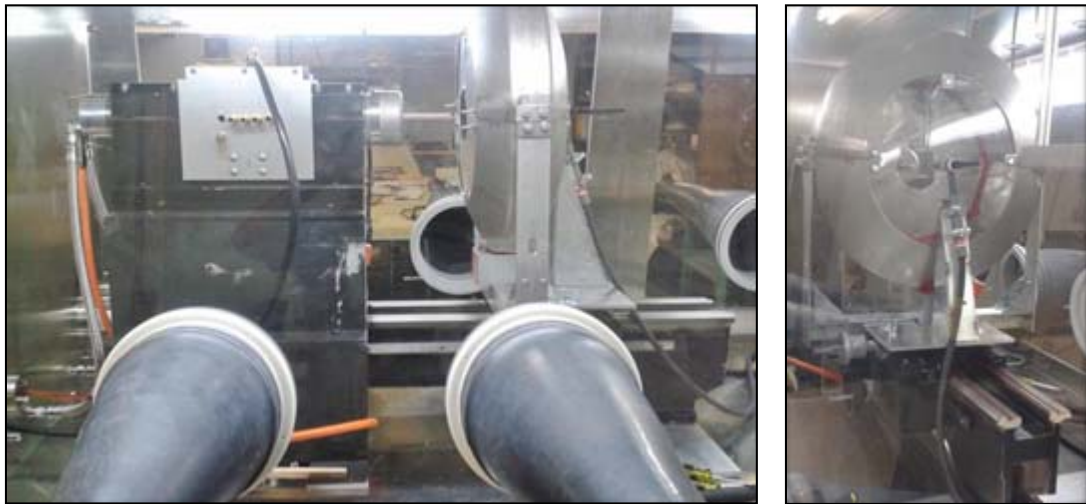
Figure 1-1: The established TAMU RES in an argon environment glovebox

Copper, uranium, and U-10Zr spherical powders were generated and their sizes and morphology characterized as a function of rotational speed. Typically, each test of the RES produced 30 grams of powder on average. All three metals exhibited bi-modal size distributions at all rotational speeds. Higher rotational speeds corresponded to greater mass percentages of the smaller diameter peak size, and reduced mass percentages of the larger

diameter peak size. Copper and uranium microspheres exhibited very smooth surfaces, while U-10Zr exhibited a rougher surface. Copper spheres were analyzed by x-ray diffraction and were found to be crystalline in structure with no amorphization. Uranium and U-10Zr spheres were polished and observed under a digital microscope. No internal voids were found in either the uranium or the U-10Zr spheres.

Overall, the TAMU RES proved to be a reliable method for producing clean, highly spherical metal powder. The argon atmosphere and contactless melting method ensured no oxidation from the environment and no contamination during the melt process. Contactless melting is highly desirable when melting reactive materials like uranium or zirconium. During this study, the TAMU RES was limited in the maximum rotational speed that could be achieved (19,000 RPM). This limit is attributed to mechanical instabilities of the rotating electrode, i.e. the "straightness" of the rod, and of the stainless steel slip ring that connects the two spindles in the system. With mechanically straight feed rods and a balanced slip ring, the RES is capable of rotating at up to 40,000 RPM [1]. Loss of powder was also encountered during the collection and filtering phase of the powder producing using the RES. It is not known what sizes of powder were lost during this process, only the final mass difference between the filtered powder groups and the metal rod before melting. The largest of these losses for each material were 2.7% for copper, 2.1% for uranium, and 1.8% for U-10Zr.

An outline describing the rest of this document is provided here. Chapter 2 contains background information on past methods of metal powder generation and the theory behind centrifugal atomization techniques, as well as past work and results from literature when using the rotating electrode process. Chapter 3 describes the experiment design set up and

introduces the procedures used during the production and characterization of the metal powder produced by the RES. Chapters 4-5 present and discuss the results of the rotating electrode experiments, and chapter 6 provides a document summary.

2.   BACKGROUND

As noted above, this document describes the installation and operation of a rotating electrode system for metal powder production. The sections in this chapter review properties and literature reports relevant to this work. Section 2.1 summarizes the relevant material properties for the metals used in this work. Section 2.2 provides a review of various powder production processes; Section 2.3 provides a review of previous studies conducted using the RES methodology.

2.1   Metal Properties for RES Studies

This section describes the basic properties and phase description of each metal used in the study (Cu, U, and U-10Zr). The relevant properties include the melting/solidus temperature, the thermal conductivity/diffusivity, the liquid density at melting, and surface tension of the liquid metal. The melting temperature and thermal conductivity correlate to the amperage needed to melt the spinning electrode. The liquid density and surface tension of the liquid metal at melting are necessary to predict the average particle size produced by the RES. More discussion of these processes is given in sections 2.2.3.2 and 3.1.2. A table comparing the relevant property values is given below. Although values for the liquid density and surface tension of U-10Zr were not found, it is thought that the liquid density value is between 13-14 g/cm^3 based on an assumed correlation between the density drop from solid to liquid uranium and the solid U-10Zr density literature value of 15.5 g/cm^3.

Table 2-1: Properties of Cu, U, and U-10Zr

	Melting Temperature (ºK)	Thermal Conductivity (W/m/K)	Liquid Density (g/cm³)	Surface Tension (N/m)
Copper	1356 [13]	385	7.99 [13]	1.31 [14]
Uranium	1406 [15]	27.5	17.27 [16]	1.55 [15]
U-10Zr	1433 [17]	18-19	-	-

A discussion of the phase changes inherent in each of the materials used in this study is important to understand what sorts of microstructure results may be seen as a result of the rotating electrode process. Pure copper has only one solid phase from room temperature to melting and its atoms are arranged in the face centered cubic structure (FCC). Thus, the only two options when considering the microstructure of post REP copper are FCC or amorphous, where the atoms do not show any structured organization.

Pure uranium assumes three different solid phases (α, β, and γ) as it is heated from room temperature to its melting point. Uranium's alpha phase assumes an orthorhombic crystal structure with four atoms per unit cell from room temperature to 660ºC. Uranium's beta phase assumes a tetragonal crystal structure with thirty atoms per unit cell from 660ºC to 670ºC. Uranium's gamma phase assumes a body centered cubic (BCC) crystal structure with three atoms per unit cell from 670ºC to the melting point [18].

The U-Zr phase diagram as it is currently understood is shown in Figure 2-1 with the U-10Zr line highlighted. U-10Zr is stable below 617°C in the α + δ phase (α-Uranium plus stable UZr$_2$) and exists as a BCC solid solution above 693°C in the γ-phase (γ-Uranium plus β-Zirconium) [19].
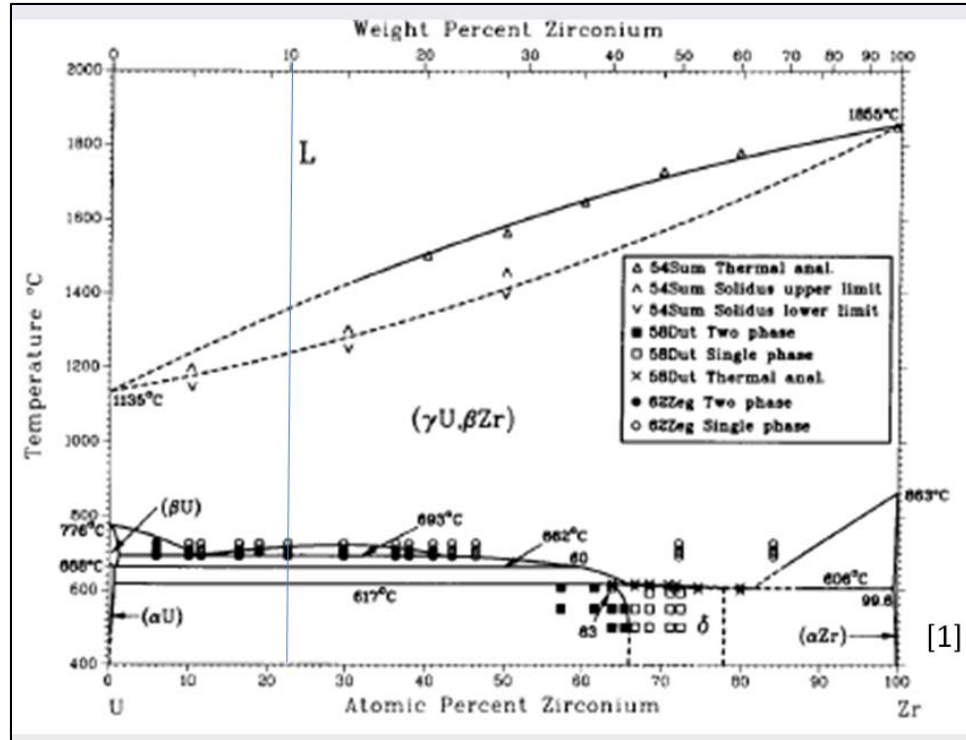
Figure 2-1: The U-Zr system phase diagram [20]

2.2   Metal Powder Production

The rotating electrode system established for this project is one of many possible powder fabrication technologies available. As noted above, the RES method was selected for uranium alloy fabrication to enable further experimental studies of thermal and creep properties.   Metal powder may be manufactured by chemical, comminution, electrolysis, and

atomization methods. These various methods have advantages and disadvantages that may influence the size, shape, and/or quality of the powder produced as well as the cost. Powder metallurgy is a desirable cost-saving method that can enable near net shape fabrication and the creation of parts using uniquely manufactured powders when creating components that have specific microstructures, or when there is no other viable way to manufacture a component, i.e. a "captive" reason [21].

Components that require unusual composition or specific microstructures may be readily produced by sintering powder. An example of this would be U-10Zr nuclear fuel which theoretically requires a smear density of 75% to allow for swelling to occur within the component during use without dimensional changes. Casted U-10Zr has a density of 15.8 g/cm^3 but a fuel element with 75% smear density has density of 11.85 g/cm^3 [19]. This can be achieved by controlling the sintering process of a U-10Zr powder into the final fuel shape.

Some components must be fabricated via powder sintering because there is no other viable method of production. These products are typically reactive or refractory metals which are difficult to manufacture using ordinary metal casting methods [21]. Zirconium is an example of a metal that exhibits extreme reactivity in its molten state, reacting with oxygen in the air or even its melting crucible [22]. Zirconium powder can be pressed and sintered at a much lower temperature, decreasing the reactivity with its surroundings.

The following sections provide a review of powder fabrication methods for comparative purposes only.

2.2.1 Powder Fabrication via Mechanical Techniques

Mechanical comminution involves the reduction in average particle size of solids through mechanical methods like grinding, crushing, and shearing. These methods create very rough, irregularly-shaped powders with a relatively broad particle size distribution. An impaction mill, or rolling mill, is one of the simplest methods available and it uses hard, tough impacting balls inside of a rotating container; the rolling and falling motion inside of the mill chamber crush larger particles into smaller particles. This method can produce powder of irregular size and shape and often contaminates the ground material with constituents from the grinding media and the container walls.

Shearing is usually achieved using a machining tool like a lathe or drill press. The source material is cut by a rotating bit and the scrap produced is collected as a powder. Often, this form of powder production needs further milling in order to be useful.

Compaction is similar to impaction methods, but requires only a crushing force and a brittle material. Like impaction, this form of powder fabrication works only on brittle material and creates a powder of irregular shape and size.

2.2.2 Powder Fabrication via Chemical Techniques

Many metal powders are created using chemical processing pathways. The size of the powder produced by chemical reactions may be tightly controlled and the shape of the powder may also be controlled to a certain extent. Common chemical methods include the decomposition of a solid with a gas (oxide reduction), thermal decomposition, precipitation from a liquid/gas, and solid-solid reactive synthesis [21]. In solid decomposition, an oxide powder is reduced via a thermochemical reaction with a reducing agent such as hydrogen or

carbon monoxide. The reducing agent consumes oxygen from the powder, reducing the oxide to its pure metal component. This method reduces the size of the powder but does not change the shape, and porosity is sometimes introduced into the powder.

Thermal decomposition normally produces powder by flowing a reactive precursor gas over the material to be made into powder, creating a metal-carrying gas molecule. The gas is then thermally decomposed and the metal component is separated from the carrier gas using fractional distillation. The resulting mixture is re-heated to remove the carrier gas and cooled again. As the final gas is cooled, metal nucleates out and is left in powder form [21].

Very small and very pure metal powder may also be produced by precipitating metal out of a liquid or gas. Precipitating from a liquid generally involves dissolving the metal into a salt then dissolving the salt in water. A second compound is mixed in to remove the salt and metal powder is precipitated. Powder produced by this method is typically on the order of 1-10 µm in size and irregularly shaped. Precipitating from a gas is expensive but can yield nanoscale powder. After the desired metal is reacted with a precursor carrier gas, it is vapor distilled and then energetically precipitated using an electron beam, laser, or induction field. The shape of the powder precipitated in this way can be somewhat controlled to be uniform.

Finally, fabricating powder using solid-solid reactive synthesis simply means allowing two different constituents of an alloy, in powder form, to react by adding heat, creating a more thermodynamically stable product. This method produces alloys without melting and must be re-milled into a powder [21].

2.2.3   Powder Fabrication via Mechanical Techniques

The system under study in this present work comprises the atomization of uranium metal and its alloys into spherical powder via a centrifugal melt method. As stated in Chapter 1, the program objective was to create a method for the fabrication of spherical powder to contribute to follow-on activities regarding uranium fuel fabrication and performance. Spherical powder is desirable because of its superior flow and packing properties. This section presents an overview of several atomization methods. The discussion starts with a brief description of gas and liquid atomization methods that were not selected for this work and is followed by a more detailed description of the rotating electrode method.

2.2.3.1   *Gas/Liquid Jet Atomization*

Gas-driven and liquid-driven atomization methods are similar processes. In both cases, a molten pool of the metal to be atomized is prepared, typically by induction melting, and a molten stream is injected through an atomization nozzle. Within this nozzle, impinging jets of either inert gas or liquid break up the stream. This process creates a steady flow of individual droplets which are driven by surface tension forces to form metal spheres. Figure 2-2 depicts a close up schematic view of this type of atomization process. Powder morphology may be controlled by varying the melt temperature, gas/liquid type, gas/liquid velocity, nozzle design, and metal feed rate.
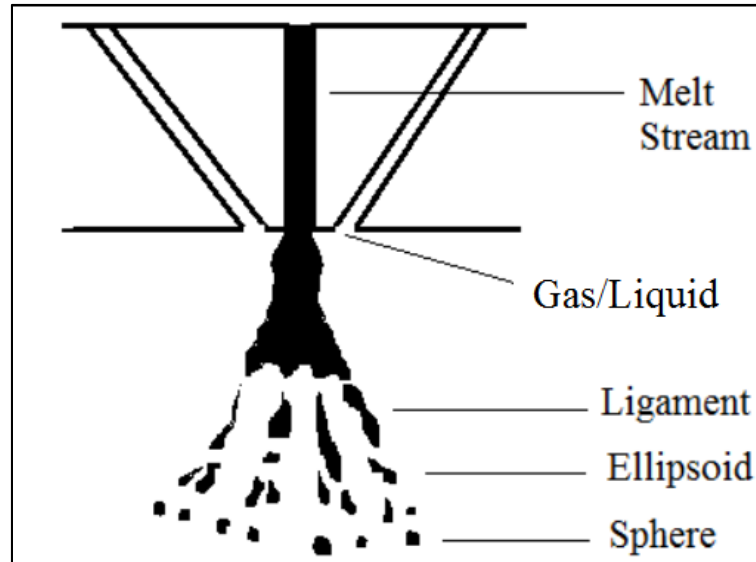
Figure 2-2: The gas atomization process [21]

Liquid and gas designs differ only in that the liquid used in a liquid atomizer collects at the bottom of the container with the powder as shown in Figure 2-3. Gas atomizers typically use air, nitrogen, helium, or argon and are used for metals that require a high melt temperature. Liquid atomizers employ water or synthetic oils and are typically used to produce powders from metals that can be melted below 1600°C. Liquid atomizers also enable rapid quenching which leads to better control of the powder microstructure. Gas and liquid atomization typically produce powders ranging in size from 1 to 10 μm in diameter, although gas atomization tends to produce smaller particles on average than liquid atomization [21].
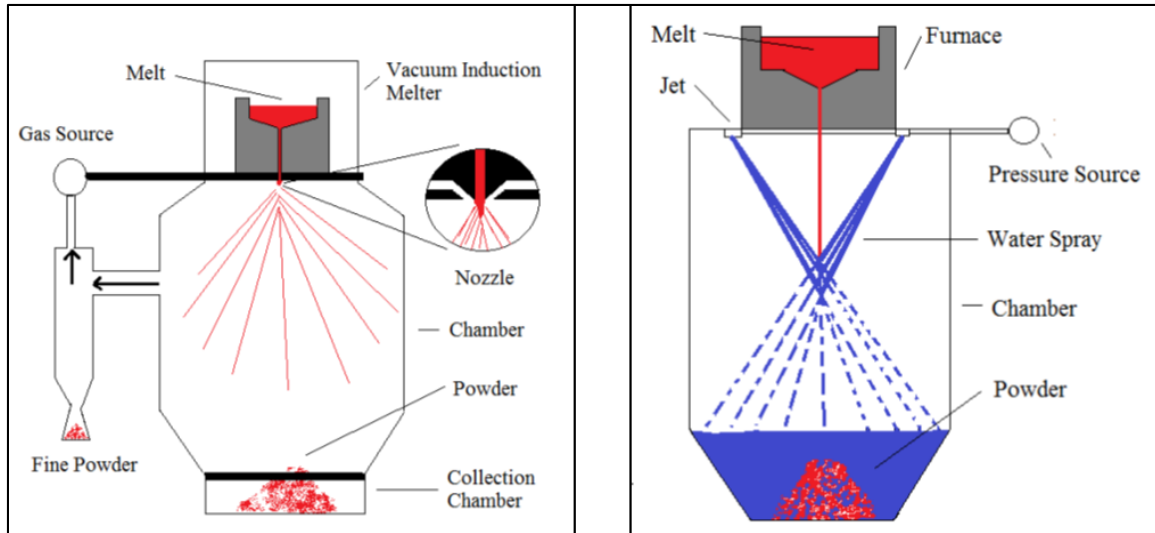
Figure 2-3: Comparison of gas (left) and liquid (right) atomizer designs [21]

The chemical reactivity of uranium and its alloying metals, particularly zirconium, removed it as a candidate for gas/liquid atomization. Uranium and zirconium oxidize quickly upon contact with water and air and their molten forms may react with some crucibles. To avoid elemental contamination from the crucible and nozzle, development of a suitable crucible/nozzle configuration would be a significant project of its own. The rotating electrode process is a contactless melting method that greatly decreases the chance of contamination and is discussed in the following section.

2.2.3.2 Rotating Electrode Process

Centrifugal atomization is especially useful for the conversion of reactive and/or refractive metal powders because it does not require the feed metal to be molten or superheated. Centrifugal atomization via the rotating electrode process produces spherical powder in a tighter size distribution than the previous gas or liquid atomization techniques as described in section 2.2.3.1 [23]. The Rotating Electrode Process is a centrifugal atomization

method that was patented by Starmet Corporation in 1972 [22]. The system consists of rotating a cylindrical metal rod at high rotational speeds (on the order of 45,000 RPM) along its longitudinal axis and melting the tip via the application of a high current electrical arc or plasma. As molten metal formed on the tip of the rotating rod, it was propelled in a radial spray as centrifugal forces overcame the surface tension forces resisting the liquid expulsion. Surface tension forces caused the expelled molten droplets to form spheres which solidified in flight before being collected by the atomization system. Figure 2-4 shows a high speed camera image capturing molten droplets being expelled away from a rotating electrode in a similar system.
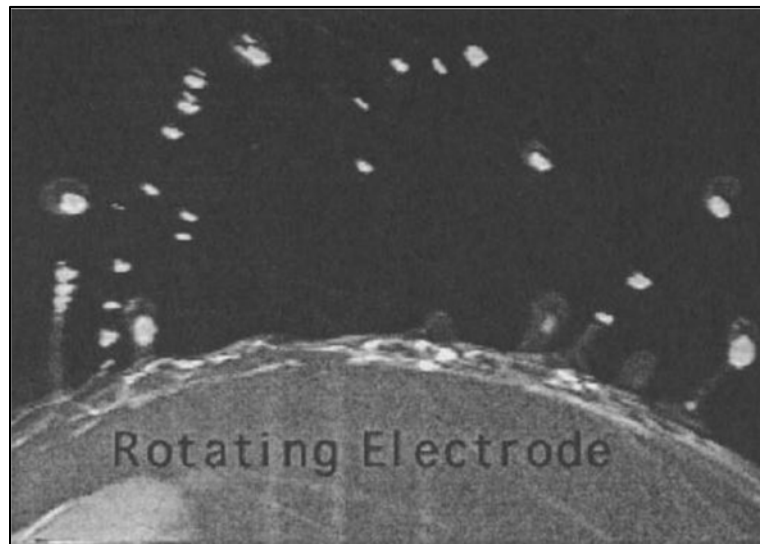
Figure 2-4: Photograph of the rotating electrode process during operation [21]

The rotating electrode process employs contactless melting which translates to very little contamination of the powder arising from contact with system hardware; atmosphere conditions may create contamination if the molten metal is chemically reactive. The powder

17

produced by the rotating electrode process is nearly perfectly spherical which allow for favorable flow properties and predictable packing densities. The rotating electrode process produces larger powder with size distributions is more tightly concentrated than other atomization processes. Powder produced using the rotating electrode process typically does not exhibit porosity, since it uses centrifugal forces to break up molten ligaments rather than aerodynamic drag [22].

Champagne and Angers [24] confirmed that there are three basic droplet formation modes that operate during centrifugal atomization, as shown in **Figure 2-5**: (1) direct drop formation, (2) ligament formation, and (3) formation disintegration.
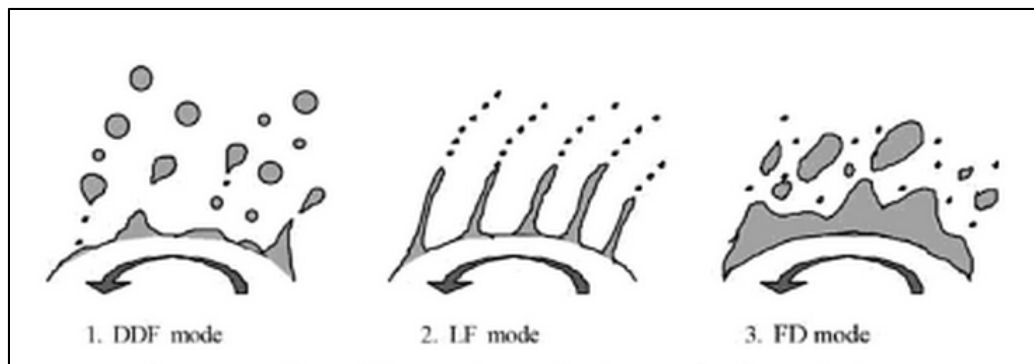
Figure 2-5: Three disintegration modes in centrifugal atomization [23].

In the direct drop formation mode, surface tension is lower than the centrifugal force and droplets form, often with irregular tails that separate from the larger droplets into smaller "satellite" spheres. Thus, this mode typically exhibits a bi-modal size distribution of particles. The ligament formation mode occurs when the rod tip melts at such a rate that significant liquid forms at the periphery of the rotating surface, creating a liquid torus that

breaks free in long ligaments instead of spheres. A schematic representation of the liquid

torus and protuberances around the rotating anode can be seen in Figure 2-6. The presence of

more liquid at the periphery allows the molten metal to form protuberances with larger peaks.

This theory of formation was developed by Taylor [25] and confirmed by Champagne and

Angers [24]. The ligament formation mode also exhibits a bi-modal size distribution, but the

weight fractions of the small and large droplets begin to approach similar values. With

continued increase of molten material at the rod's periphery, the droplet formation mode

shifts to formation disintegration, where the ligaments become unstable and larger powders

are produced [23].
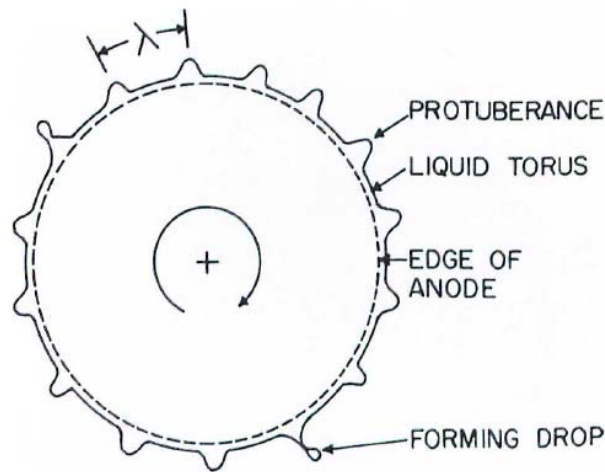
**Figure 2-6: Schematic representation of the liquid torus and protuberances around a
rotating anode [24]**

Champagne and Angers' analysis of centrifugal atomization enabled a quantitative

characterization relating the average diameter of particles produced in the direct drop

formation mode [26]. The median particle diameters in μm of the dominant mode (excluding satellite particles) d_{50}^d (on a weight basis) is defined by

$$d_{50}^d = 4.27 \; x \; 10^6 \cdot \frac{1}{\omega^{0.95}} \cdot \frac{1}{D^{0.61}} (\frac{\gamma}{\rho})^{0.42} Q^{0.12} \qquad \qquad \text{2-1}$$

where Q is the anode melting rate in m³/s, D is the diameter of the rotating electrode in meters, and ω is the angular velocity of the rotating electrode in radians/s, γ is the surface tension in N/m, and ρ is the liquid density in kg/m³. A second relation, d_{50}^s, was developed to describe the secondary mode median diameters (excluding larger particles) and is defined by

$$d_{50}^s = 1.77 \; x \; 10^6 \cdot \frac{1}{\omega^{0.80}} \cdot \frac{1}{D^{0.58}} (\frac{\gamma}{\rho})^{0.27} Q^{0.25} \qquad \qquad \text{2-2}$$

2.3   Description of Rotating Electrode Systems in Literature

Three previously published rotating electrode systems and their findings are discussed in this section: the rotating electrode process design by Starmet [27, 28], the Idaho National Laboratory (INL) design [12], and the system used by Champagne and Angers in their research [24, 26]. The Starmet and INL design schematics are depicted in Figure 2-7 and Figure 2-8 below. The system used by Champagne and Angers was similar to Starmet's design. The primary differences between the INL and Starmet designs were that INL's version had a vertical system that could reach speeds up to 40,000 RPM with a different electrode motion scheme. For the INL system, the tungsten electrode moved toward the rotating electrode during operation in contrast to the continuous feed system with a stationary tungsten electrode in the Starmet system. Starmet's design was horizontal and could only

20

reach rotational speeds of 18,000 RPM. Both systems operated in inert atmospheres. The INL

design was placed inside of a glovebox while Starmet and Champagne used pressurized

systems.
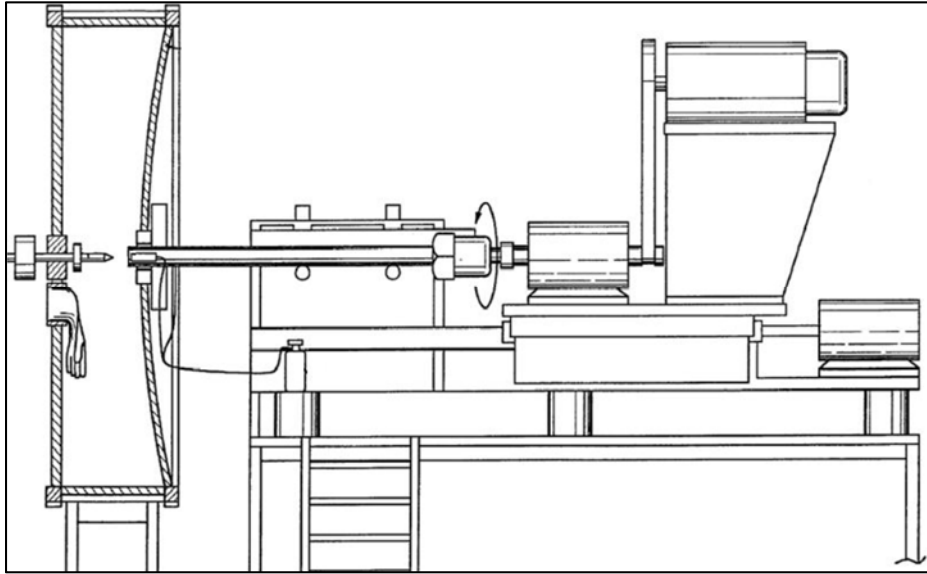
Figure 2-7: The rotating electrode process by Starmet Corporation [29]
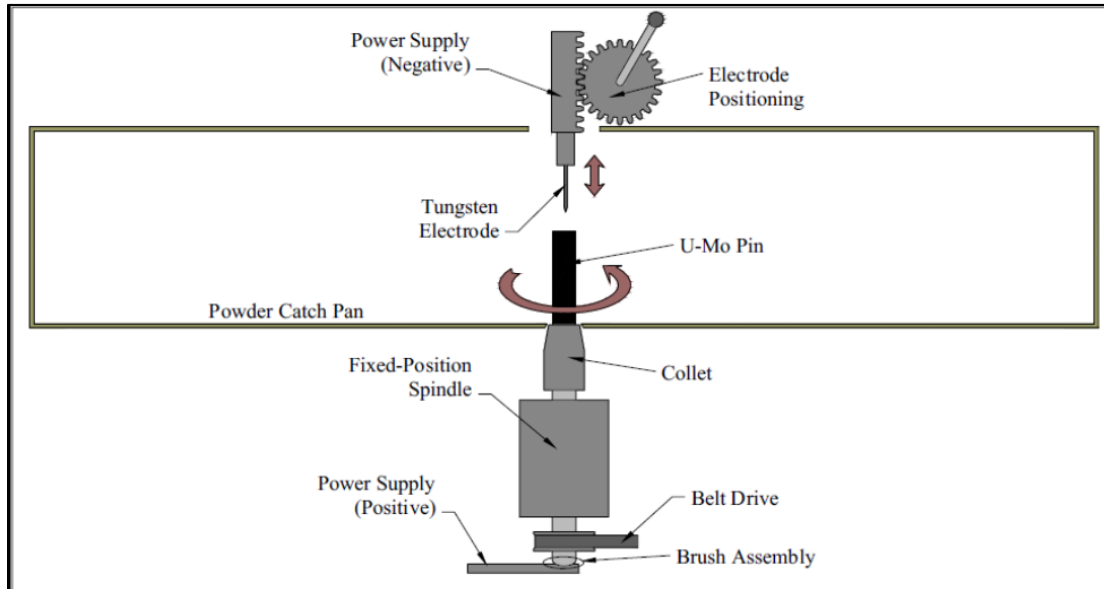
Figure 2-8: The rotating electrode process by INL [12]

2.3.1 The INL System

The INL system has been used to produce and characterize U-7wt% Mo powder using 75 A of current. This U-7Mo powder was used to help fabricate fuel as part of the Reduced Enrichment for Research and Test Reactors (RERTR) program. The rotational speed of the U-Mo anode was controlled by increasing the current supply to the drive motor by raising the voltage of the system using a variable transformer unit. A maximum velocity of 45,000 ROM was achieved at 140 V. Usable powder for this experiment was defined as particle less than 106 μm in diameter. All larger particles were collected and re-melting to undergo a second round of atomization. The U-7Mo rods that were atomized were 3/8 inches in diameter [12].

Figure 2-9 compares the size distributions of particles produced at rotational speeds of 35,000 RPM and 45,000 RPM respectively. The U-7Mo powder produced by INL's rotating electrode system was spherical, homogeneous, and exhibited the same decreasing median

22

size correlated to an increase in rotational speed as predicted by Equations 2-1 and 2-2. The rotational speeds were measured without a load (i.e. a rod) inserted and could have changed while running the system with a rod inserted [1]. It can also be seen from Figure 2-10 and Figure 2-11 that the U-7Mo microspheres produced by INL's rotating electrode system were not porous and that no segregation occurred between the uranium and molybdenum [12]. These findings led to the expectation that any U-10Zr powder produced in this present study would also show no sign of elemental segregation or porosity. However, analysis of the elemental microstructure of the powder produced was outside of the scope of the study and was not performed.
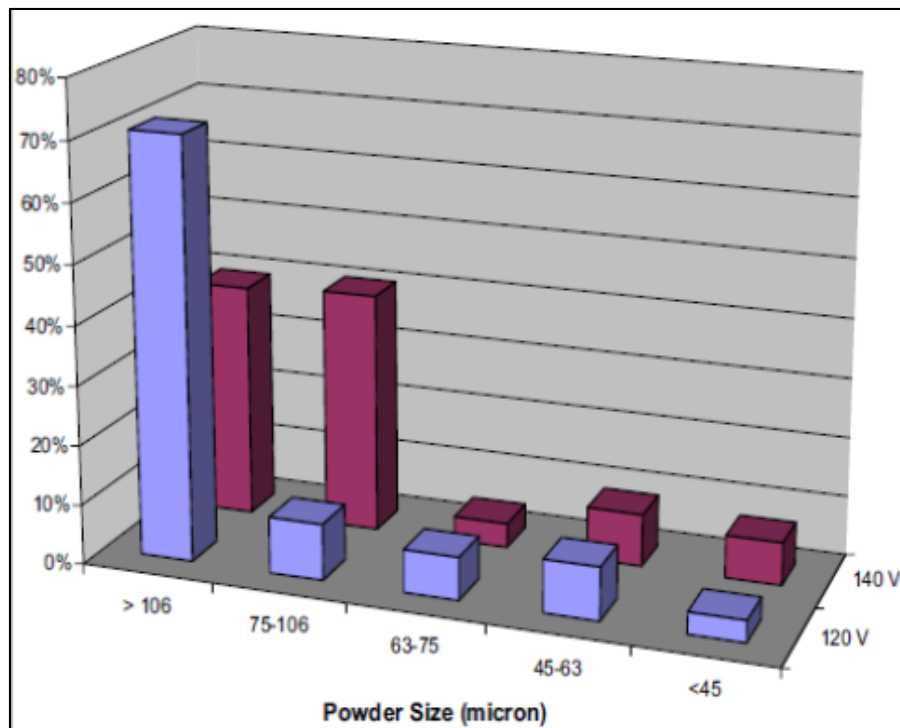
Figure 2-9: The effect of rotational speed on U-7Mo particle size [12]
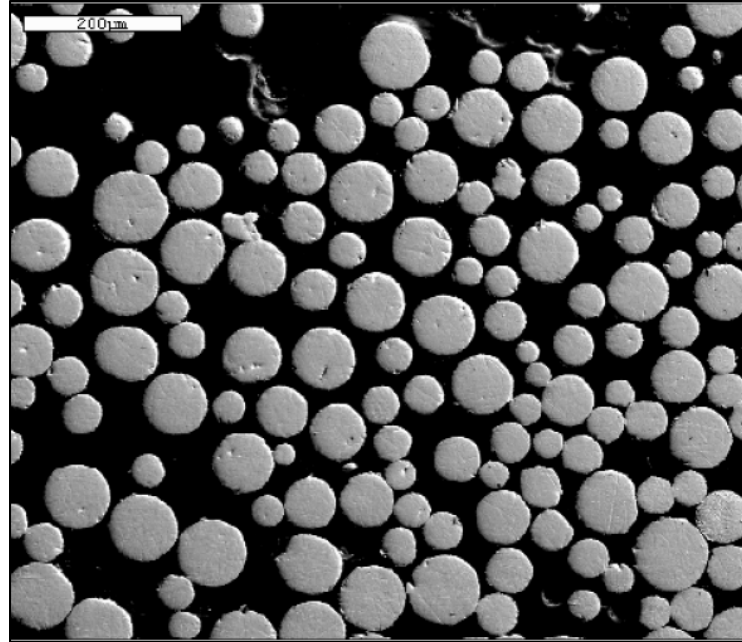
Figure 2-10: Polished U-7Mo particles produced using INL's centrifugal atomizer [12]
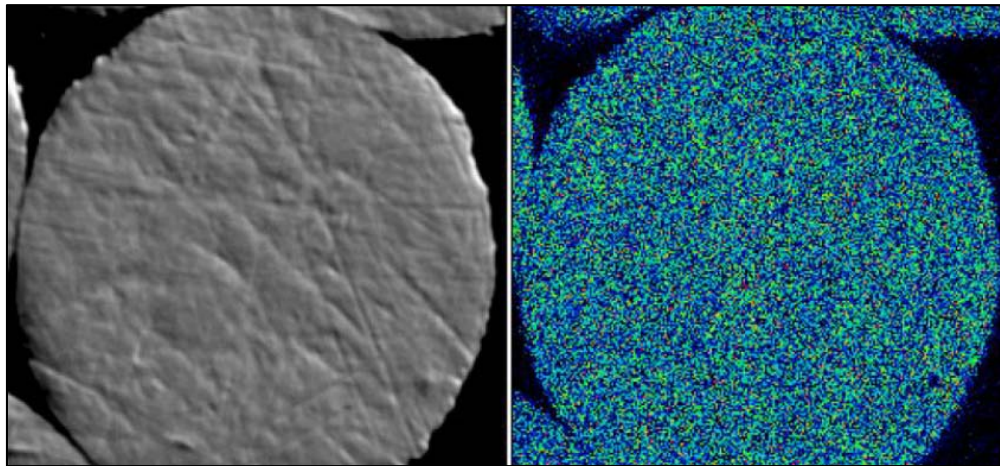
Figure 2-11: Scanning Electron Microscopy photograph compared to X-ray map of U-7Mo element distribution [12]

2.3.2   The Starmet System

Starmet's rotating electrode system was designed for industrial uses and used to produce

SAE 1018 steel and titanium alloy powder [22]. It was operated at rotational speeds of 2,500

RPM to 17,500 RPM and consumed rods with diameters between 2.5 and 3.5 inches. The atmosphere within the catch pan of the Starmet system was vacuum controlled and filled with helium during operation. Figure 2-12 displays the size distributions of atomized SAE 1018 steel and titanium alloys obtained from the Starmet system [22].
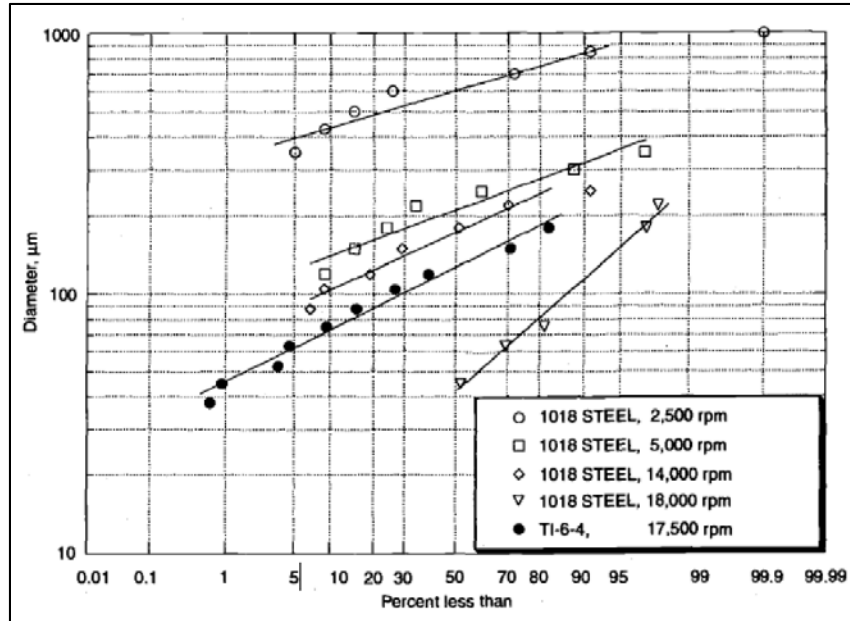
Figure 2-12: The effect of rotation speed on SAE 1018 steel and titanium alloy median particle size [22]

2.3.1   The Champagne/Angers System

The rotating electrode system used by Champagne and Angers [26] was a horizontal design and used an electric motor to control the rate at which the tungsten cathode was moved toward the rotating anode. This keeps the melting rate constant. Like the Starmet system, it was filled with helium at a positive pressure during operation. A total of 126 atomizations were performed using five different metals (Armco iron, SAE 1090 steel,

Copper (99.9%), Aluminum (99.999%), and Zinc). Angular velocity, rod diameter, and melting rates of the anode varied from 622 to 1570 rad/s, 1.27 to 3.1 cm, and 6.58E-8 to 7.5 E-7 m^3/s, respectively [26].

Champagne and Angers found that the melting rate of the anode had a significant effect on the particle size distribution but not on the distributions mean particle size. However, for high melting rates, it was observed that metals with a larger value of the surface tension to liquid density ratio ($\frac{\gamma}{\rho}$) exhibited larger mean diameter sizes. At even higher melting rates (7.5 x 10^{-7} m^3/s), a more unimodal and widely dispersed weight percent distribution was observed.

Figure 2-13 shows a typical size distribution of SAE 1090 steel powder atomized by the direct drop mechanism and characterized by Champagne and Angers. It depicts both weight percent and number percent distributions. It was noted in their findings that the shape of the weight percent distributions were not influenced much by an increase in rotational velocity, other than shifting the peaks to a smaller size. Increasing the rotational velocity did however influence the number percentage size distribution significantly as shown in Figure 2-14 (b). As the rotational velocity increased, the number of satellite particles produced approached the same number of primary particles produced.
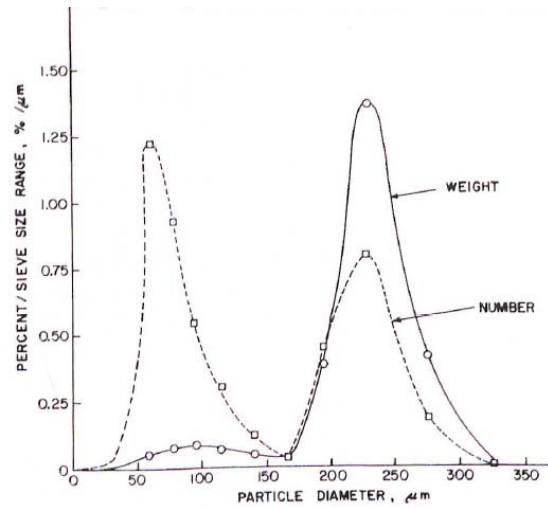
Figure 2-13: Typical particle size distribution of SAE 1090 steel powder atomized by the rotating electrode method (1230 rad/s; D=0.019 m; Q=2E-7 m^3/s) [26]
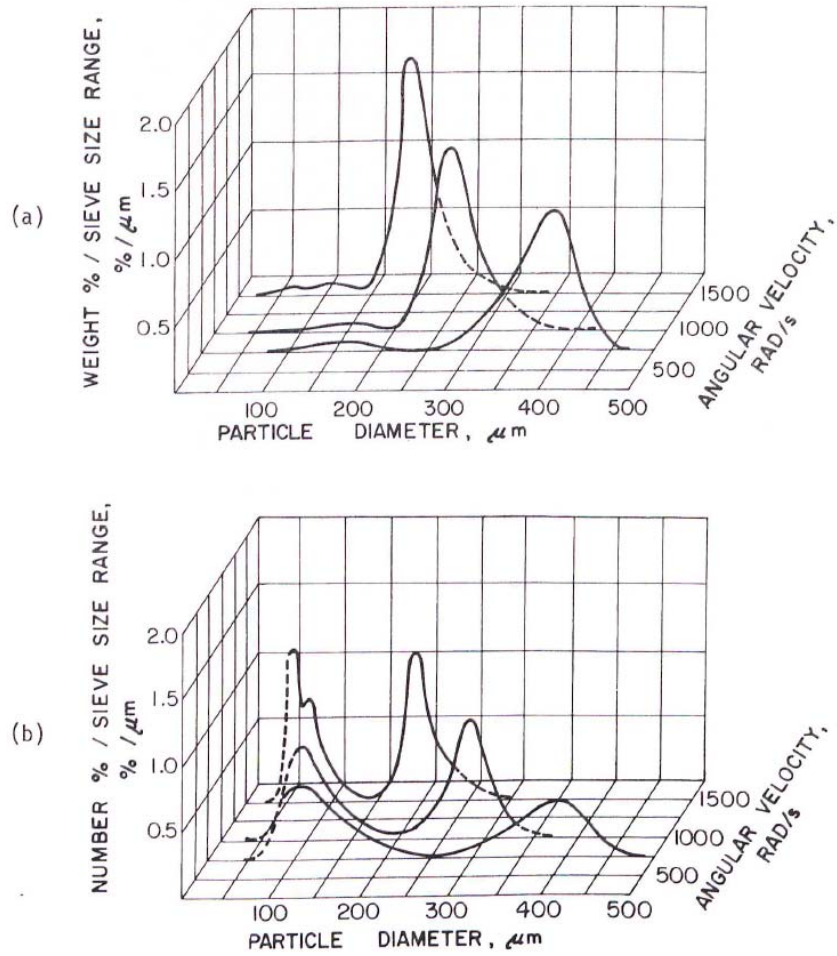
Figure 2-14: Influence of anode angular velocity on the particle size distribution of REP powders (SAE 1090 steel; D=0.019 m; Q=1.8E-7 m^3/s): (a) On a weight basis; (b) On a number basis [26]

3. EXPERIMENTS

This chapter describes rotating electrode system and supporting equipment as well as the operating procedures developed during the production and characterization of copper, depleted uranium metal (DU), and U-10Zr metal alloy powder. Section 3.1 describes the system and related equipment, Section 3.2 presents the procedures used for powder production and Section 3.3 presents the procedures created for powder characterization.

3.1 Rotating Electrode System

The rotating electrode system was previously established as a benchtop unit that was open to air by Chad Thompson [1] and is shown below in Figure 3-1. Modifications and improvements were necessary for this present study to improve the user interface for operation and the modified system was installed into an inert atmosphere glovebox.

Figure 3-1: The Rotating Electrode System as built by Thompson [1]

3.1.1   Rotating Electrode System Description

The RES is composed of: (1) an iron spindle holder which holds one Dynomax model 1860 motorized spindle and one Dynomax model 2000 non-motorized spindle, (2) a slip ring-electrical brush system to connect the two spindles and which provides a ground connection for the system, (3) a variable frequency drive (VFD) connected to the motorized spindle, (4) a water coolant system for the motorized spindle, (5) a catch pan to retain powder, (6) a helium cooling system attached to the catch pan to cool powder as it is produced, (7) a tungsten inert gas (TIG) welder tip to provide the arc that melts the tip of the rotating source rod, (8) an aluminum framework that structurally supports the spindle holder, and (9) a lathe bed that allows the catch pan to be moved back and forth in one dimension. The following sections describe these components in a cursory overview of how the RES was designed and to provide a basis by for comparison for modifications to the original design. Supplemental detail about each component can be found in Thompson [1].

3.1.1.1   Spindles & Spindle Holder

The RES has one motorized spindle and one non-motorized spindle. The purposes of the spindle are to: (1) hold the anode rod during operation, (2) hold the slip ring during operation, and (3) allow the system to rotate during operation with minimal friction losses.

The model 1860 motorized spindle is a water-cooled, three-phase, integral conduction AC motor designed to operate at 460 V with a power curve depicted in Figure 3-2. It is designed to operate at a maximum RPM of 40,000, has one 1.25 cm (0.5 in.) collet, and is controlled using a variable frequency drive. The model 2000 non-motorized spindle is comparable in size and is designed to safely rotate at the same speed as the 1860 model.

Besides being non-motorized, it varies from the 1860 model by having two, 1.25 cm (0.5 in.) collets (one on each end), connected by a solid shaft. The two spindles are connected to each other by having one collet on each spindle grip one end of a slip ring as shown in Figure 3-3. The spindles are held by set screws in a custom Dynomax spindle holder (Figure 3-4) that aligns the spindles and holds them steady during operation.
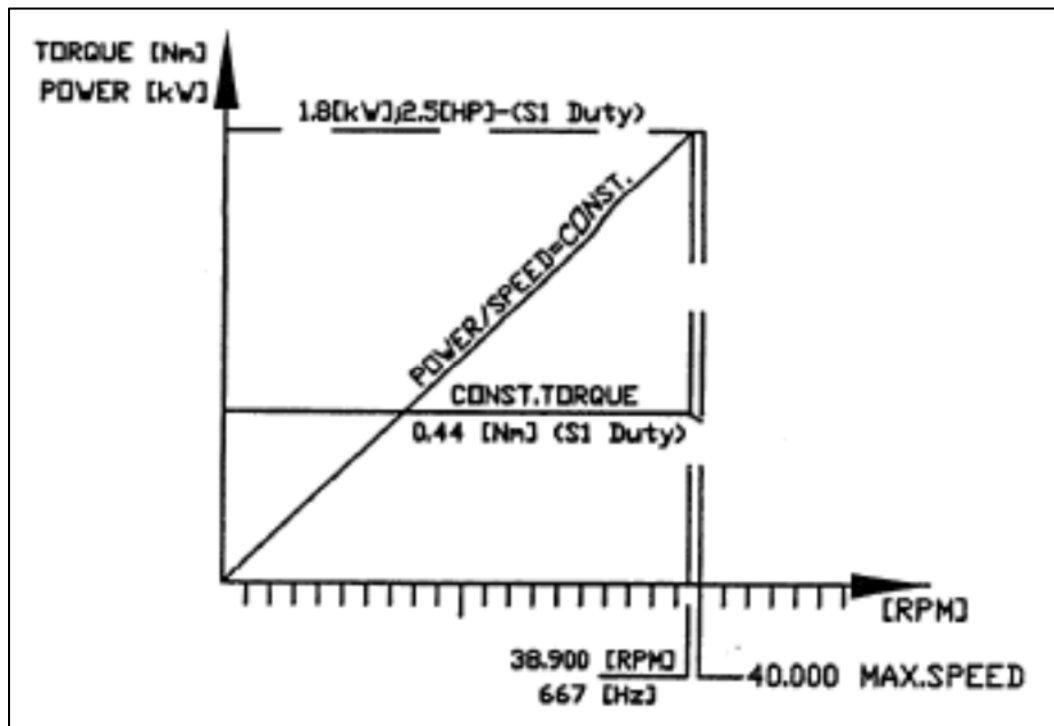
Figure 3-2: The power curve of the model 1860 motorized spindle

Figure 3-3: Photograph of the slip ring mounted between the two spindles [1]

Figure 3-4: Photograph of the Dynomax Spindle Holder with spindles installed [1]

3.1.1.2   Variable Frequency Drive

The variable frequency drive (model SF430V) is manufactured by AC Tech Lenze and provides power to and controls the rotational speed of the motorized spindle. It controls both by adjusting the frequency and voltage supplied to the motorized spindle. It is mounted within an electrical box, shown in Figure 3-5, that contains a 10A breaker for surge protection. The VFD connects to the motorized spindle via a proprietary cable. One end is fitted with a screw cap and fits directly onto the spindle. The other end requires that the wires be connected directly to the output terminal of the VFD. The wiring diagram used to connect the spindle to the VFD is depicted in Figure 3-6. The U, V, and W wires were attached to the T1, T2, and T3 output terminals respectively. The ground from the motor was attached to the input ground of the VFD power supply. The spindle thermo-resistors must never be connected to the DC bus voltage outputs of the VFD or the spindle motor will be severely damaged by the resulting short circuit.

A remote keypad was connected to the VFD and installed onto the side of the catch pan so that the operator could easily control the spindle power without having to move away from the RES. The secondary keypad is shown in Figure 3-7. Modifications were made to the keypad location when the RES was moved into the glovebox since it could not remain attached to the RES. More details about this modification can be found in section 3.1.4.

Figure 3-5: The SF430V Variable Frequency Drive mounted in an electrical enclosure box [1]
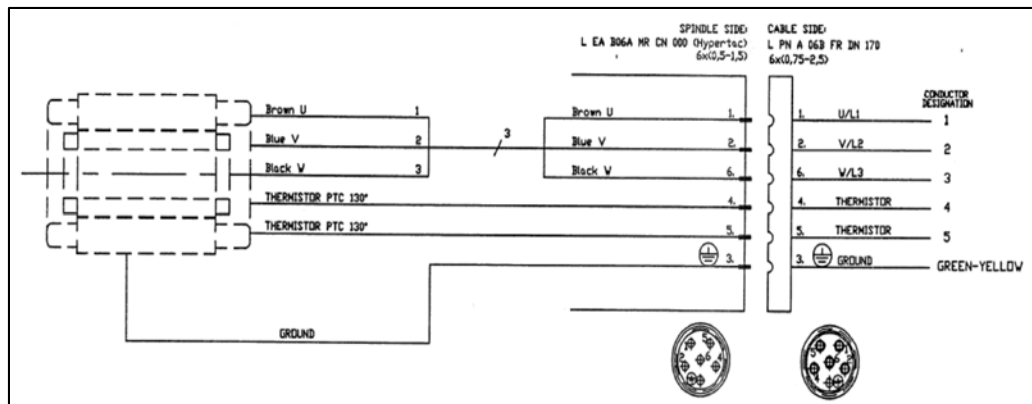
Figure 3-6: The wiring diagram to connect the spindle cable to the VFD

Figure 3-7: Variable frequency drive remote key pad [1]

3.1.1.3   TIG Welder & Torch Holder

The power supply that provides the energy to establish an arc between the rotating electrode and the welding electrode comes from the Lincoln TIG-225 welder, shown in Figure 3-8. The TIG-225 has a maximum operating current of 200 A with a duty cycle of 100% while running at 90A DC, and of 40% while running at 200A DC [30]. A welder's duty cycle is the percentage of a unit of time (typically ten minutes) that a welder can be continuously run before overheating [31].

35

Figure 3-8: The Lincoln TIG 225 welder [32]

The tungsten electrode is located within the torch head. The torch head is clamped onto a triangular aluminum holder designed and fabricated to hold the electrode level in a horizontal position, as shown in Figure 3-9. The operator controls the current that is being sent to the welding electrode via a foot "amp troll". The amp troll resembles a car pedal and operates in the same fashion. If the user requires a higher current, pressure may be applied to the amp troll. A decrease in pressure corresponds to a decrease in applied current. The TIG 225 also allows for a maximum current limit to be set before operation begins so that too much current cannot be accidently applied.

Figure 3-9: The angle of the welder electrode relative to the torch head [1]

3.1.1.4   Slip Ring & Brushes

The electrical brushes shown in Figure 3-10 are used in the RES to enable the flow of high current through the rotating electrode by providing a conduit for the ground connection. They are Mersen (Philadelphia, PA, U.S.A.) model LFC554 electro graphitic brushes which are capable of operating continuously at a speed of 90 m/s while transferring 10A/cm^2 of current [33]. These types of brushes may be made from several different materials and the

selection process behind the choosing of the model LFC544 for the TAMU RES is described in Thompson [1].

Figure 3-10: A single LFC544 electro graphitic brush fabricated by Mersen [1]

The brushes are set into five Mersen model DDO 168-37 brush holders and allowed to contact the slip ring with a force of 2.07 N/cm² (3 psi). The brush holders are mounted on a 1cm diameter copper rod which is connected to ground via a copper cable coming out of the top of the slip ring holder. Dimensions of the brush holders and a picture of all five brush holders mounted on the copper rod are depicted in Figure 3-11 and Figure 3-12, respectively.
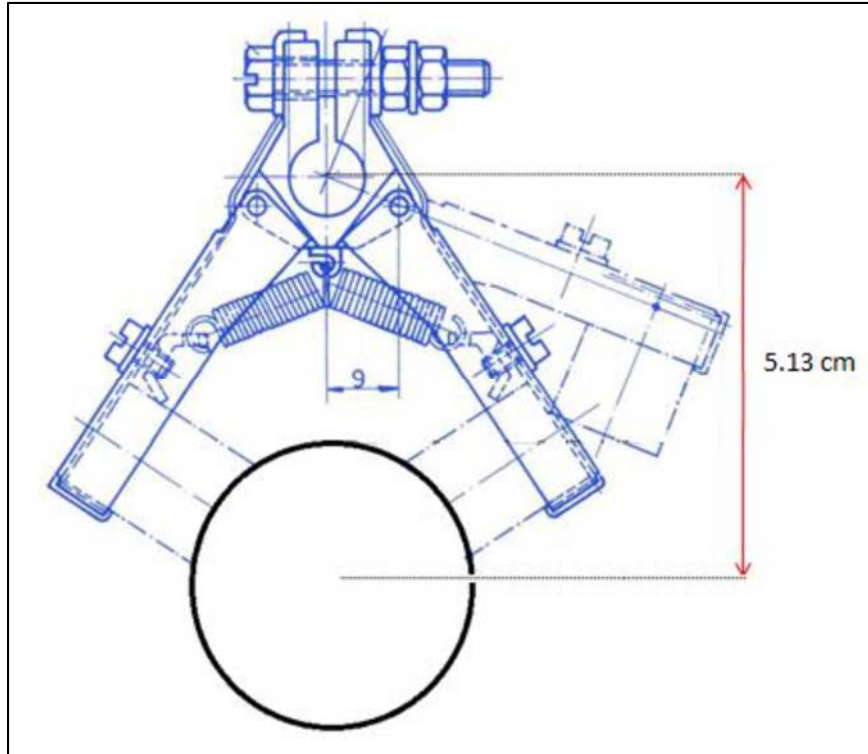
Figure 3-11: The DDO 168-37 brush holder in contact with a slip ring [1]

Figure 3-12: The five brush holders mounted to the 1cm diameter copper rod [1]

The 303 stainless steel slip ring shown in Figure 3-13 is the rotating shaft that connects the two spindles during operation and is also what the electrical brushes contact while transferring up to 200 A to the rotating source metal electrode that is being atomized. The alternating fin design of the slip ring was created with three purposes: (1) it translates motion from the motorized spindle to the non-motorized spindle by fitting into the interior spindle collets (Figure 3-3), (2) it provides for the completion of the electric circuit through contact with the electro graphitic brushes, and (3) the high surface area enables convective cooling. The amount of cooling needed depends on the heat generated by friction losses with the brushes and the voltage drop from the brushes to the slip ring. Further discussion of the slip ring cooling calculation can be found in section 3.1.2 and in Thompson [1].

Before modifications were made, the original length of the slip ring was 5.08 cm (2.00 in), the original fin diameter was 5.00 cm (1.97 in), and the original core diameter was 1.95 cm (0.75 in). Figure 3-14 shows that the fins were originally 1.00 cm thick and spaced equally from each other by gaps roughly 4.00 cm wide. 3.18 cm (1.25 in) of each end of the slip ring was machined to a diameter of 1.25 cm (0.50 in) so that the slip ring could be inserted into the collets.
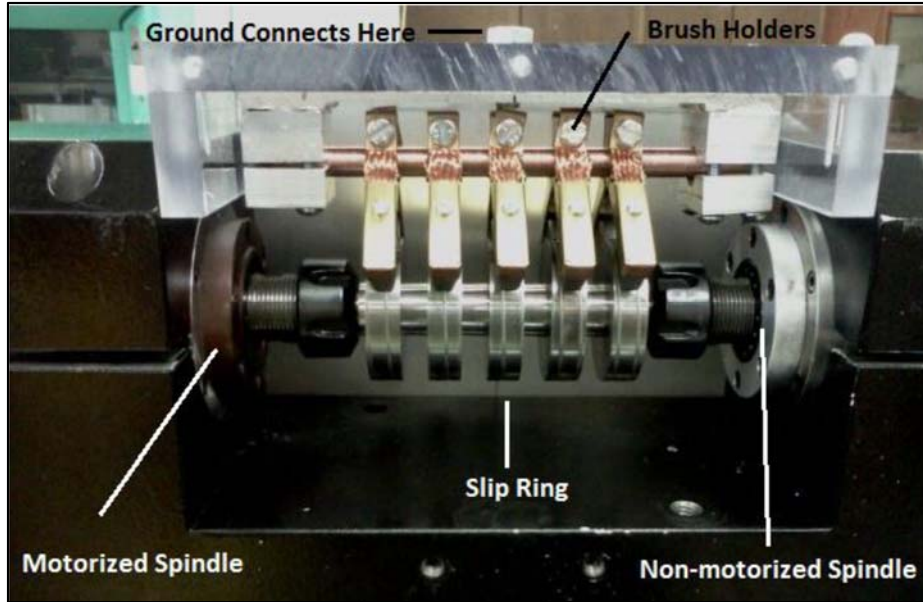
Figure 3-13: The slip ring mounted with the electro graphitic brush system [1]
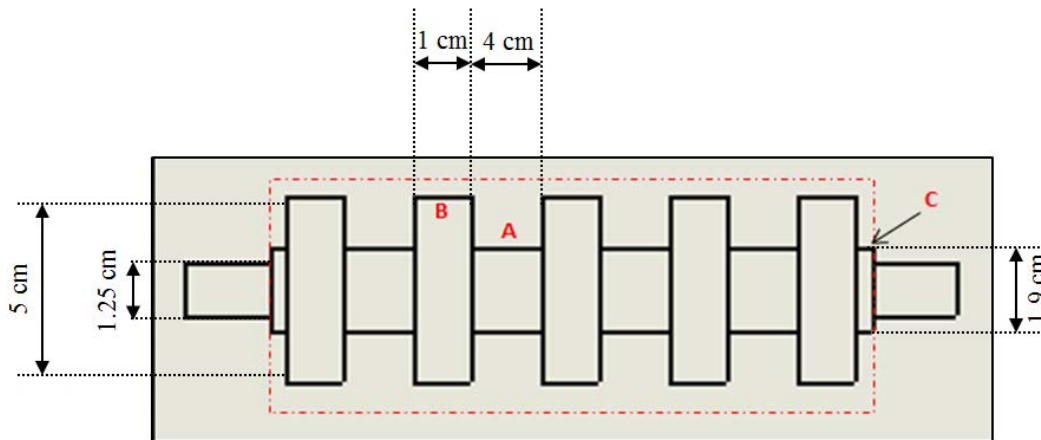
Figure 3-14: Original Slip Ring Design by Thompson

3.1.1.6   Catch Pan and Powder Collection Drawer

The catch pan shown in Figure 3-15 is a two-piece, semi-cylindrical stainless steel pan with a depth of 15.24 cm (6.00 in) and a height of 50.8 cm (20 in). It was designed to be large enough to allow the molten droplets from the rotating electrode process to solidify

before impacting the walls of the catch pan. The catch pan diameter was limited in size by the requirement to be able to fit inside a glovebox. It was determined that the quarter-inch thick walls of the catch pan is sufficient to stop an entire rod-worth of DU, the most dense metal used in this study, from penetrating the catch pan during a full speed operation at 40,000 RPM. An aluminum insert prevents powder from exiting the front of the catch pan, nearest the electrode, while allowing the rotating electrode to enter the catch pan. A Plexiglas insert prevents powder from exiting the back of the catch pan while allowing the operator to observe operation of the system while providing an access location for the TIG welding electrode. The catch drawer shown in Figure 3-16 is positioned directly below the catch pan and a hole was machined in the bottom of the catch pan to allow for powder collection. Both the catch pan and the catch drawer mounted on a movable carriage (Figure 3-17) that moves with two degrees of freedom. The operator can adjust the position of the catch pan and catch drawer both in the side to side directions as well as the front to back directions.

Figure 3-15: The catch pan without Plexiglas & aluminum inserts installed [1]
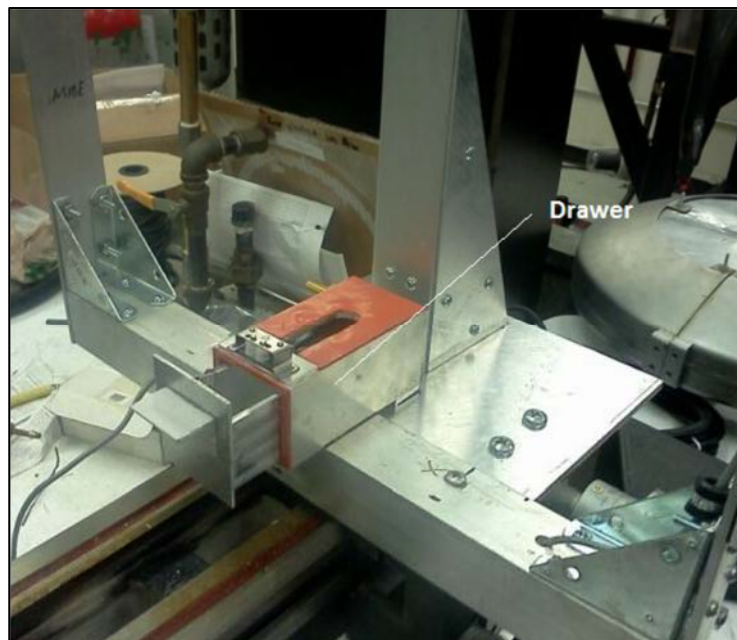
Figure 3-16: The catch drawer with the catch pan removed [1]
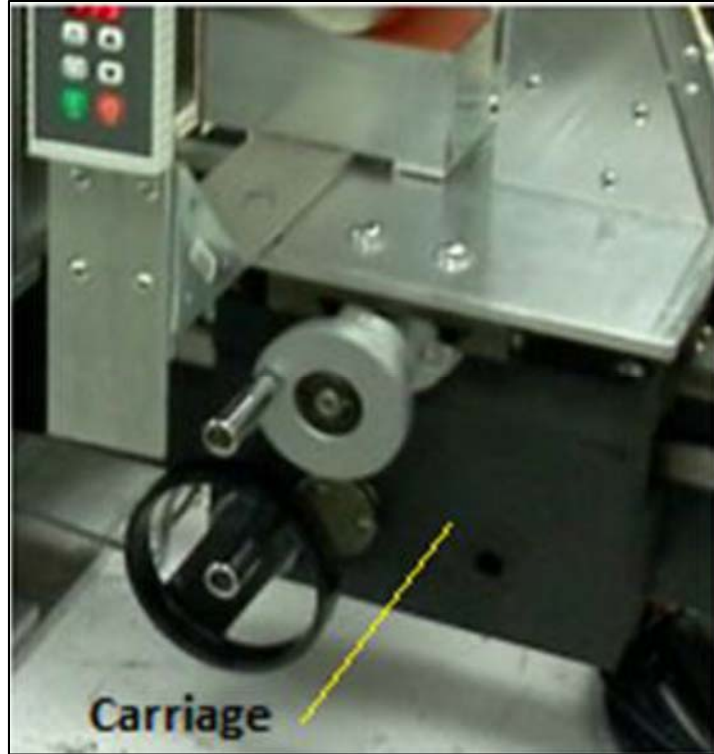
Figure 3-17: The carriage of the RES [1]

3.1.2   System Performance Estimates and Design Calculations

In order to be conservative, all calculations were done assuming the TAMU RES will be operating at the maximum design speed of 40,000 RPM, even though the nominal operating speed for this study ranged from 10,000 to 19,000 RPM.

During operation, heat is generated by friction as well as the voltage drop between the steel slip ring and the ten electro graphitic brushes. To ensure the integrity of the slip ring while operating at full speed, it was prudent to estimate the amount of heat being generated as well as the self-cooling rate of the rotating slip ring. Equation 3-1 describes the method for determining the diameter of the slip ring fins based on the maximum contact interface velocity at which the brushes are rated to operate (90 m/s). This diameter is a limiting factor

44

on how large the diameter of the slip ring can be and, along with the length limit imposed by the spindle holder, places a limit on the amount of slip ring surface area available for forced convection cooling.

$$D = \frac{v \cdot t}{\omega \cdot \pi} \qquad\qquad \text{3-1}$$

where D is the maximum allowable diameter of the slip ring, v is the maximum contact interface velocity of the brushes (90 m/s), t is the number of seconds in one minute (60 s), and ω is rotations per minute. Using Equation 3-1, Thompson calculated a diameter of 4.2971 cm (1.94 in) [1]. Thompson's reported diameter of 4.2971 centimeters is correct; however, the slip ring was manufactured with the incorrect reported diameter of 1.97 inches. With the incorrectly manufactured slip ring installed in the RES, the maximum allowable speed dictated by the brushes' rated speed was 34,350 RPM. In order to allow the RES to safely operate at 40,000 RPM, the slip ring must be replaced with a slip ring that has the correct diameter of 1.60 inches.

Thompson conservatively determined that when running the RES at 40,000 RPM and 200A, the combined heat generated by both friction and voltage drop adds up to a total of 908 W [1]. The heat removed by a rotating cylinder can be determined by

$$Q = h \cdot \pi \cdot D \cdot \Delta T \cdot l \qquad\qquad \text{3-2}$$

where Q is the heat removed in Watts, h is the coefficient of convection, D is the diameter of the cylinder, ΔT is the temperature difference between the cylinder and the ambient fluid, and l is the length of the cylinder [34]. The coefficient of convection can be determined by

$$h = \frac{Nu \cdot k}{D} \qquad\qquad 3\text{-}3$$

where Nu is the average Nusselt number, and k is the thermal conductivity of the surrounding fluid [35]. The average Nusselt number can be determined by

$$Nu = 0.11(0.5Re_w^2 + Gr_d \cdot Pr)^{0.35} \qquad\qquad 3\text{-}4$$

where Re_w is the peripheral speed Reynolds number, Gr_d is the Grashof number, and Pr is the Prandtl number [35]. The peripheral speed Reynolds number can be determined by

$$Re_w = \frac{\pi \cdot D^2 \cdot w}{v} \qquad\qquad 3\text{-}5$$

where w is the peripheral speed of the cylinder in rad/s, and v is the kinematic viscosity of the fluid [35]. The Grashof number can be determined by

$$Gr_d = \frac{g \cdot \beta \cdot \Delta T \cdot D^3}{v^2} \qquad\qquad 3\text{-}6$$

where g is the acceleration due to gravity and β is the thermal expansion coefficient [35]. The maximum temperature difference, ΔT, between the slip ring and the ambient atmosphere was set to 100 K assuming the slip ring would reach a maximum temperature of 125 ºC (this is well below the 600 ºC auto-ignition temperature of graphite in air [36]).

Once the coefficient of convection was estimated, the surface area and therefor length of the slip ring could be determined. The original design and dimensions are discussed in section 3.1.1.4 and shown in Figure 3-14. They were calculated using the properties of air and the incorrect maximum slip ring length of 1.97 inches. These calculations were modified using the appropriate maximum slip ring diameter of 1.69 inches and the properties of both air and estimate the RES behavior inside of a glovebox. Table 3-1 and Table 3-2 show the calculated results for the Grashof number, peripheral speed Reynolds number, average Nusselt number, and coefficient of convection for the slip ring using the properties of air and of argon.

Table 3-1: Properties of Air and Argon

Property	Units	Argon	Air
k	W/(m·K)	0.014808	0.0217
β	1/K	0.0041127	0.004113
P	kg/(m³)	2.0049	1.4535
C$_p$	J/(kg·K)	522.43	1005.4
v	(m²)/s	9.49E-06	1.08E-05
Pr	-	0.67158	0.72741

Table 3-2: Calculated Heat Transfer Results while Determining Slip Ring Length

Air			Argon		
Property	Fins	Gaps	Property	Fins	Gaps
Gr	2.39E+05	2.74E+06	**Gr**	3.09E+05	3.55E+06
Re	4.42E+05	2.25E+06	**Re**	5.03E+05	2.56E+06
Nu	7.73E+02	2.41E+03	**Nu**	8.46E+02	2.64E+03
h (W/m²·K)	8.80E+02	1.22E+03	**h (W/m²·K)**	6.57E+02	9.10E+02

Using Equation 3-2 and the calculated heat (W) generated by the slip ring (shown in Table 3-3), it was estimated that the widths of fin sections A and C in Figure 3-14 could be increased from 1.5 cm to 1.6 cm and that the width of fin section B could be increased from 1.00 cm to 1.27 cm. The new dimensions would increase the total length of the slip ring by 13.5 cm and provide adequate cooling to the slip ring during operation in argon by a realistic safety factor of 1.62, and a conservative safety factor of 1.05. The conservative safety factor assumes that 200 A of current is passing through the slip ring and that the slip ring is rotating at 40,000 RPM. The realistic value is based on user experience of effectively melting depleted uranium and U-10Zr using currents ranging 90 to 100 A which would decrease the amount of heat generated through a voltage drop between the slip ring and the electro graphitic brushes:

$$P = V * I \qquad\qquad 3\text{-}7$$

where P is the power generated due to voltage drop (W), V is voltage (V), and I is the current from the welder (A). The LCFC554 electro graphitic brushes have a voltage drop of 2.3 V [33] when contacting stainless steel and this value was used when calculating the amount of heat generated by the voltage drop and friction between the slip ring and the brushes. A more detailed discussion of this topic can be found in Thompson [1].

Table 3-3: Safety factors of new slip ring dimensions operating at 40,000 RPM in argon

Q cooling (W)	Q calculated (W)	Safety Factor	
1059.852	1008	1.0514	(very conservative)
	907.3	1.1681	(conservative)
	654.3	1.6198	(realistic)

3.1.3   Glovebox

The TAMU RES was relocated from an open air lab setting into an argon atmosphere glovebox, depicted in Figure 3-18, custom-made by M. Braun (Garching, Germany), an inert gas technology company, to prevent and limit oxidation of the uranium and U-10Zr powder before, during, and after production. The engineering design sheets for the glovebox can be seen in Appendix A.

Figure 3-18: The M. Braun Argon Atmosphere Glovebox

The RES spindle holder, spindles, spindle base, catch pan carriage, and catch pan track were installed into the third compartment, farthest away from the two antechambers, before the glovebox was sealed for operation. The water coolant system, as well as the power feedthroughs for the motorized spindle and TIG welder, was completed prior to glovebox assembly. Coolant water for the motorized spindle is fed through two of the eight 3/8 inch bulkhead feedthroughs in Figure 3-19. There are six 1.5 inch female national pipe thread (FNPT) full coupling ports located at the back of the glovebox, just above the bulkhead feedthroughs. Power and gas for the TIG welder are fed through one of these ports, while the ground wire for the system is fed through another. The power supply to the motorized spindle uses one of these ports as well. All three of these feedthrough systems required the

installation of Conax Technologies (Buffalo, New York, USA) gland seals which are discussed in the modifications section (3.1.4).
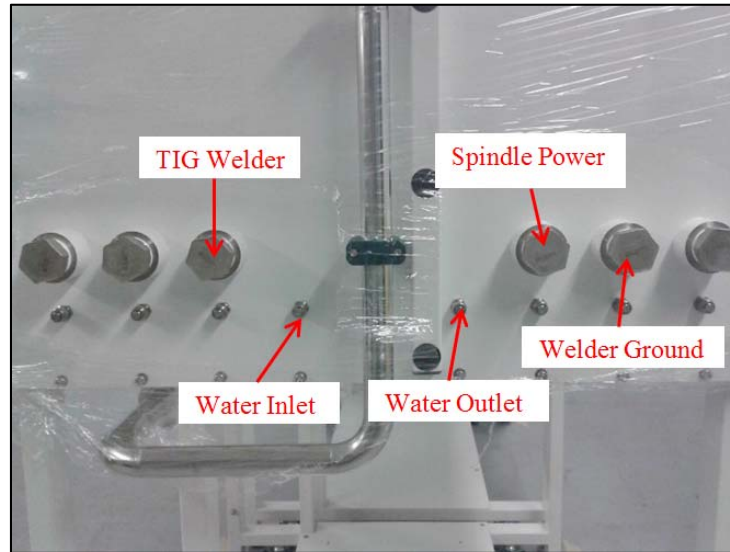
Figure 3-19: The eight bulkhead and six FNPT full coupling ports located in the rear wall of the M. Braun Glovebox

The M. Braun glovebox has one Edwards (Crawley, West Sussex, United Kingdom) model RV12 vacuum pump connected to the main glovebox chamber and its two antechambers. One antechamber is 39 cm (15.35 inch) in diameter and 60 cm (23.62 inch) long, and is used to pass large items into and out of the glovebox. The second antechamber is a 15 cm (5.9 inch) diameter, 40 cm (15.75 inch) long chamber used for passing smaller items into and out of the glovebox.

The glovebox has four glove ports per chamber, two to a side, totaling twelve glove ports in all. Each of the three chambers is also equipped with a power cord feedthrough for operating electrical devices within the glovebox.

3.1.4 RES Installation & Design Modifications
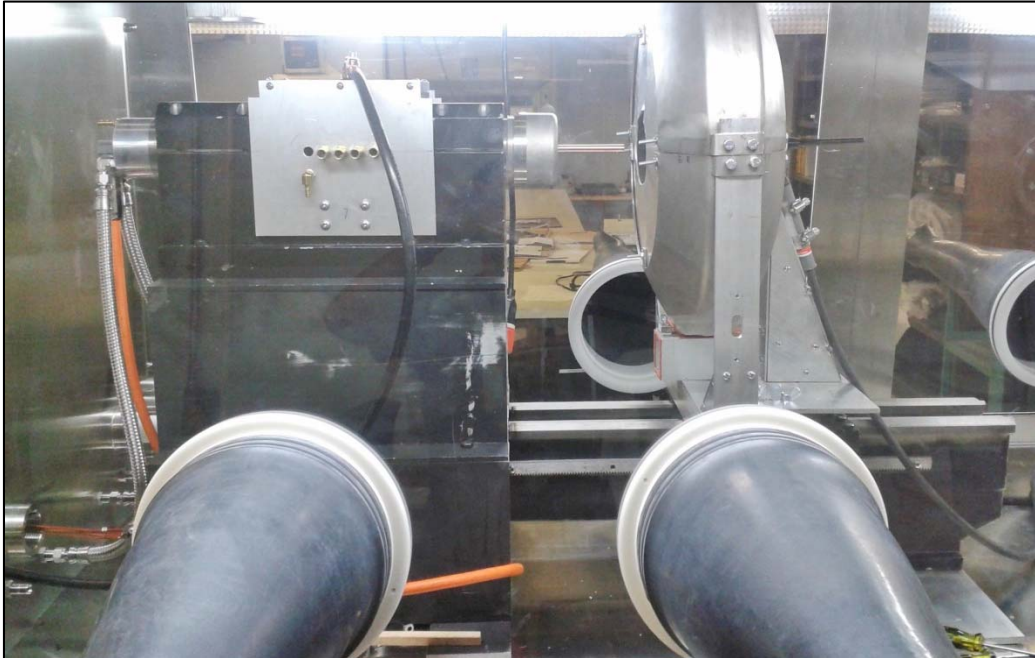
Figure 3-20: The rotating electrode system after glovebox installation and modifications

Modifications were made to the RES design to enable the installation inside of the glovebox and operational requirements. This section describes those design changes, ease-of-use upgrades, and the process of installing the RES into the M. Braun glovebox.

3.1.4.1 Large Components & Water Coolant System

Parts of the RES that were too big to fit through the glovebox's large antechamber were installed prior to the assembly and startup of the glovebox system, as can be seen in Figure 3-21. Any installation that required the use of a bulkhead feedthrough or coupling was also completed before the final glovebox assembly. Installation of the Conax gland seals, used to pass power through the bulkhead wall to the motorized spindle and TIG welder, required the use of and modification of three of the FNPT couplings. Installation of the water coolant

lines from the motorized spindle to the bulkhead wall required access to the interior-located bulkhead feedthroughs.

Figure 3-21: Pieces of the larger rotating electrode system components inserted into the glovebox before closure.

Leak-free water coolant was provided to the motorized spindle via two stainless steel braided Swagelok (Solon, OH, USA) hoses, seen in Figure 3-22. These hoses were tested to be leak-free before closure of the glovebox, by connecting them to a Thermo Scientific NESLAB ThermoFlex 5000 recirculating chiller and circulating water through the motorized spindle. De-ionized water was used during initial operations but distilled, purified water was used later to limit the slight pitting effect in both the chiller and the motorized spindle that de-ionized water has on metal surfaces [37]. A Pentair (Milwaukee, WI, USA) ECP5-10 pleated cellulose/polyester filter was installed in the line to further improve the purity of the

chiller water. Its placement in the line was after the water leaves the chiller, but before it reached the glovebox inlet. The filter (Figure 3-23) is rated to filter particles as small as 5 μm, operates at a maximum flow rate of 10 gpm, a pressure drop of less than one psi, and at temperatures between 4.4 and 51.7 ℃.

Figure 3-22: The inlet and outlet water lines connecting to the motorized spindle through the bulkhead

Figure 3-23: Water filter for the motorized spindle cooling water

3.1.4.2   Variable Frequency Drive & Conax Fittings

The variable frequency drive (3.1.1.2) and its electrical box were hung on the side of the glovebox as shown in Figure 3-24 using a hanging support. The hanging support was fashioned out of two long, thin aluminum pieces attached to the back of the electrical box with screws. The ends of the aluminum pieces were bent into hooks to grab onto the existing lip on top of the glovebox.

Figure 3-24: Hanging support for the variable frequency drive

Power supplying conduits for the motorized spindle and TIG welder were fed through three of the six 1 ½ inch FNPT full couplings located on the back wall of the glovebox, underneath the bulkhead feedthroughs. The couplings and feedthroughs from both inside and outside of the glovebox are visible in Figure 3-25.

Figure 3-25: Inside (left) and outside (right) views of the two types of feedthroughs into the glovebox

Conax Technologies specializes in sealing gland assemblies for temperature sensing and pressure/vacuum sealing applications [38]. To this end, one EGT-750 gland seal was used to transfer current and gas to the TIG welder torch, and one PL-12-4A gland seal was used to transfer power to the motorized spindle. An existing EG-500 gland seal with a cracked ceramic sleeve and old sealant was found in the laboratory and, after replacing the sleeve and the Viton rubber sealant, was used to transfer ground current from the RES system back to the TIG welder. Example cut-a-ways of each seal are shown in Figure 3-26, Figure 3-27, and Figure 3-28 below. More detailed information about the dimensions of the seals can be found in Appendix A.
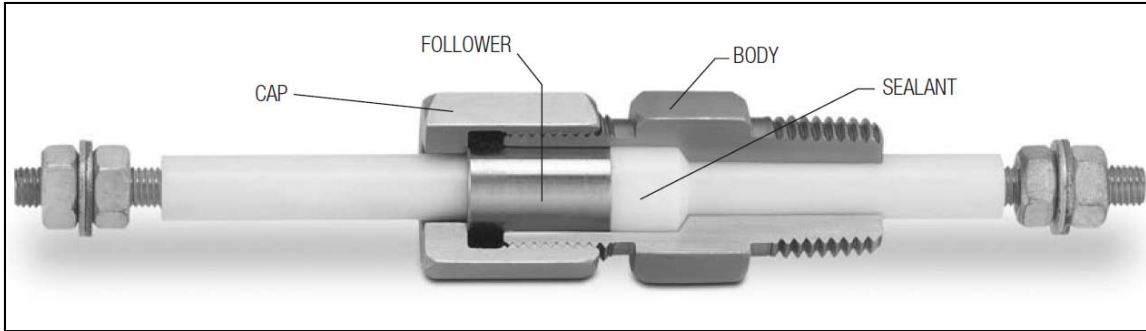
Figure 3-26: Conax, EGT series single electrode gland seal [39]
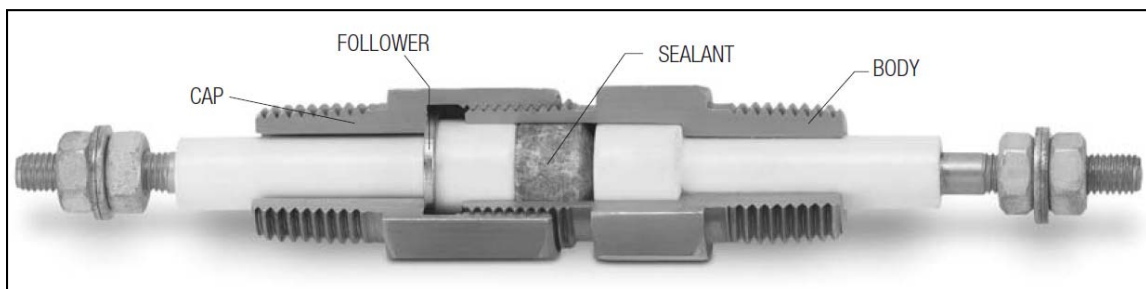
Figure 3-27: Conax, EG series single electrode gland seal [40]
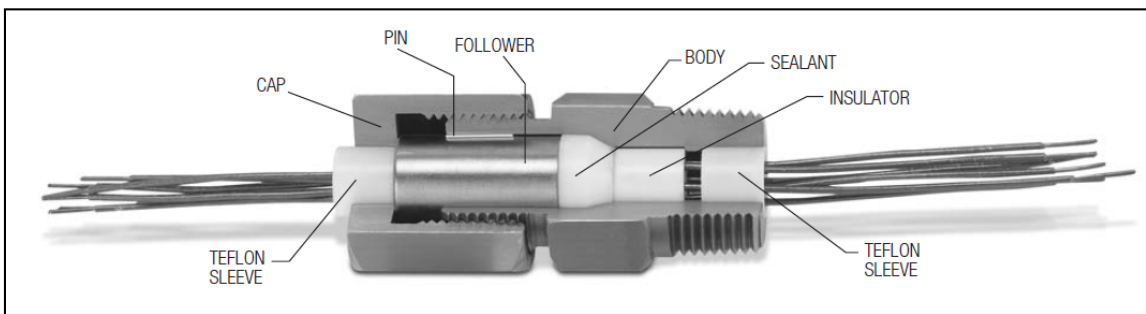
Figure 3-28: Conax insulated lead wire gland seal [41]

The bodies of the EGT and EG seals are 1 inch and 0.75 inch NPT respectively. The design required an intermediary bushing to fit into the 1.5 inch FNPT glovebox couplings. A solution was implemented whereupon two of the original 1.5 inch steel plugs shown in

Figure 3-25 were machined to accept 0.75 inch NPT fittings and one plug was machined to accept 1 inch fittings, creating bushings from the plugs.

In addition to current, the EGT seal also enabled the flow of argon gas from the TIG welder through the glovebox wall and into the TIG torch. It can be seen from Figure 3-29 that one copper adapter was machined for each end of the EGT-750 electrode. These copper adapters were designed to connect the EGT-750's threaded electrode to the TIG welder's Ultra-Flex tubing as well as pass current and argon between the two. The engineering sketch for the adapters is in Appendix B. The original Ultra-Flex tubing that came with the TIG welder connects the welder to the EGT-750 electrode. An extra length of Ultra-Flex tubing was purchased from Lincoln Electric to connect the EGT-750 electrode to the TIG torch inside the glovebox (Figure 3-30). The EGT's original copper electrode was solid, so a 9/64 inch through hole was drilled along its center line to allow argon gas to pass through.
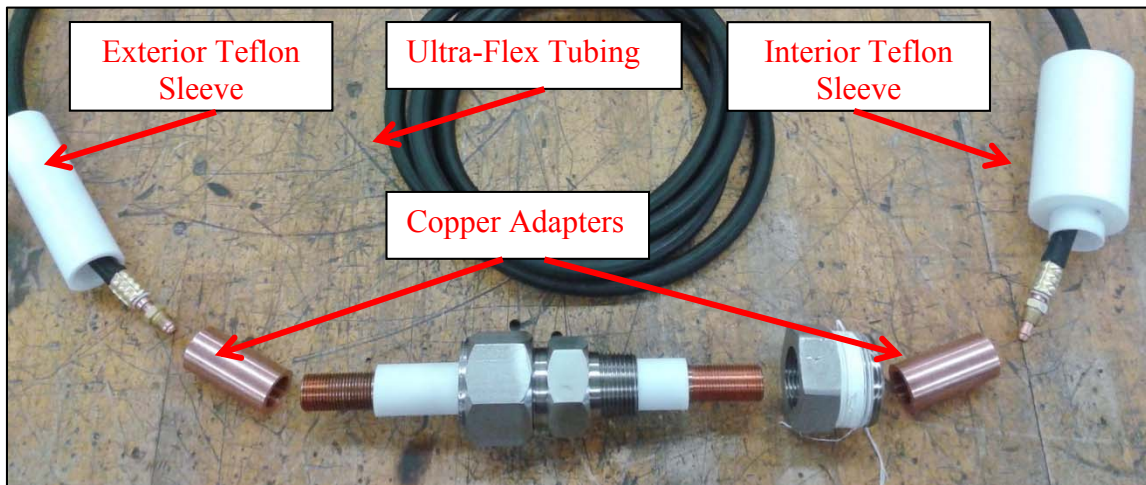
Figure 3-29: EGT-750 with copper bushings and Teflon sleeves

Figure 3-30: TIG welder torch connected to EGT-750 gland seal via Ultra-Flex tubing

Both of the copper electrodes that came with the EG and EGT seals were bare and risked arcing to the glovebox wall if installed without insulation. In addition, both electrodes were too short to traverse the length of the FNPT couplings and emerge inside in the glovebox. Therefore, Teflon sleeves were designed for both the EG-500 and EGT-750 seals that would cover any exposed copper within the FNPT couplings and prevent arcing. Two Teflon sleeves were machined for the EGT seal. Both sleeves simply slide over the existing sleeve that came as part of the gland seal and extends far enough away from the seal to cover the connection between the copper adapter and the Ultra-Flex tubing. The engineering sketch for both of these designs is shown in Figure 3-31 and Figure 3-32. An interior sleeve was all that was needed for the EG seal to cover the connection between the ground wire coming from the RES and the EG-500 electrode. A copper adapter with a set screw was machined to make this connection. The sleeve can be seen in Figure 3-33 and the copper adapter can be seen in Figure 3-34. The engineering sketch for the adapter is in Appendix B.
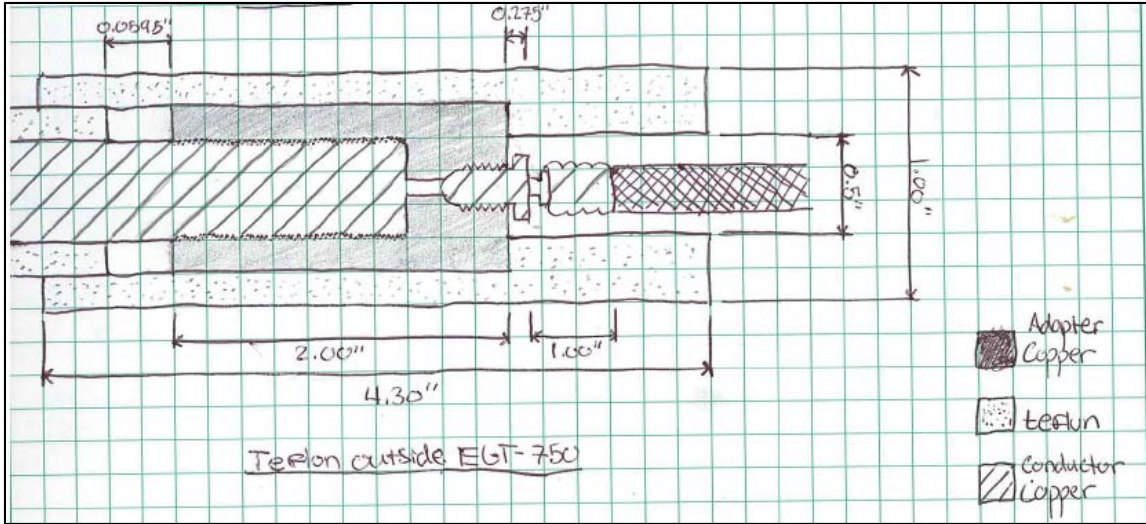
Figure 3-31: Exterior Teflon sleeve for the EGT-750
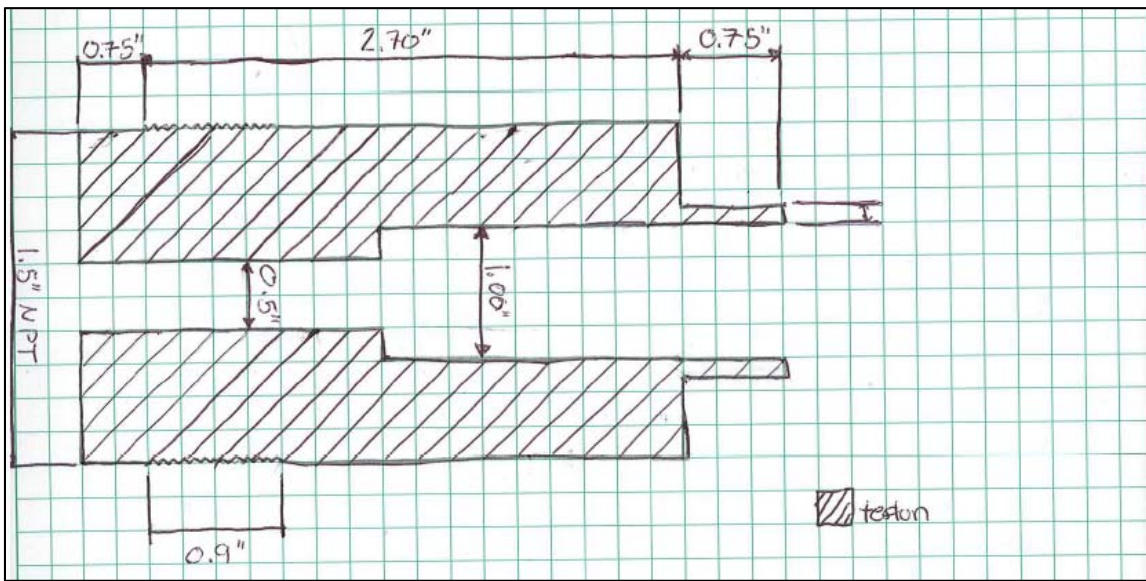
Figure 3-32: Interior Teflon sleeve for the EGT-750
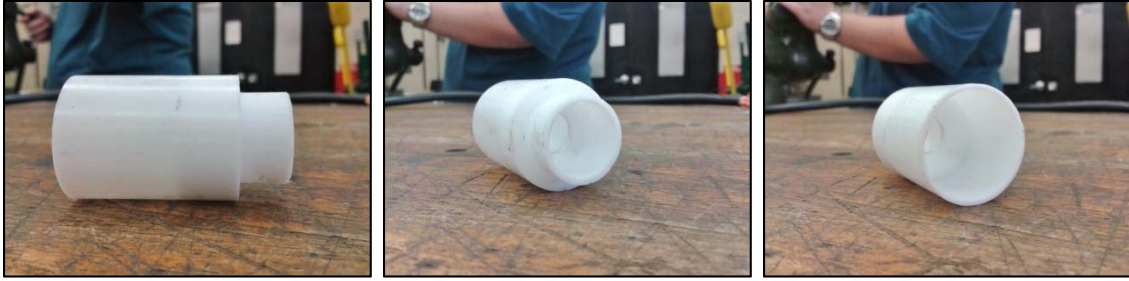
Figure 3-33: EG-500 Teflon sleeve

Figure 3-34: EG-500 copper adapter with set screw

The wire conductors that came as part of the PL-12-4A gland seal arrived insulated and so no extra insulation was needed. The PL-12-4A seal provides a connection between the VFD and the motorized spindle cable. Only four wires within the six-wire spindle cable connect to the VFD. Each of the four wires were wound together with a corresponding PL-12-4A wire and connected with a wire connector or "cap". Figure 3-35 shows how an electrical box was installed onto the side of the RES and encloses the connections between the spindle cable and the PL-12-4A wires. These wires were connected to the VFD by comparing to pictures of the VFD/spindle cable connection before it was taken apart for moving. Figure 3-36 depicts an interior view of all of the finished glovebox feedthroughs.
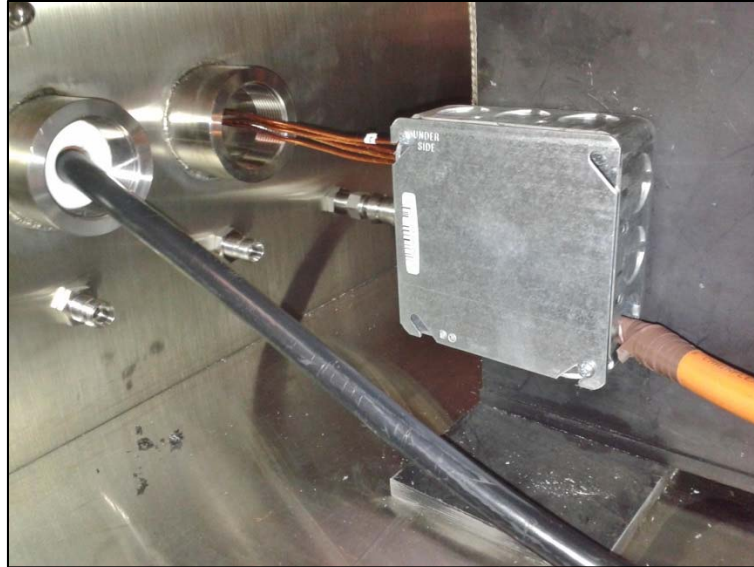
Figure 3-35: Electrical box that houses the connections between the motorized spindle cable and the PL-12-4A gland seal

Figure 3-36: Interior view of all five glovebox feedthroughs

3.1.4.1   Catch Pan & Torch Holder

Before installation into the glovebox, the catch pan was modified to improve its usability: (1) the screws that secure the catch pan frame to the carriage were replaced with wing-nuts that did not require the use of a wrench to tighten and un-tighten, (2) the holes in the frame that hold the catch pan to the frame were re-drilled and re-tapped to better align with the catch pan holes, and (3) the holes holding the Plexiglas viewing insert to the catch pan were re-drilled and tapped to accept screws and no longer required a nut and washer. A pair of 2 inch by 5 inch stainless steel strips were cut and bent to fit the inside walls of the catch pan. These were welded onto the top half of the catch pan and extend down across the crack formed where the two catch pan halves meet. The strips eliminated the need to cover the cracks with tape to prevent powder from escaping the catch pan, as was done during benchtop operation.

The torch holder depicted in Figure 3-37 was constructed of four aluminum pieces and held together by screws with washers and nuts. Over time, operating the RES would shake some of the nuts loose and the torch holder would wobble, which affected the position of the welding electrode on the face of the rod being melted. Before installation into the glovebox, the torch holder was tack-welded at several points to eliminate the need for screws.

Figure 3-37: Torch holder tack-welded together

3.1.4.2   Argon Fan & Helium Cooling System

Although it was determined in section 3.1.2 that the slip ring was capable of cooling itself during operation, a fan was installed as an extra level of safety to further ensure adequate cooling of the slip ring and electro graphitic brushes. A hole about 7 inches in diameter was cut out of the center of one of the protective aluminum plates installed on the spindle holder on either side of the slip ring, and a fan was mounted over the hole. A secondary protective aluminum plate was installed directly behind the fan, allowing enough room for argon flow, to make up for the weakness introduced by cutting the hole in the first plate. The fan blows argon over the slip ring constantly at a rate of ~100 cubic feet per minute. Figure 3-38 shows the fan system during production and after installation.

A helium catch pan cooling system was installed in order to reduce the amount of conglomeration and "flaking" depicted in Figure 3-39. Strips of slightly melted material would form along the catch pan walls as a result of particles contacting the catch pan wall before being fully solidified. The helium is delivered to the catch pan at 15 cfh through the nascent feed-through present in the top of the catch pan, eliminating the need for another gland seal installation. The flow of helium is user-controlled by turning a valve located just above system workstation inside of the glovebox.
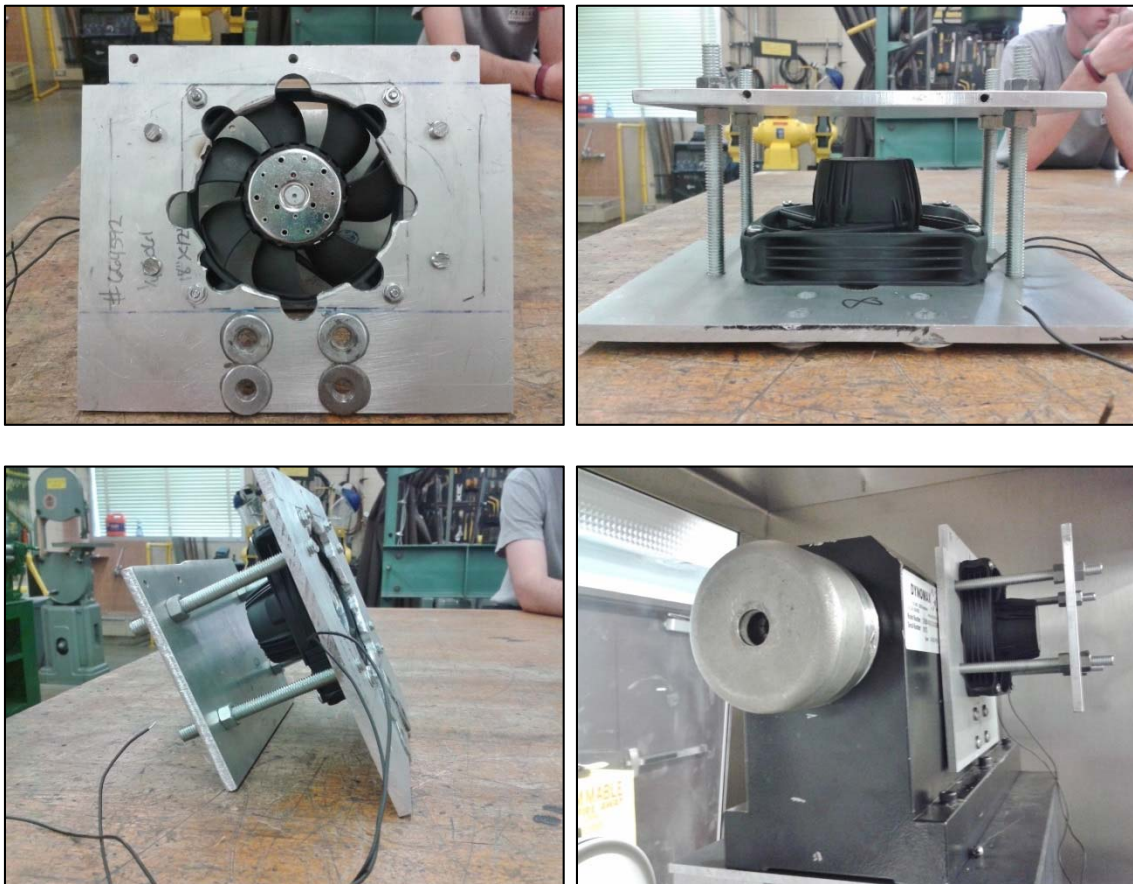
Figure 3-38: Slip ring cooling fan

Figure 3-39: Conglomeration of copper microspheres

3.2   System Setup and Operating Procedures

This section describes the steps that an operator of the RES must perform in order to safely and efficiently conduct a powder generating experiment. Sections 3.2.2 through 3.2.6 are presented as formal, step by step procedures with numbered steps replacing paragraphs.

3.2.1   Alloy Pin Preparation

The metal rod undergoing atomization should be between 3 and 5 inches in length and cylindrical. The rod must be as straight as possible to avoid vibrational issues. It was observed that the straightness of the rotating electrode is the primary limiting factor that determines the maximum rotational speed for safe operation. Before every melt, the rod's weight and length were measured. The rod was inserted at least 1 inch into the collet and the collet tightened. To achieve a sufficiently tight collet, it was sometimes necessary to hold the collet in place with a wrench while turning the black face of the collet with a pipe wrench. The heat shield was guided over the rod and the collet assembly, and tightened. For future

operators, if the metal being atomized has a low yield strength (such as copper), it is advisable to insert the rod as much as 2.5 inches into the collet to help avoid the torque strain that a longer rod will place on itself during operation. Doing this will minimize the risk that the rod will break or bend during operation.

An appropriately sized tungsten electrode was cleaned to remove any oxidation and sharpened to a point. A 2% thoriated tungsten electrode 1/8 inches in diameter was used during the present experiments to melt rods 3/8 inches and 13/32 inches in diameter. A larger electrode should be used for melting a rod greater than 13/32 inches in diameter to avoid a 'drilling' effect (Figure 3-40); where the core of the rod melts while the periphery of the rod remains solid.

Figure 3-40: "drilling" effect

A rubber stopper was inserted into the hole at the bottom of the catch pan to prevent powder from escaping during operation

3.2.2   Welder Set-Up

1. Place the welding electrode in the torch, allowing about 0.5 inch of the tip to extend past the pink ceramic nozzle.

2. Place the torch into the torch holder, allowing the electrode to penetrate into the catch pan through the center of the Plexiglas insert.

3. Using the carriage wheels, advance the torch towards the metal rod and center the electrode on the face of the rod. Arrange the welder and foot troll pedal in a comfortable position for welding.

4. Connect the torch plug to the welder.

5. Open the cover gas tank valve to allow argon to flow to the welder. Argon flow should be set to 20-25 cubic feet per hour, but the gauge will not show an accurate reading until the welder is turned on.

6. Ensure that the polarity of the welder is set to DC negative. Setting the polarity to DC positive or AC will melt the tungsten electrode faster than the metal rod.

7. Do not plug in welder to power source yet, and leave the front panel switch in the OFF position to prevent an accidental arc.

3.2.3   Water Flow & Slip Ring Fan

1. Ensure that the valve above the water filter is allowing flow and turn on the chilled water line.

2. Ensure that flow is established.

3. Plug in spindle cooling fan if unplugged.

3.2.4   Variable Frequency Drive

1. Remove the protective front panel of the VFD electronics box and turn on the VFD by flipping the breaker into the "up" position. It is designed to take two tries before remaining in the up position of its own accord.

2. Replace the protective front panel.

3. Input the mode (program design) that will be used on the experiment. Identify "automatic shut off if overloaded" and "emergency breaking power if needed" modes or program them if none exist.

4. During normal operation, ensure the mode ramps down to minimum RPM for a few minutes to ensure hot brushes do not weld to the hot slip ring. The mode will be initiated from the remote keypad. Do not turn the mode on at the panel.

5. Normal operation will not require any programming, only the power on of the VFD.

6. While wearing the appropriate personal protection equipment (PPE), set the VFD to spin the motorized spindle at around 5800 RPM by using the remote keypad attached to the catch pan. To do this: while the spindles are stationary, use the arrows on the keypad to cycle up or down until the number 100 is displayed. Rotations per minute can be calculated by

$$\text{RPM} = (\text{VFD Display \#}) * (\frac{38900}{667}) \qquad\qquad 3\text{-}8$$

7. Press the green start button.

8. While the rod is spinning, use a rough grit sandpaper to polish any surface oxidation off of the rod.

9. When it can be seen that the pin is spinning with no problems, stop the motor by pressing the red button on the remote keypad.

10. Move the catch pan forward until the face of the metal pin is ~1/8" from the tip of the welding electrode and centered.

3.2.5   Ramp Up & REP Initiation

1. Cycle to the desired rotational speed using Equation 3-8 and the VFDs remote keypad and press the green button to initiate spinning.

2. Keep a finger on the red button until the desired speed is reached in case rapid shutdown is required during ramp up.

3. After reaching the desired RPM, cover eyes with welding visor.

4. Press the foot troll pedal down until the arc is initiated.

5. Continue pressing the pedal down until the tip of the pin begins to melt (should be fully pressed down if max current was properly adjusted on the welder).

6. As the pin tip melts, maintain the ~1/8" distance between the pin and the electrode by using the crank on the carriage to move the catch pan closer to the spindle. Do not allow the electrode to touch the rotating pin as this will cause a short circuit and trip the VFD's breaker. If 'drilling' occurs, leaving a hollow shell, back off to allow the electric arc to cover and melt the shell.

7. Continue until the catch pan comes into contact with the spindle holder and you can proceed no further using the carriage crank.

8. Release the pedal and press the red button on the remote keypad to stop the rod from spinning.

3.2.6   Ramp Down

1. Ensure that the pedal is not depressed while ramping down the RPM (move aside with foot). The VFD mode should allow for minimum RPM while the brushes and slip ring cool off.

2. Ensure enough time is allowed for proper cooling of the metal rod (~5 minutes).

3. Turn off the VFD by flipping the circuit breaker to the down position.

4. Turn off the welder by flipping the front panel switch to the OFF position and unplugging the welder from its power source.

5. Close the water and argon lines.

6. Leave spindle cooling fan plugged in and on.

7. Wait until the metal rod is cool and then remove it from the collet.

8. The powder will be in the powder catch drawer at the bottom of the catch pan. Section 3.3 contains instructions on collecting and analyzing the powder produced by the rotating electrode process.

3.3   Powder Characterization

This section outlines the steps involved in handling and filtering the powder produced by the Rotating Electrode Process. Section 3.3.2 is presented as a formal, step by step procedure with numbered steps replacing paragraphs.

3.3.1 Powder Retrieval

To retrieve the powder from the catch pan after atomization, the catch pan assembly was moved away from the rod and lifted away from the carriage by unscrewing the four wing nuts at the catch pan's base. This was a two person job requiring access from both sides of the glovebox at the same time. Each person used one arm to grip the frame and lift the catch pan assembly up and back off of the rails and onto the glovebox floor. A 5/16 inch wrench was used to loosen and remove the bolts holding the catch pan's Plexiglas insert. A flathead screwdriver was used to loosen the screws holding the welding torch and the torch was lifted up and away from the catch pan. Careful attention was given not to puncture the gloves on the electrode's sharp point. A thick bristled brush was used to brush any remaining powder from the catch pan wall. Once all of the powder had collected at the bottom of the catch pan, the rubber stopper was removed and the powder was brushed into the catch drawer below. Any molten material that had resisted the brush and remained on the catch pan wall was removed using a narrow, stainless steel paint scraper. This powder was brushed into the catch drawer as well.

3.3.2 Powder Characterization

1. Calibrate a scale.

2. Place a brass basin on the scale and zero the scale.

3. Remove the catch drawer and hold it over the brass basin.

4. Carefully remove the foil covering the hole at the bottom of the drawer and allow the powder to spill out in the basin. Be careful not to allow any of the tape to touch the falling powder.

73

5. Place the basin, now holding the powder, back onto the scale.

6. Record the resulting value as "powder obtained".

7. Remove the basin and zero the scale.

8. Remove the remaining pin length from the RES.

9. Weigh the pin and measure its length. Record these values.

10. Label the pin with: the date, name of operator, type of metal, and experiment number.

11. Find the weight of "powder produced" by subtracting the remaining pin weight from the pin's initial weight before melting.

12. Subtract the weight of the "powder obtained" from the weight of the "powder produced" and record as "powder lost during retrieval".

13. Starting with a 710 μm sieve on top, stack the three largest sieve sizes on top of a second empty basin with the largest sized sieve on top and the smallest sieve on bottom. An example of the sieves used in the present study can be seen in Figure 3-41.

Figure 3-41: Brass sieve used to filter metal powder [42]

14. Place a plastic tray onto the scale and zero the scale.

15. Remove the tray, take off the cover of the tray, and place the base of the tray underneath the powder funnel, shown in Figure 3-42, (the base of the tray is recognizable as being the half with the widest bottom). The engineering sketch for the Teflon powder funnel is provided in Appendix B.

Figure 3-42: Teflon powder funnel

16. Pour the collected powder into the largest sieve.

17. Filter by tapping and shaking the sieve on top of the other two sieves until no more powder falls through.

18. Remove the largest sieve and the pour unfiltered contents into the powder funnel. Powder will be directed into the petri dish at the bottom.

19. Tap sieve on funnel to ensure all of the powder is dislodged.

20. Place the cover back onto the plastic tray base and place the tray back on the scale. Record the resulting value as the weight of powder produced in that particular size range.

21. Label the plastic tray with: the date, name of operator, experiment number, size range, type of metal melted, and powder weight in grams.

22. Repeat steps 13 through 21 with all of the remaining sieve sizes.

23. When finished filtering, add the recorded powder weights of each tray into one total and subtract this number from the "powder obtained" value to obtain the amount of powder lost during the characterization process.

24. Add this number to the amount of powder lost during collection from the catch pan to obtain a "total powder lost" value for the entire REP process.

4. RESULTS

Table 4-1: Overview of experiments performed

Rotating Electrode Material	Date (dd-mm-yy)	Environment (Argon/Air)	RPM	Current (A)	Diameter (Inches)
Copper	**05-Oct-12**	**Air**	**12,000**	**90**	**0.3750**
	05-Oct-12	**Air**	**18,000**	**90**	**0.3750**
	18-Oct-12	**Air**	**18,000**	**45**	**0.3750**
	16-Nov-12	**Air**	**10,000**	**90**	**0.3750**
	16-Nov-12	Air	11,000	90	0.3750
	26-Nov-12	Air	13,000	90	0.3750
	27-Nov-12	Air	14,000	90	0.3750
	28-Nov-12	Air	15,000	90	0.3750
	29-Nov-12	Air	16,000	90	0.3750
	08-Dec-12	Air	10,000	90	0.3750
	08-Dec-12	Air	12,000	90	0.3750
	09-Dec-12	Air	17,000	100	0.3750
	09-Dec-12	Air	18,000	90	0.3750
	17-Dec-12	Air	19,000	90	0.3750
	19-Dec-12	**Air**	**20,000**	**90**	**0.3750**
	03-May-13	Argon	13,000	90	0.3750
	24-Jun-13	Argon	15,000	100	0.3750
	16-Jul-13	Argon	15,000	100	0.3750
	19-Jul-13	Argon	15,000	100	0.3750
	30-Jul-13	Argon	15,000	100	0.3750
DU	25-Sep-13	Argon	12,000	40	0.4063
	08-Aug-13	Argon	15,000	50	0.4063
	12-Aug-13	Argon	15,000	40	0.4063
	15-Aug-13	Argon	15,000	40	0.4063
	23-Oct-13	Argon	14,000	50	0.4063
	04-Nov-13	Argon	13,000	50	0.4063
	04-Nov-13	Argon	16,000	50	0.4063
U-10Zr	**05-Dec-13**	**Argon**	**18,000**	**50**	**0.3750**
	09-Jan-14	Argon	16,000	125	0.3750
	21-Jan-14	Argon	15,000	125	0.3750
	24-Jan-14	Argon	14,000	125	0.3750

Table 4-1 gives a comprehensive list of the dates these tests were conducted, the RPM that was selected, and the amperage used by the rotating electrode for atomization. Data about rod lengths and weights before and after melting, the amount of powder collected, and the amount of powder lost during each step of characterization is provided in Appendix C. All of the experiments were conducted using a 2% thoriated, 1/8 inch diameter, sharpened tungsten electrode. Red, bold entries are experiments that did not produce usable powder or for which the powder could not be characterized.

4.1   Copper Powder

The TAMU RES was used to atomize 3/8 inch diameter copper rods in an air environment fifteen times before the system was installed inside an argon atmosphere glovebox. Five of the fifteen tests either did not produce powder or the powder that was produced could not be fully characterized by the method described in 3.2. The remaining ten experiments produced usable powder using rotational speeds that varied from 10,000 to 19,000 in 1,000 RPM intervals. Five tests were conducted in the argon atmosphere glovebox using 3/8 inch diameter copper rods to verify whether or not the argon would alter the powder production method or the resulting powder. It was determined that extra cooling inside of the catch pan was required to alleviate the conglomeration problem that arose due to argon's lower heat transfer coefficient, and to that effect a helium cooling line was added to the system (3.1.4.2).

The characterization of the copper powder produced using the RES is discussed in the following sections. An observed general trend was that increasing the RPM at which the rotating electrode was spun increased the mass percentage of smaller diameter powders while

decreasing the RPM increased the mass percentage produced of larger diameter powders. Pictures of the powder were taken with a Hirox digital microscope (model KH-1300) and are included in the following sections.

One challenge that was observed is worth noting before moving on to the powder characterization results. The 2% thoriated tungsten TIG electrode was not re-sharpened or sanded to remove any surface impurities for the four copper tests and three uranium tests conducted between 24-June-2013 and 15-August-2013. As a result, during a test on 18-August-2013 the current from the welder arced through the protective handle of the torch head to the aluminum torch holder, causing the system to short and the breaker to close. A small hole was burned through the protective torch handle as shown in Figure 4-1. It was hypothesized that the buildup of impurities on the tungsten electrode tip provided resistance and that the current took an easier pathway through the handle cover to the aluminum torch holder. A new torch handle cover was purchased and the arcing effect was eliminated by sanding and sharpening each tungsten electrode on a grind-stone before each operation of the RES.

Figure 4-1: Hole burned through the torch handle cover as a result of arcing

A second failure worth highlighting for future reference arose during the 18-October-2012 test that was performed at 18,000 RPM and with 45 A of current. The test was carried out to determine what effect, if any, atomizing the copper rod using a lower amperage would have on the resultant powder. However, no powder was produced.

Instead, the copper rod was heated to a malleable state (without melting) and the small rotational imbalances present in the rod caused it to bend sharply at a right angle relative to the collet as shown in Figure 4-2 and Figure 4-3. The torque induced by rotating the rod in this shape caused the rod to come into contact with the collet shield, forcibly stopping rotation. The VFD logged the sudden stoppage of the motorized spindle and caused the breaker to close, shutting off the RES. It was very difficult to remove the bent rod from the RES and may have proved impossible if it had happened inside of the glovebox where work

80

space and freedom of movement are limited. It is thereby concluded that any attempt to atomize metal with the RES using insufficient amperage would not be advisable.

Figure 4-2: Bent copper rod
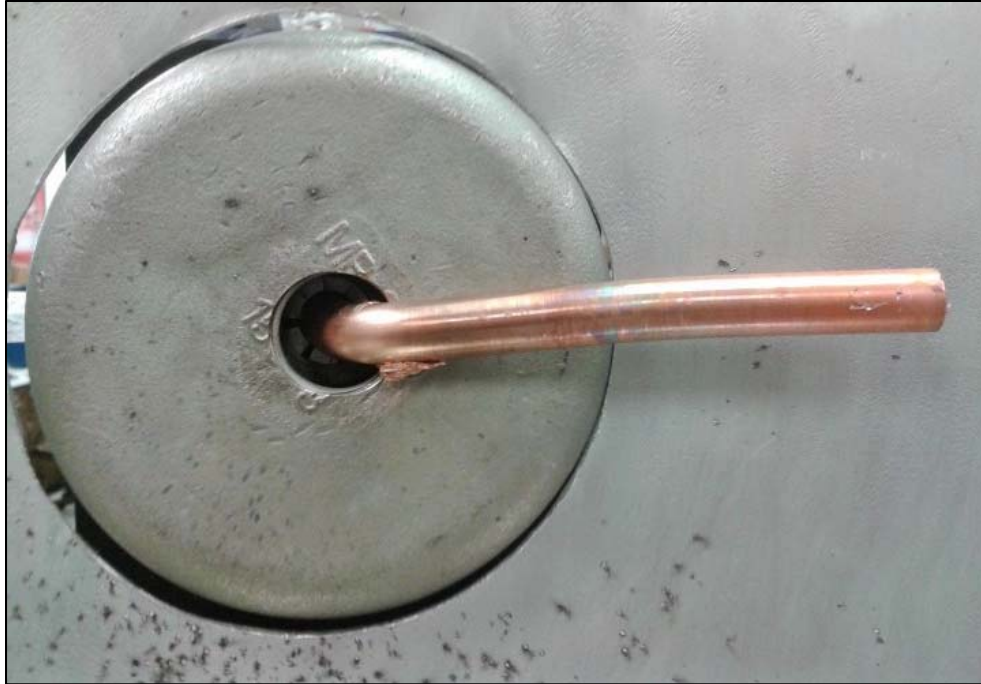
Figure 4-3: Close up of bent copper rod

4.1.1   Mass Percent Yield vs. Microsphere Diameter (Copper Powder)

This section presents the results of copper powder characterization in terms of the size range of the powder versus the mass percentage yields of the total powder collected. Figure 4-4 shows photos of the melt-tips of two copper rods. The rod on the right was melted in an air atmosphere and the one on the left was processed in an argon atmosphere. Copper rods processed in air always exhibited discoloration and a buildup of carbonized "ash" on the rod's surface. Rods that were processed in argon did not exhibit any discoloration or carbon build-up.

**Figure 4-4: Contrast between copper rods melted in argon (left) and air (right)
atmospheres**

Figure 4-5 presents the mass-based particle size distribution (determined by sieving) from
the first RES produce from a copper rod inside the glovebox at 13,000 RPM and 90 A
(without a helium cooling line installed) compared to the powder results of the RES operated
in air at the same current and RPM. From this data comparison, it can be seen that copper did
not melt as readily in an argon atmosphere as it did in air. This is supported by the
observation during operation that it took longer to create a puddle of molten metal on the face
of the rod when initiating an arc in the glovebox than it did in air. The poorly heated molten
copper on the rotating tip did not behave in the same manner as the air-melted material. The
liquid may have been at a lower temperature due to the sluggish heating in an argon
environment. The liquid release was somewhat sluggish as well, which produced larger
diameter powder. To compensate for this observation, the amperage was increased to 100 A
for the next four copper tests of the RES.
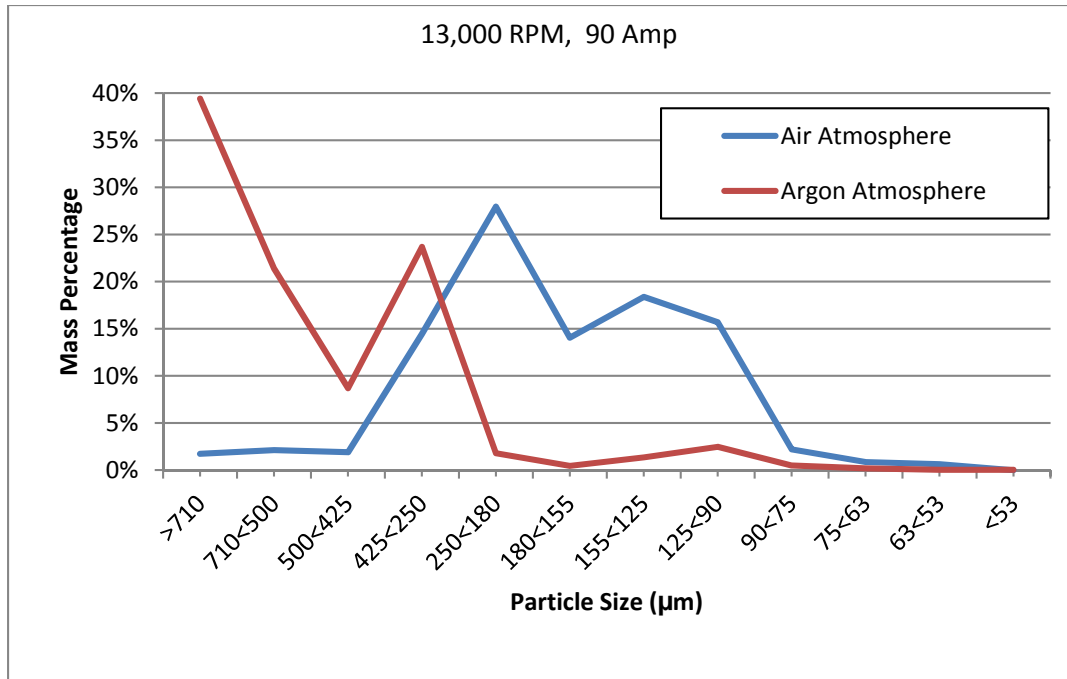
Figure 4-5: Contrast between copper particles produced in air and argon environments

The impact of the helium cooling gas in the glovebox RES system on the resulting particle size distribution was dramatic. Figure 4-6 shows the mass-based particle size distribution for a test conducted at 15,000 RPM and 100 A without a cooling gas, while Figure 4-7 shows the powder characterization results for a test conducted at the same RPM and current but in the presence of a 20 cfh helium flow inside the catch pan. The shift from preferentially large powder mass percentages to a distrubition more often seen in subsequent powder characterizations was the direct result of the helium coolant cooling the copper microspheres enough to prevent coagulation and sticking en-route to the catch pan wall.
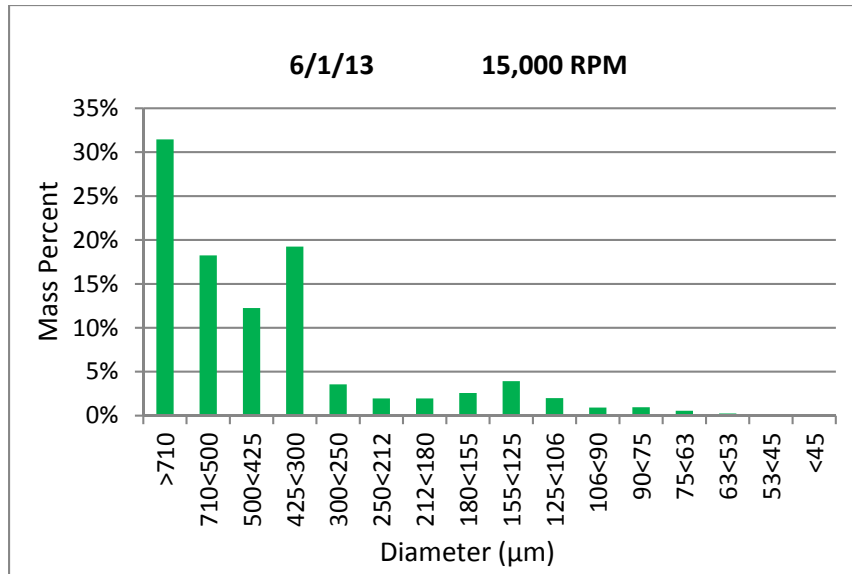
**Figure 4-6: Mass-Based particle size distribution for copper powder produced without
a helium cooling flow**
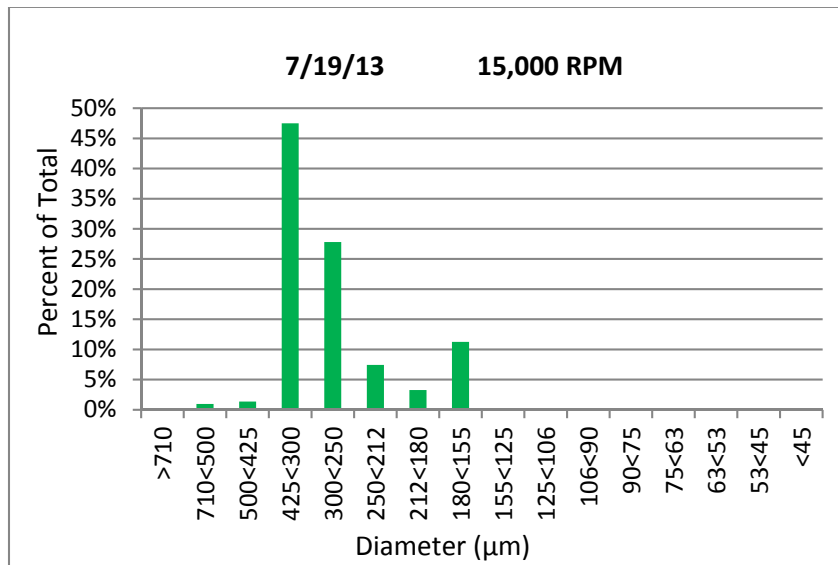
**Figure 4-7: Mass-Based particle size distribution for copper powder produced with a 20
cfh helium cooling flow**

Figure 4-8 presents the particle size distributions for copper powders made using

rotational speeds ranging from 10,000 RPM to 18,000 RPM. As the rotational speed of the

85

rod increases, the percentage of larger particles (i.e., in the 250 to 425 μm range) is noticeably reduced. This correlation is notable between speeds of 10,000 and 16,000 RPM since a further increase to 18,000 RPM does not produce as dramatic a reduction. It is also worth noting that a finer particle size category (i.e., 90 to 125 μm) begins to become more prominent above 12,000 RPM. This second peak rises and broadens as rotational speed is increased. The effect is more clearly seen in Figure 4-9, which contrasts the 10,000 RPM powder results with the 18,000 RPM powder results.
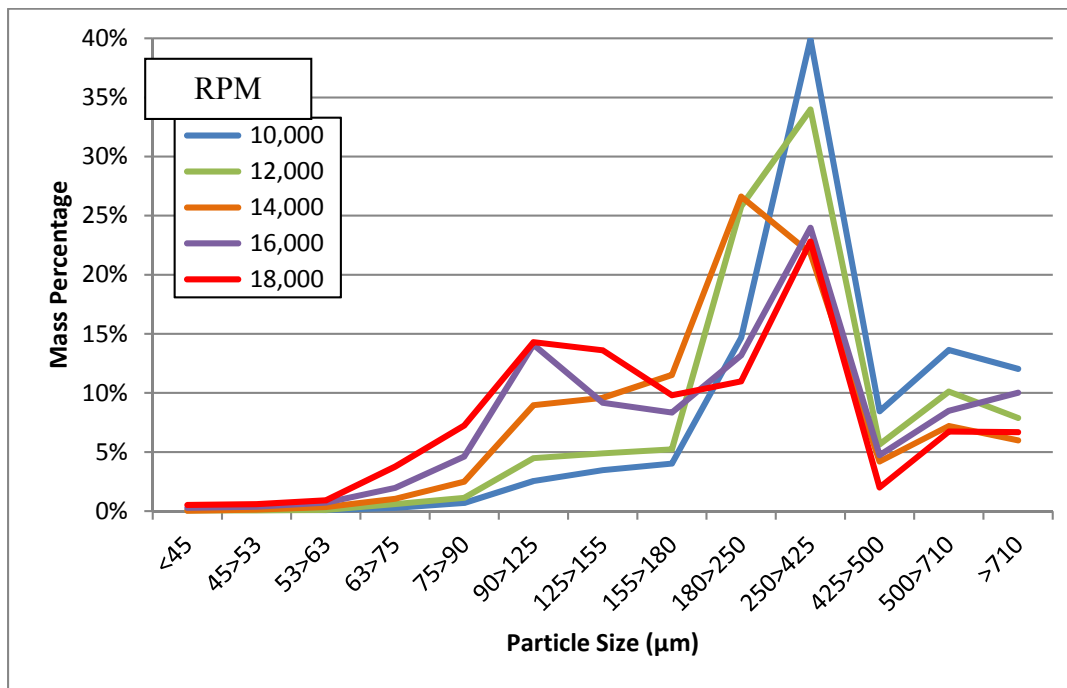
Figure 4-8: Mass-Based particle size distribution for copper produced at varying rotational speeds
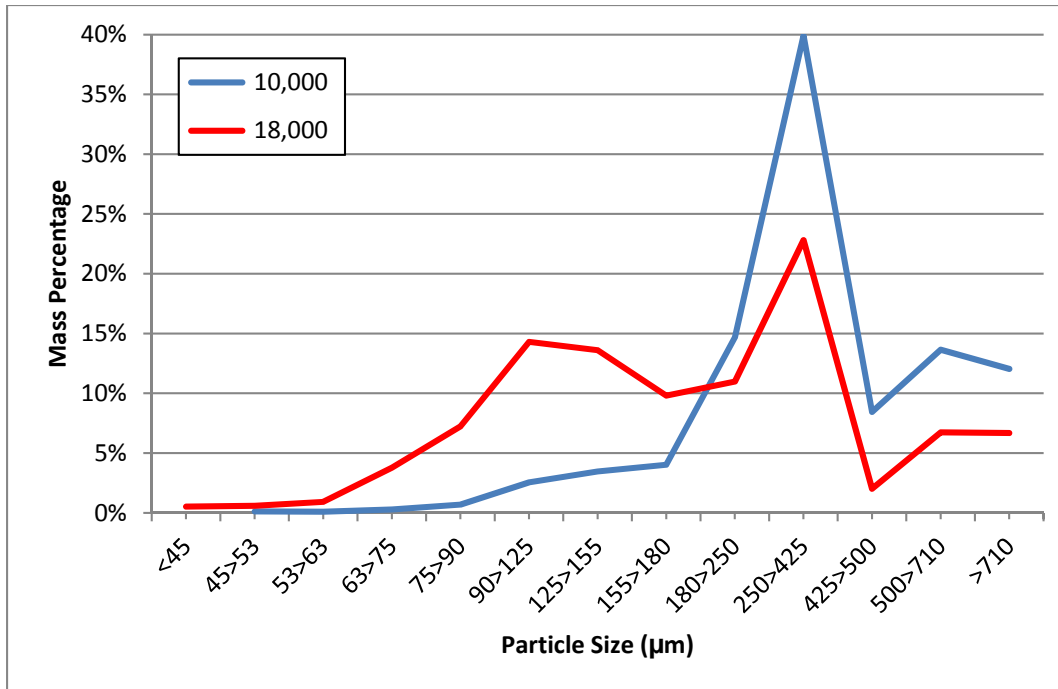
Figure 4-9: Contrast between copper powder production at rotational speeds of 10,000 and 18,000 RPM

4.1.2 Comparison of Size Distributions with Rotational Speed

This section presents the particle size data from the sample powder production tests in the previous section in relation to the rotation speed of the source electrode. Figure 4-10 presents the variation of the mass percentage of every size range as a function of the rotational speed of the source electrode. Size ranges below 180 μm generally exhibit an increase in mass percentage as rotational speed increases, while size ranges above 180 μm exhibit a general trend of decrease. This data may prove useful to future users trying to maximize the powder production of a specific size range. However, the production behavior as a function of rotational speed for a particular size range in copper may not transfer to other materials. Evidence to the contrary is provided by the differences between copper and uranium

production as a function of rotational speed. Figure 4-11 provides a less complicated comparison of the particle size variations with rotational speed.
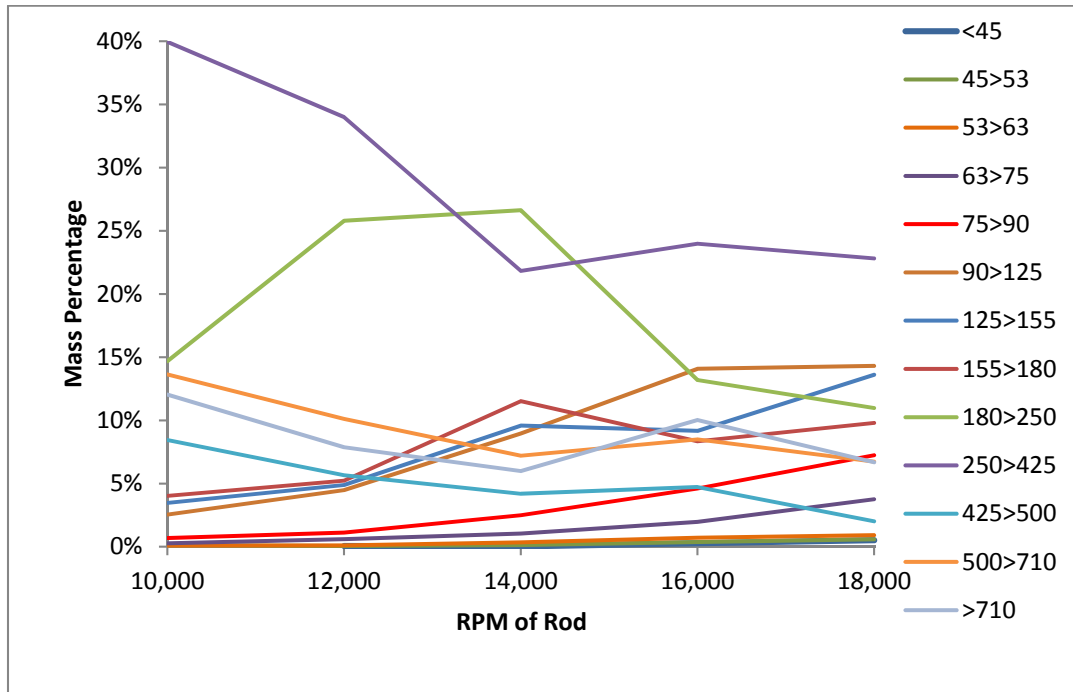
Figure 4-10: Mass distributions segregated by particle size ranges for copper powder produced at varying rotational speeds
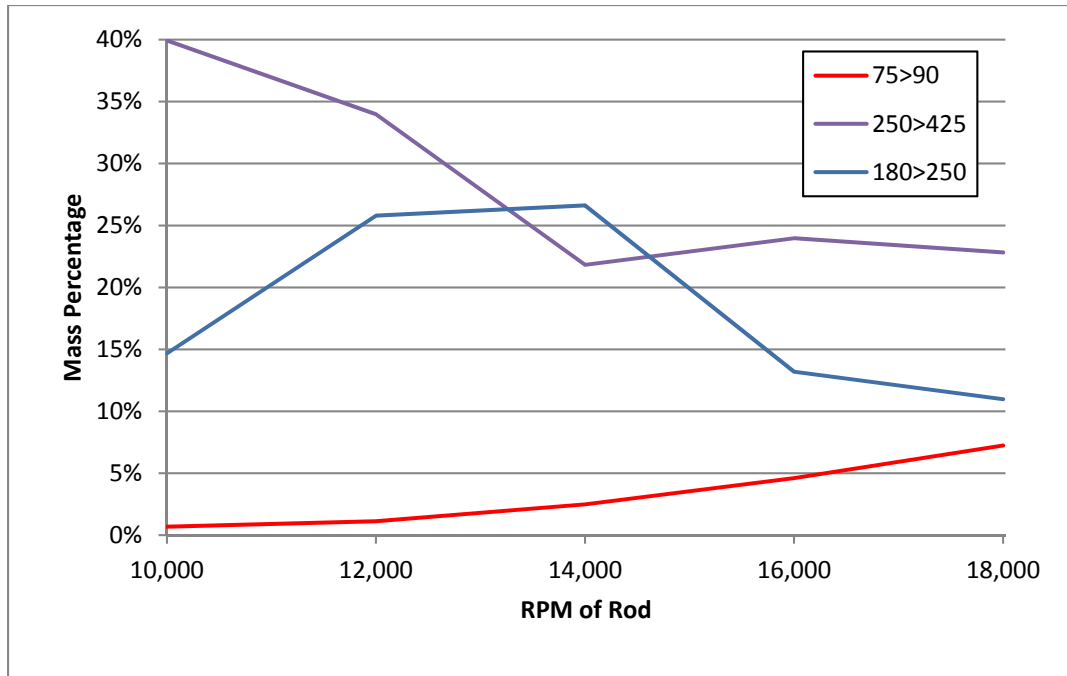
Figure 4-11: Mass distributions for selected small, medium, and large particle size ranges for copper powder produced at varying rotational speeds (same data as Figure 4-10)

4.1.3   Copper Microspheres Examination

The copper powder produced by the RES was examined using X-ray diffraction (XRD) and optical microscopy. It was determined from the XRD results that the powder did indeed form a crystalline structure upon solidification rather than becoming amorphous during the atomization process. From the microscope images, it was observed that much of the powder formed was spherical although there were irregularly shaped particles as well, especially for large particle sizes.

4.1.3.1   XRD

X-ray diffraction is a chracterization technique that can identify a crystalline substance by analysing the intesity and angles at which generated x-rays are diffracted through the

substance. If the material being analysed has a crystalline structure, the x-rays will be diffracted at specific angles and intesities based on the repeatable patern of the material's atomic structure. Combined with some previous knowledge about the material being sampled, x-ray diffraction can also help determine the relative amounts of any impurities or solid phases within a sample [42]. The x-ray diffraction analysis was conducted using the Texas A&M Geology Department's Rigaku diffractometer [43].

Fourteen copper powder samples from three rotational speeds were prepared for XRD analysis. Samples were prepared and labeled on glass slides as pictured in Figure 4-12. Four 11,000 RPM samples were prepared from the size ranges of 63 to 75 μm, 90 to 106 μm, 125 to 180 μm, and 180 to 250 μm. Four 13,000 RPM samples were prepared from the size ranges 63 to 75 μm, 90 to 106 μm, 106 to 125 μm, and 180 to 250 μm. Six samples were prepared from the size ranges of less than 45 μm, 45 to 53 μm, 63 to 75 μm, 90 to 106 μm, 106 to 180 μm, and 180 to 250 μm. The powders from each size range were mounted onto the glass slides using an acetate soluble bonding agent to immobilize the powder. Before the bonding agent dried, the powder was pressed flat onto the slide so that it would fit into the narrow slide opening in the diffractometer.
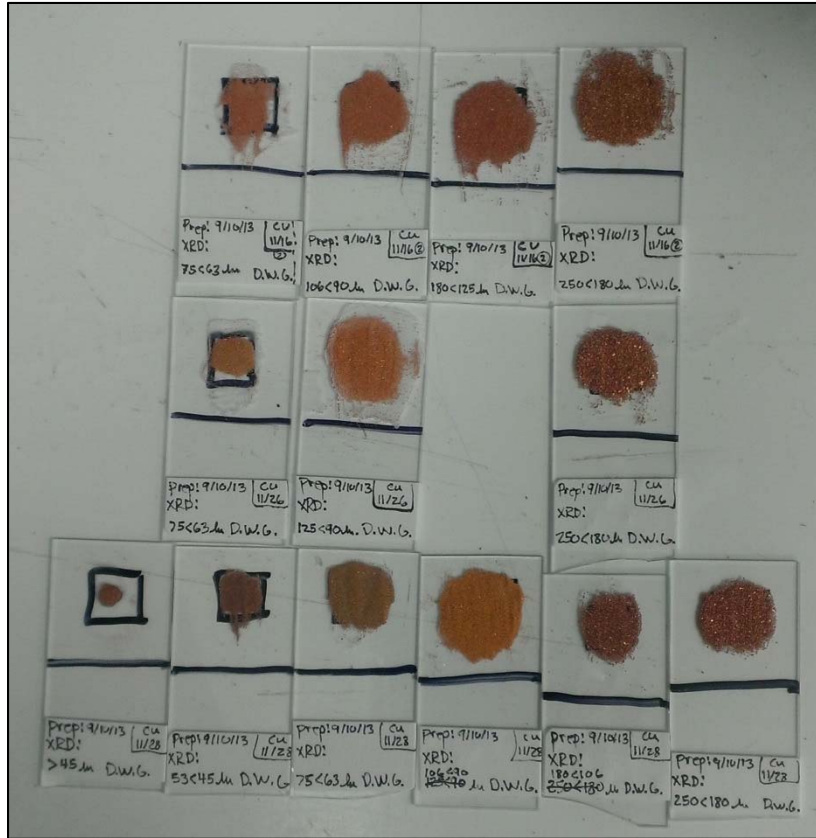
Figure 4-12: Completed x-ray diffraction copper powder samples

All of the samples exhibited the same three peaks of intensity at diffraction angles of approximately 43.4, 50.5, and 74.2 degrees shown in Figure 4-13. The height of the peak denotes the intensity of the diffracted x-rays at that angle. The d-spacing number is the interplanar spacing that corresponds to the h, k, and l planes that caused the formation of the x-ray reflection. The angle where each peak is located represents the relative position of the detector as it moves around the material being analyzed [42]. All fourteen copper powder samples returned a variation of the same three peaks shown in Figure 4-13 with varying intensity values but always the same angle position and d-spacing values. The measured d-spacing values matched benchmark d-spacing values known for copper, indicating that the

copper powder produced by the RES formed crystal structures and were therefor not amorphous.
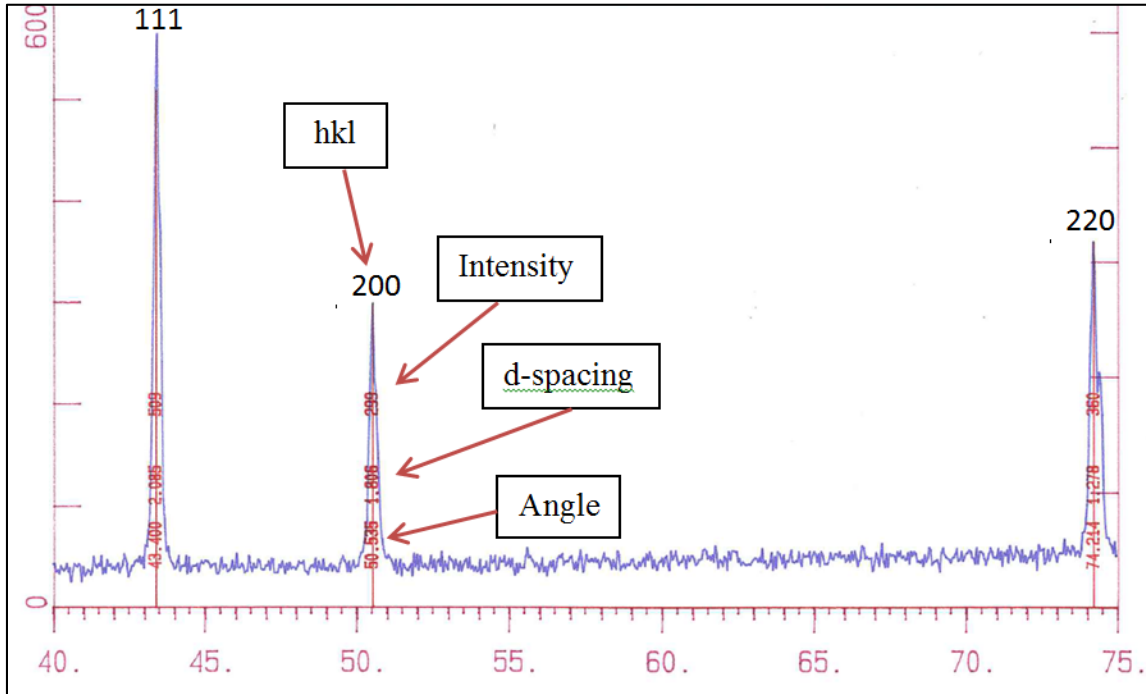
Figure 4-13: Sample XRD plot of analyzed copper powder produced by the RES

4.1.3.2 Optical Microscope Images

Figure 4-14 shows a sample of copper powder in its raw form, before separation for analysis. Most of the powder particles are sphereical but some non-sphereical formations are evident. Most notably, the non-sphereical pieces take the form of (1) a "splatter" where part of the orignal sphere is sometimes still evident as a hump in the center of the flake (Figure 4-15), (2) a long shard of material (Figure 4-16), (3) a cluster of spheres that have stuck to each other (Figure 4-17), or (4) a slightly mishapen sphere.
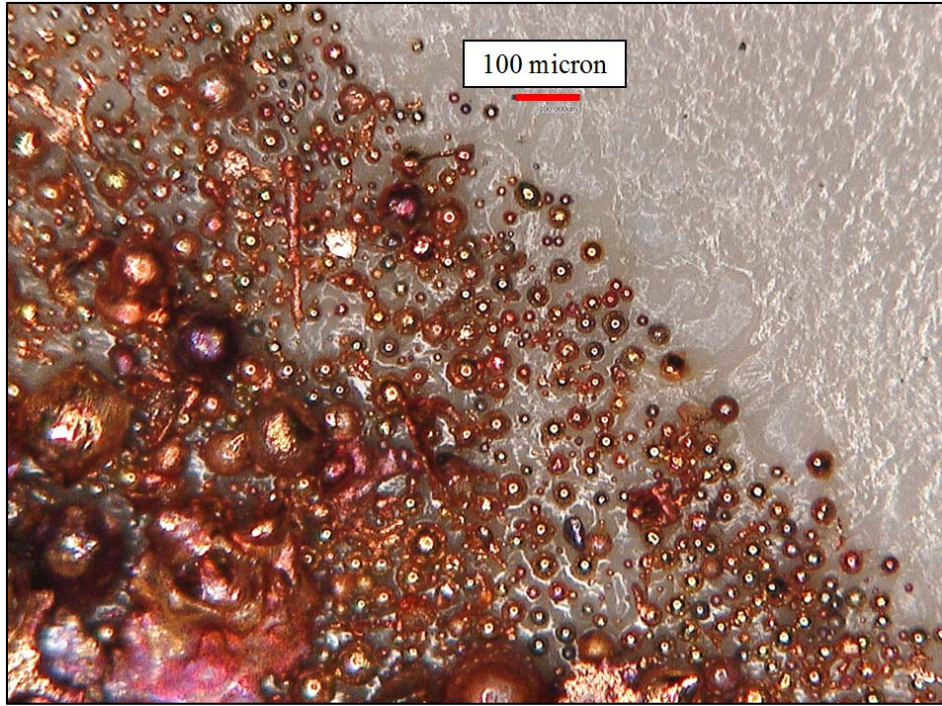
Figure 4-14: Bulk copper powder produced by the TAMU RES
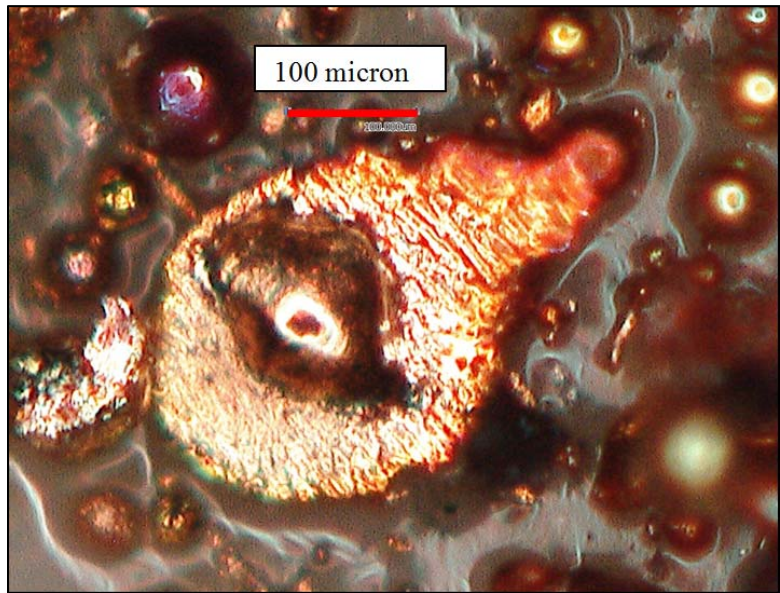
Figure 4-15: "Splatter" formation
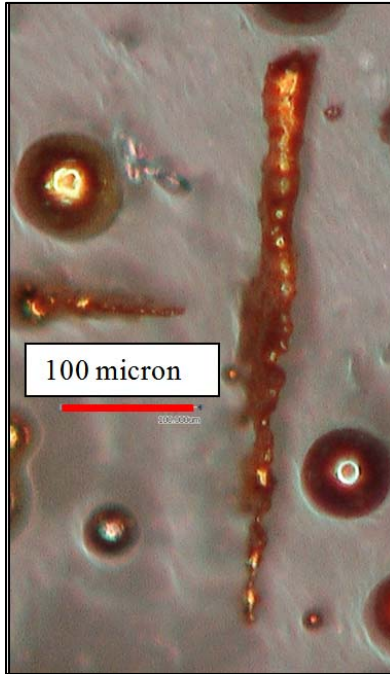
Figure 4-16: Shard formation
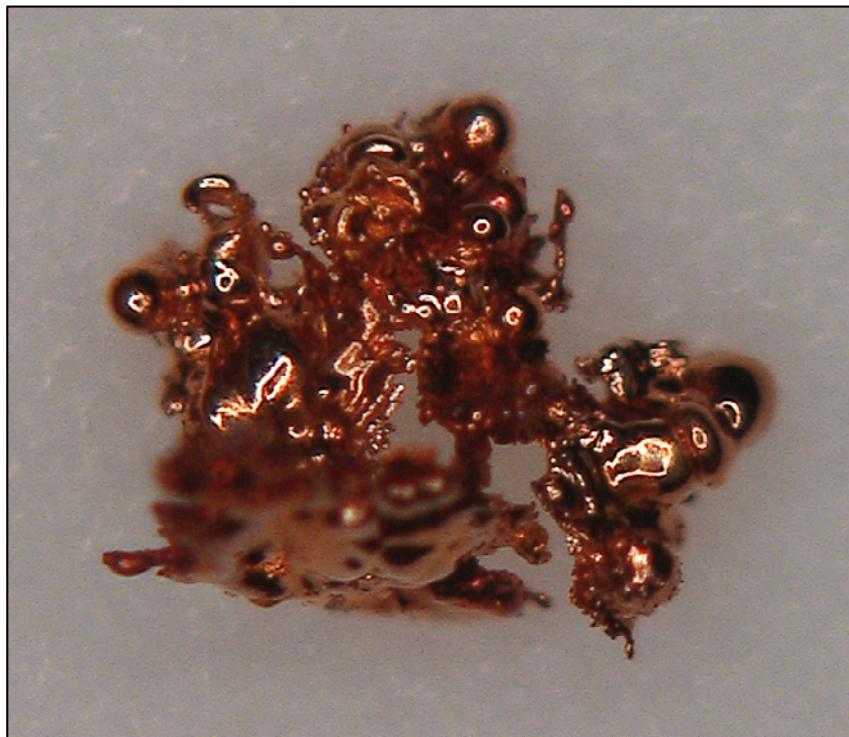
Figure 4-17: Sphere cluster formation

Figure 4-18 shows a powder sample taken from the 75 to 90 μm size range after sieving. Most of the particles are spherical with some particles exhibiting a tail; a result of never breaking away from their stream of molten metal before surface tension started forming the sphere. Figure 4-19 presents a good example of the transitional stage that the molten metal undergoes during the atomization process. Molten metal is flung radially away from the rotating electrode in long strings of material. The strings separate into smaller pieces, which coalesce under surface tension to form spheres. The string in Figure 4-19 hardened during the separation process; before the pieces had fully separated but after the microspheres had started to form.
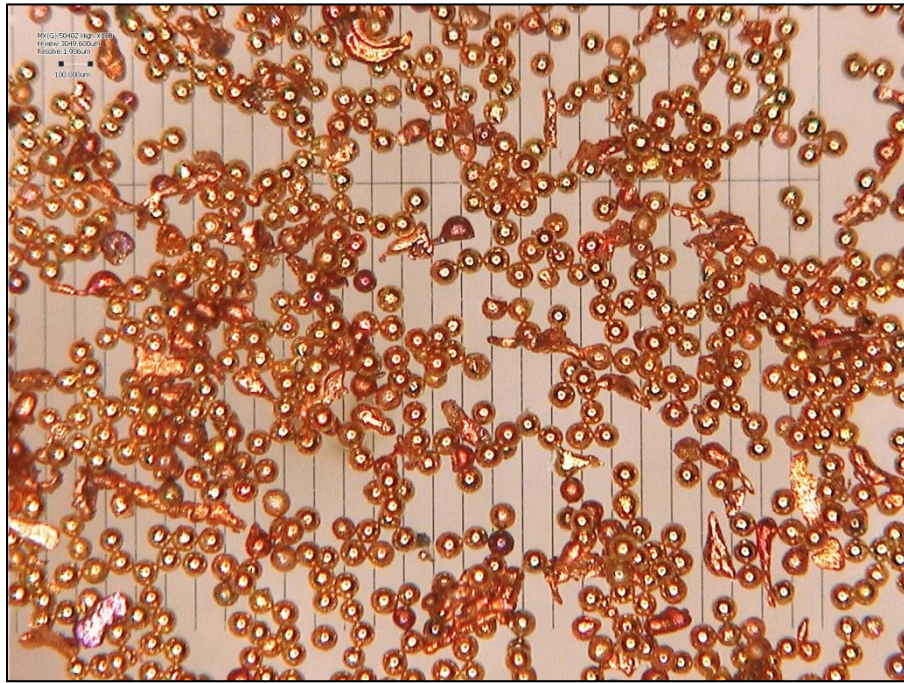
Figure 4-18: Copper microspheres taken from the 75 to 90 μm size range on a 100 μm background
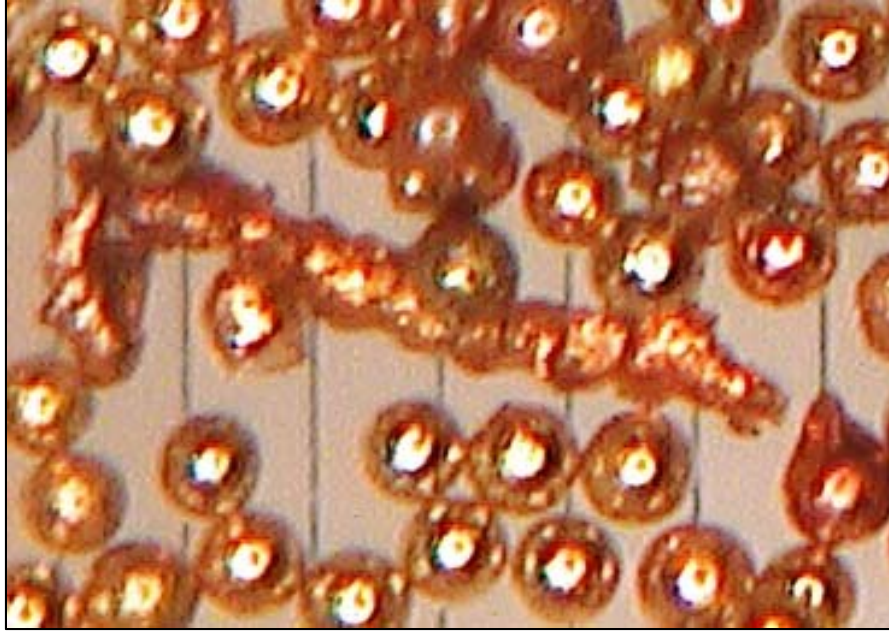
Figure 4-19: String of molten droplets on a 100 µm background

When observed individually under high magnification, the microspheres showed strong sphericity and appeared to have some surface roughness. They retained their copper coloring and did not show any of the oxidation inherent in the powder samples produced by Thompson in Figure 4-20 [1]. Figure 4-21 and Figure 4-22 show individual microspheres at high magnification on 20 and 100 µm backgrounds, respectively.
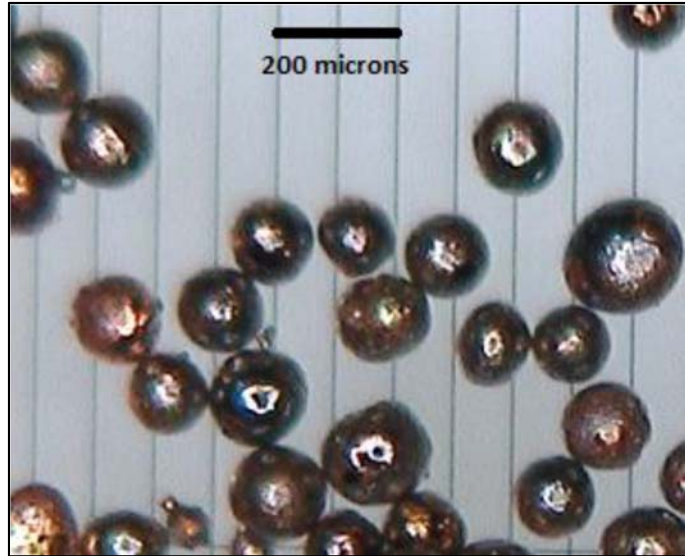
Figure 4-20: Copper microspheres produced by Thompson [1]
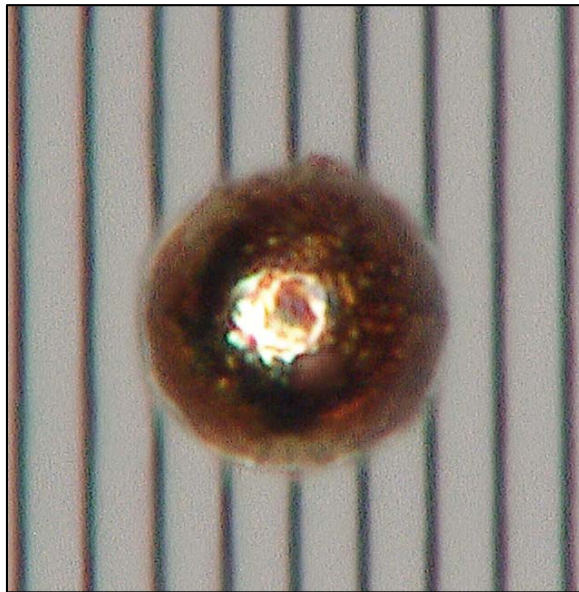
Figure 4-21: Copper microsphere taken from the 75 to 90 μm size range on a 20 μm background
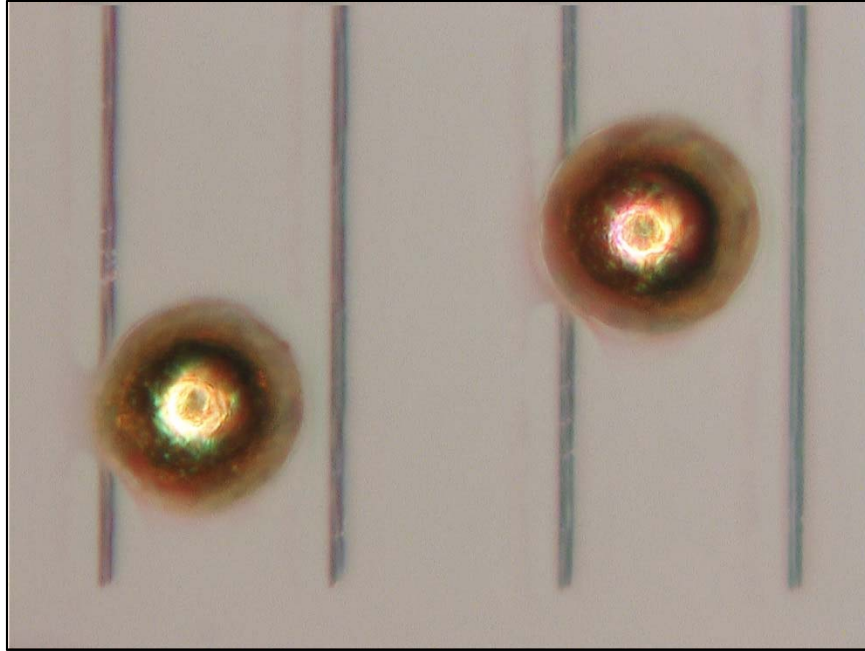
Figure 4-22: Copper microspheres from the 75 to 90 μm size range on a 100 μm background

4.2 Uranium Metal Powder

Seven tests of the TAMU RES were conducted using 13/32 inch (1.032 cm) diameter uranium metal rods. To remove the surface oxidation, the rods were inserted into the RES and rotated at low speed and the surface was removed rough-grit sandpaper. Three of the seven tests were conducted at 15,000 RPM to verify that the RES was capable of repeating results between multiple usages. A notable incident occurred during the preparation of the uranium rod used in the first test. An overlong nitric acid solution bath caused a loss of material in the rod and may have been a contributing factor to the failed test. A more detailed record of the occurrence can be found in Appendix D.

4.2.1   Mass Percent Yield vs. Microsphere Diameter (Uranium Powder)

This section presents the results of uranium metal powder characterization in terms of the size range of the powder versus the mass percentage yields of the total powder collected.

It was important to know that the RES could repeatedly produce powder with consistent properties. Figure 4-23 shows the powder characterization results of three production tests using uranium metal source rods, operating at 15,000 RPM with helium cooling gas flowing inside the catch pan. The tests used currents of 40, 50, and 50 A, respectively. It was confirmed that the RES produces reproducible results, with the largest yield difference between the three tests (~53%) occurring in the 250 to 212 μm range. Yield differences below 180 μm were deemed to be within acceptable ranges for an in-house system that was not designed for industrial production.
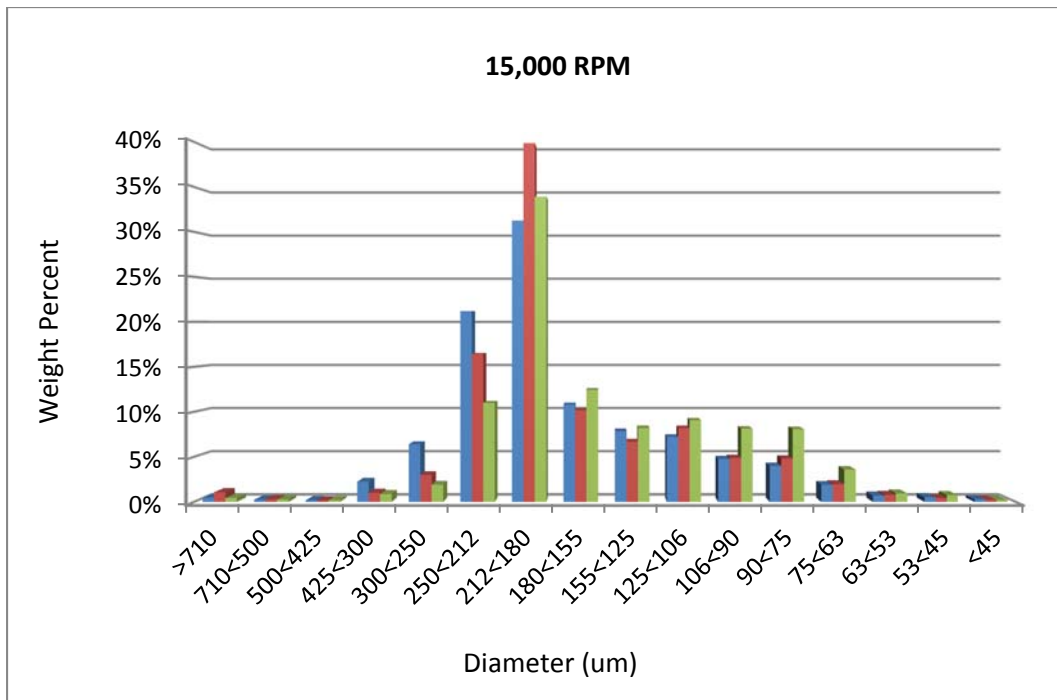
Figure 4-23: Mass-Based particle size distribution for uranium metal particles produced at 15,000 RPM

99

Figure 4-24 presents the uranium metal powder characterization results for rotational speeds ranging from 12,000 RPM to 16,000 RPM. Similar to the copper results, as the rotational speed increases, the quantity of larger powder particles degreases. However, this effect is not as strong as it is in copper. Unlike the copper results, the peak particle size produced shifts towards smaller powder sizes as rotational speed is increased. Further, while a second peak representing finer powder production is not as pronounced as in copper, it still exists and is much wider than in copper. This implies that as the rotational speed is increased, a greater percentage of smaller size powder is produced. The smaller, secondary peak is evident at an RPM of 13,000 and the shifting and widening effects of the peaks are evident at RPMs of 15,000 and 16,000. The effects can be more clearly seen in Figure 4-25, which consolidates the 12,000, 14,000 and 16,000 RPM powder results on a separate graph. Rotational imbalances introduced by the uranium rods' lack of straightness caused a determination not to perform any experiments above 16,000 RPM for safety.
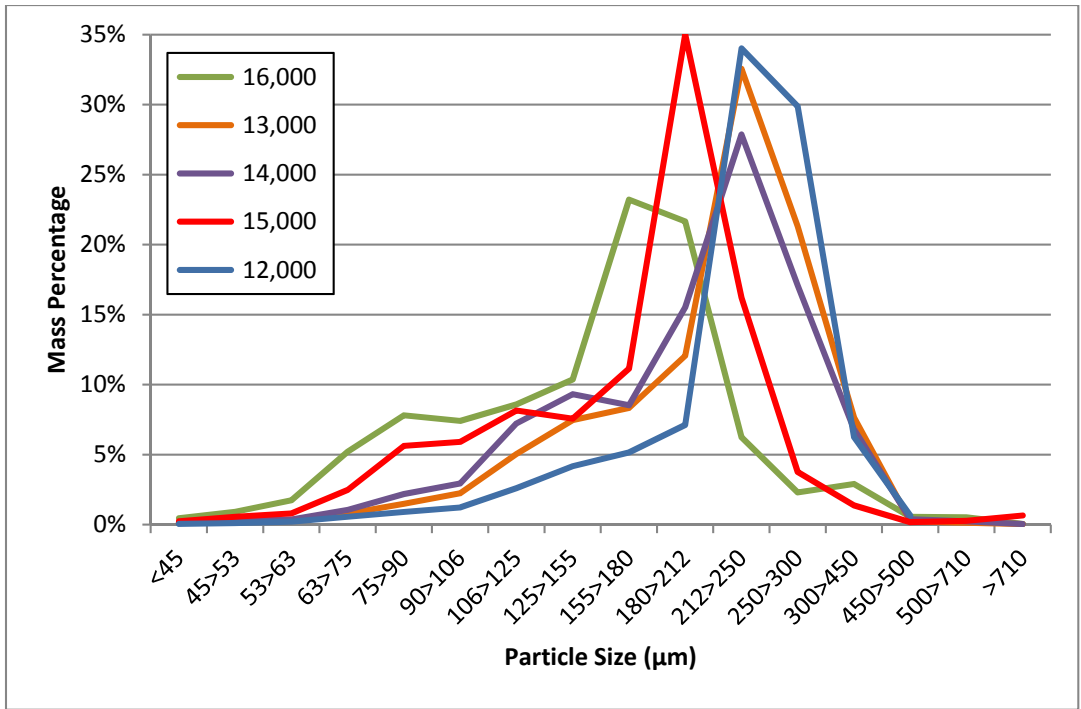
Figure 4-24: Overview of uranium powder yield percentage versus powder size at varying rotational speeds
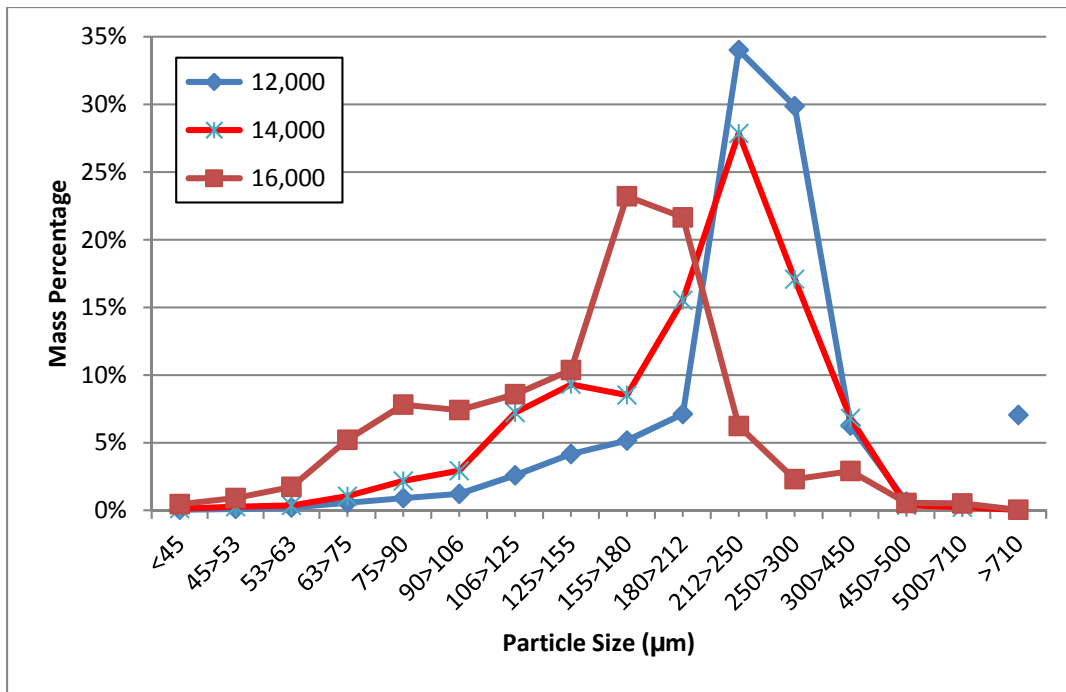
Figure 4-25: Contrast between uranium powder production at rotational speeds of 10,000, 14,000, and 18,000 RPM

4.2.2 Mass Percent Yield vs. Electrode Rotational Speed

This section presents the results of uranium metal powder characterization as a function of rotational speed. Figure 4-26 depicts the mass percentage of every size range as a function of RPM. Size ranges below 212 μm generally exhibit an increase in mass percentage as rotational speed increases, while size ranges above 212 μm exhibit a general trend of decrease. The size range of 180 to 212 μm stands out by not fitting into either category; showing a sharp increase in percentage produced until 15,000 RPM where a sharp decrease occurs. It is again noted how the powder production distribution for uranium does not match that of copper and that each material has a distinct, repeatable distribution as a function of rotational speed. Figure 4-27 and Figure 4-28 provide a better contrast of the production behavior between smaller, medium, and larger powder size ranges as a function of RPM.
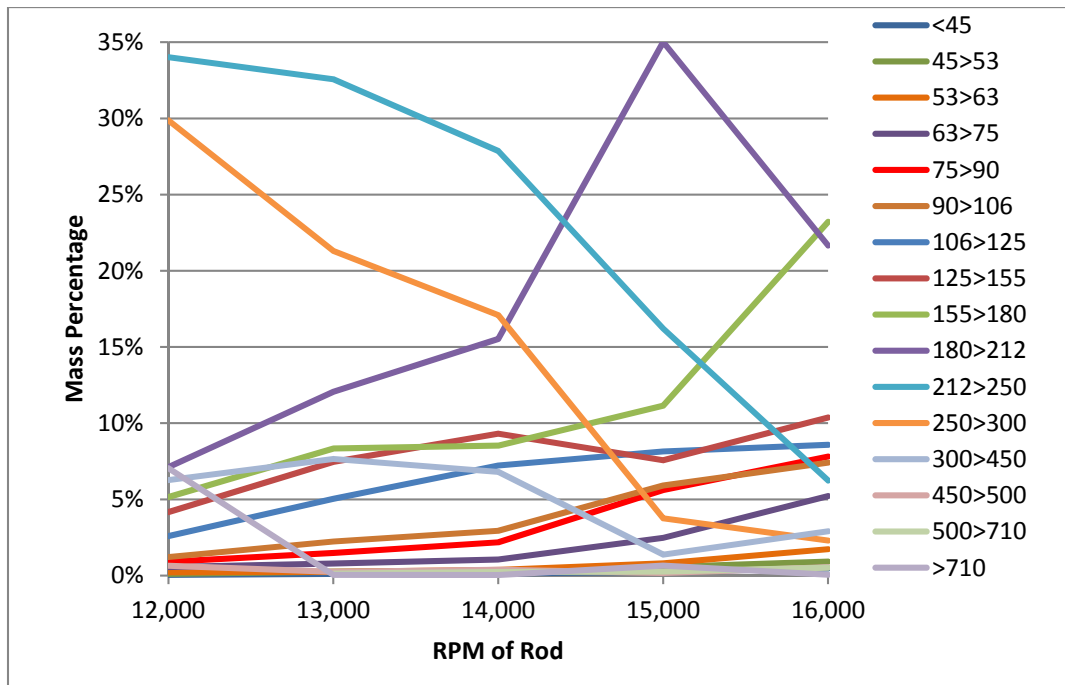
Figure 4-26: Overview of uranium powder production percentages as a function of rotational speed
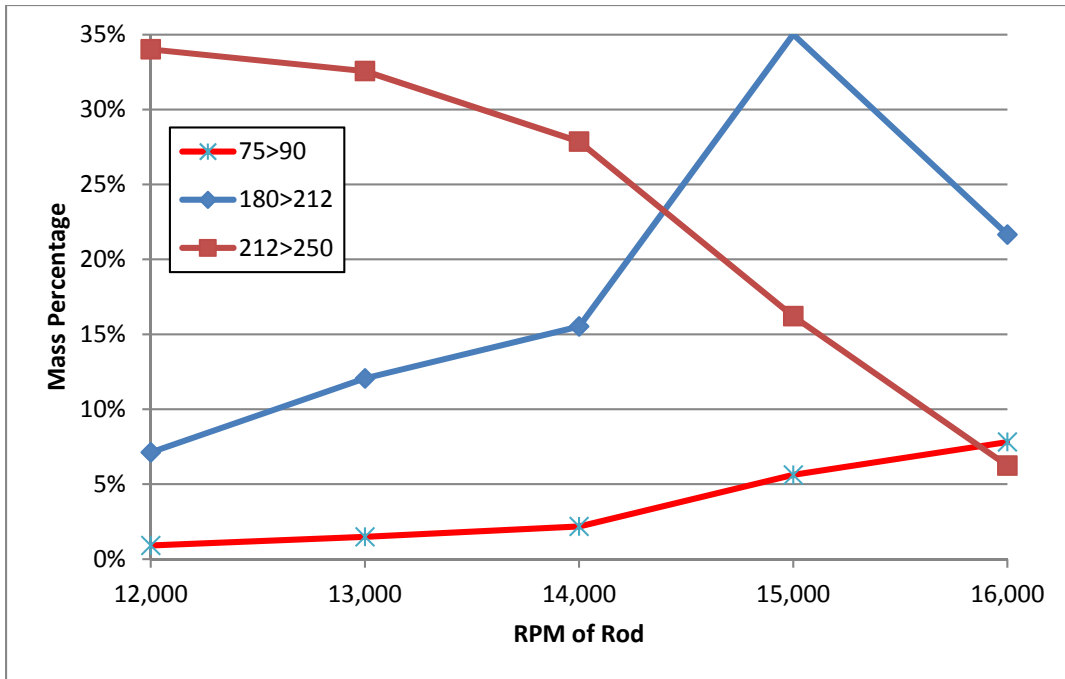
Figure 4-27: Contrast between large and small size uranium powders produced as a function of rotational speed
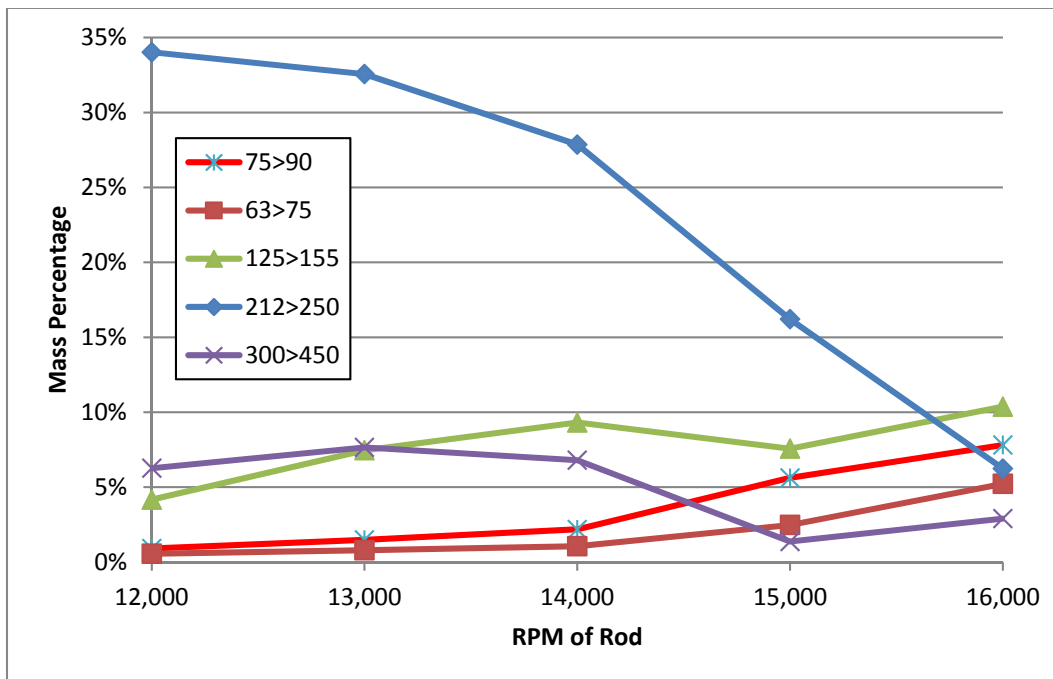
Figure 4-28: Contrast between large, medium, and small size uranium powders produced as function of rotational speed

4.2.3 Imaging of Uranium Metal Microspheres

Figure 4-29 and Figure 4-30 depict uranium powder before characterization and the melt tip of a uranium rod after atomization. The rods did not show as much of a bowl feature after melting as the copper rods did. However, the bowl feature is largely influenced by how close the user keeps the tungsten electrode to the face of the rotating electrode during operation, and does not seem to affect the powder. Also, the rods were melted using much lower currents than the copper rods. This may have reduced the penetration depth of the arc.

Figure 4-29: Uranium powder before characterization

Figure 4-30: The Melt tip of a uranium rod after atomization

The uranium powder produced at rotational speeds of 13,000 and 16,000 RPM were imaged using the Hirox digital microscope. The powder was highly spherical, lacking shard, splatter, or conglomeration formations inherent in the copper powder. The microspheres exhibited a shiny surface and lacked the same degree of surface roughness exhibited by copper and U-10Zr powders. The only physical difference that could be detected between microspheres produced at 13,000 RPM and microspheres produced at 16,000 RPM were the shape of the non-spherical powder artifacts. Any non-spherical artifacts observed in the powder produced at 13,000 RPM took the form of the "slugs", or elongated spheres shown in the left image of Figure 4-31. Non-spherical artifacts observed in the powder produced at 16,000 RPM took the form of the long, curved "worms" shown in the right image of Figure 4-31.
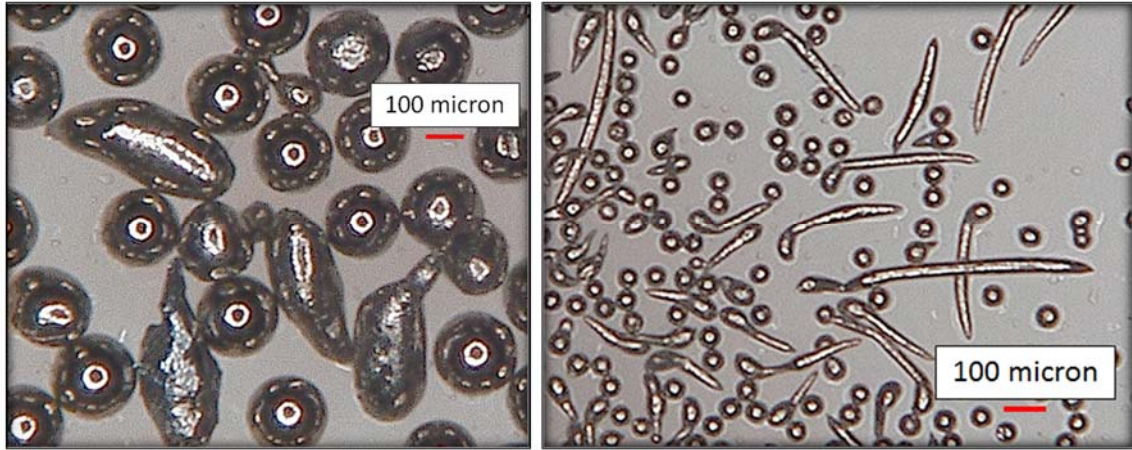
Figure 4-31: Difference in non-spherical powder formations between 13,000 RPM and 16,000 RPM powders

Figure 4-32 shows uranium powder produced at 13,000 RPM viewed at 100 and 600 times magnification. Figure 4-33 shows uranium powder produced at 16.000 RPM viewed at 200 and 800 times magnification. It appears as if powder produced at 16,000 RPM has more surface roughness than powder produced at 13,000 RPM.
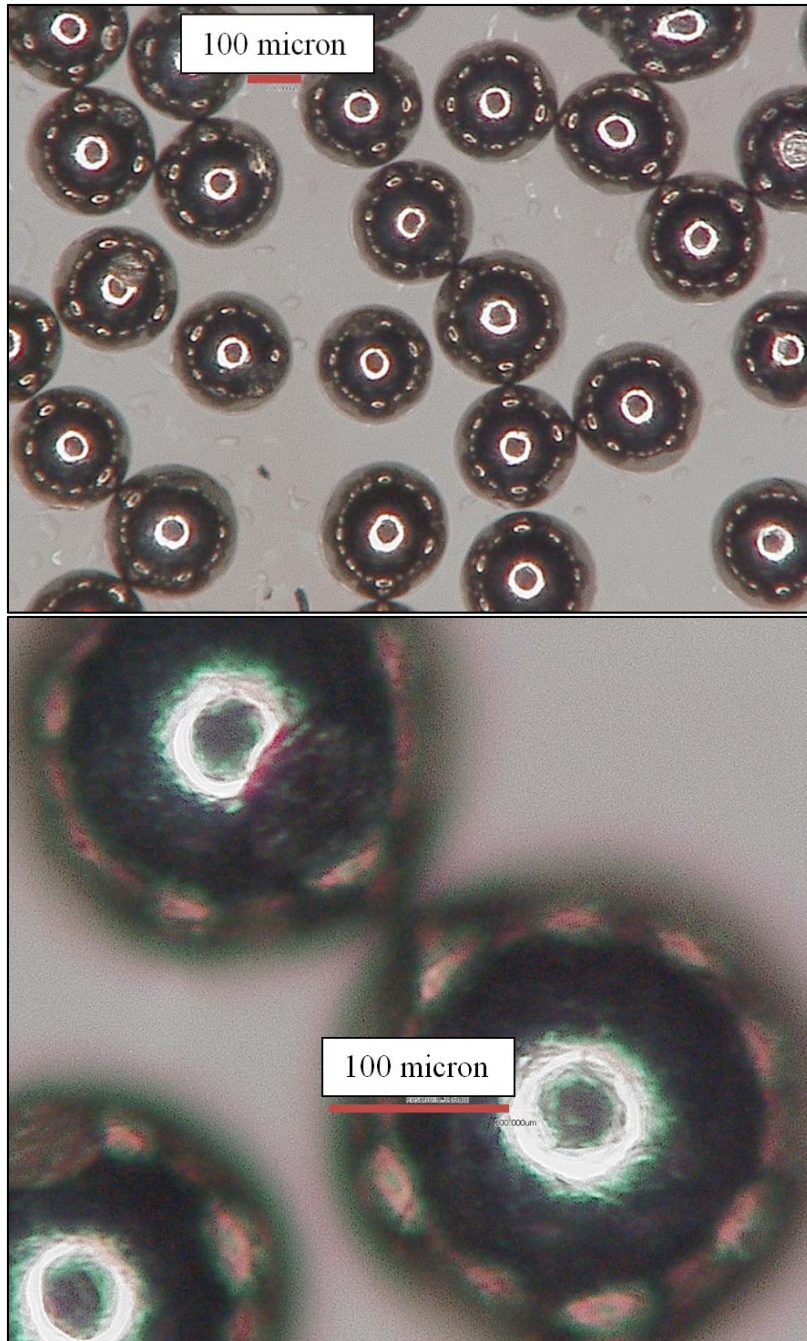
Figure 4-32: 13,000 RPM uranium powder seen at 100x (above) and 600x (below) magnification
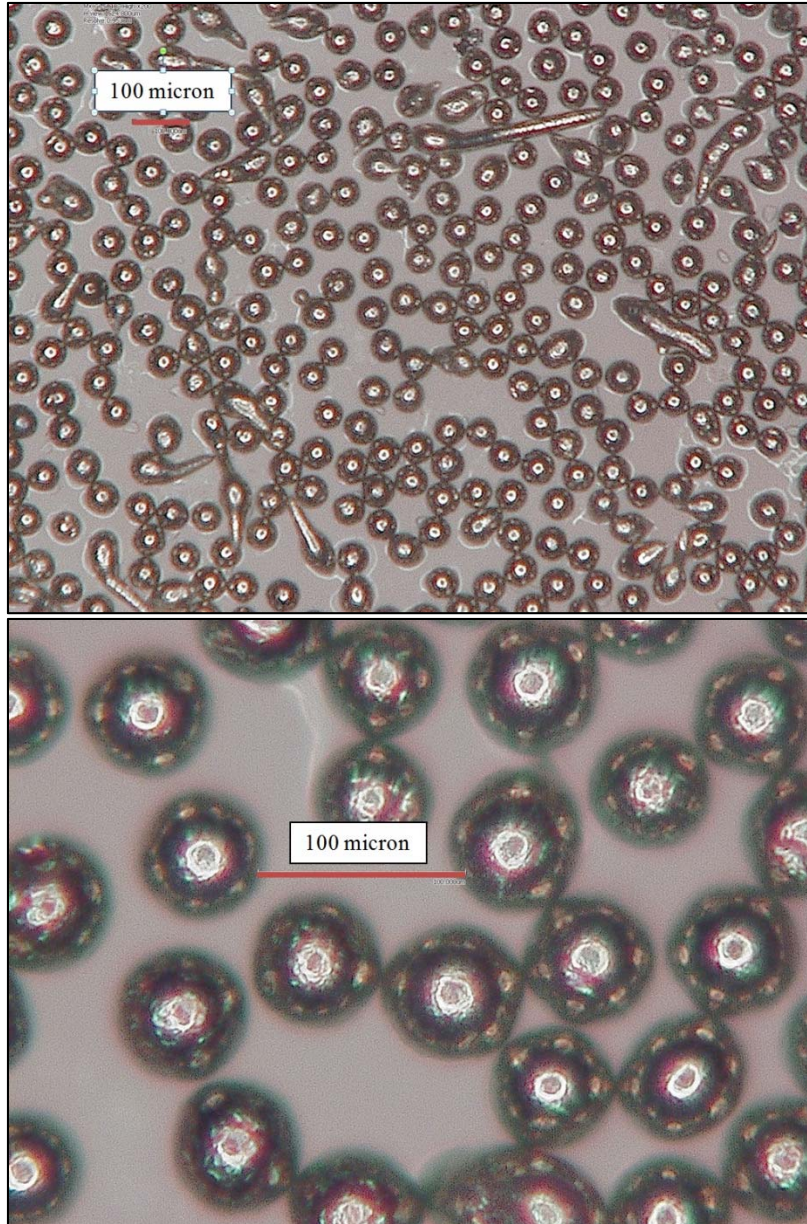
Figure 4-33: 16,000 RPM uranium powder seen at 200x (above) and 800x (below) magnification

Figure 4-34 shows uranium powder after it had oxidized in air. The oxidation reduced the amount of light reflected by the microspheres and allowed for better imaging without the light reflective artifacts in the previous images.
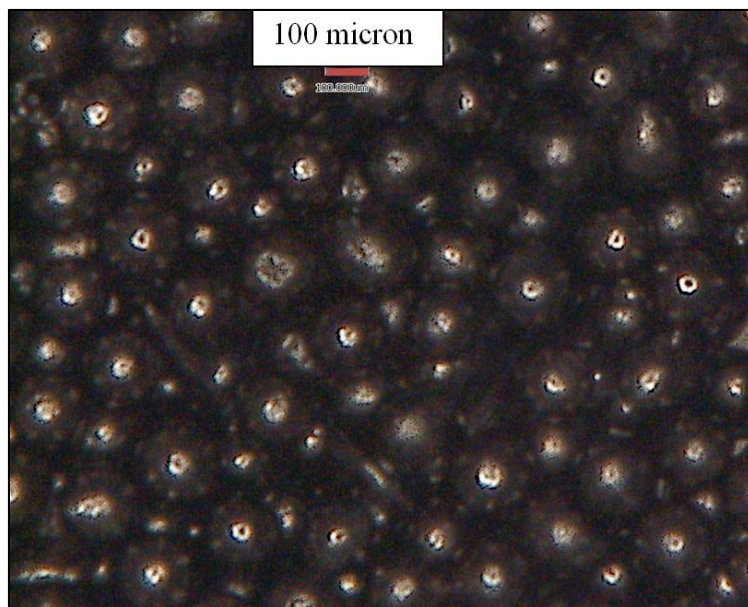
Figure 4-34: Oxidized uranium powder produced at 16,000 RPM and suspended in epoxy

4.3   Uranium 10 Weight Percent Zirconium Powder

Four production tests of the RES were conducted using 3/8 inch (0.9525 cm) diameter uranium, 10 weight percent zirconium (U-10Zr) alloy rods from Y-12 (Oak Ridge, TN, USA). The number of tests possible was limited by the amount of U-10Zr material. Surface oxidation was removed from the rods in the same manner described in section 4.2. However, it was easier to remove the oxidation from the U-10Zr rods than for the uranium rods. Interestingly, the U-10Zr rods stayed warm to the touch for a longer period of time after grinding the surface oxide away. The four tests were conducted at 14,000, 15,000, 16,000, and 18,000 RPM respectively. The 18,000 RPM test was conducted using 50 A of current, based on the amperage required to melt uranium rods. This proved to be enough to melt the rod but was not sufficient to produce fine powder, instead producing mostly large chips of material shown in Figure 4-35. The chips were a matte gray color and had smooth, rounded

edges. Although powder was produced from this experiment and characterized, the data was not included in the results shown in the following sections because it would not be representative. Figure 4-36 shows the melt tip of the 18,000 RPM U-10Zr rod after atomization. The rest of the tests using a U-10Zr rotating electrode were operated at currents between 100 and 125 A.

Figure 4-35: U-10Zr powder produced at 18,000 RPM using 50 A

Figure 4-36: The melt tip of the 18,000 RPM U-10Zr rod after atomization

4.3.1   Mass Percent Yield vs. Microsphere Diameter (U-10Zr Powder)

This section presents the results of U-10Zr powder characterization in terms of the size range of the powder versus the mass percentage yields of the total powder collected. Figure 4-37 depicts an overview of U-10Zr size distribution percentages as a function of rotational speed of the rotated electrode. The size distributions were notably different than those produced for either copper or uranium. In the graph, three peaks can be observed. The first is located within the 500 to 710 μm size range and is made up of large, non-spherical particles. The second peak is located within the 250 to 300 μm size range and is made up of spherical and non-spherical particles. The third peak appeared while operating at 15,000 RPM and is located within the 180 to 212 μm size range.

The first two peaks responded more like the uranium peaks did to an increase in rotational speed by receding slightly in height. The third peak imitated copper behavior and appeared to be a result of increased rotational speed and slightly broadening with further

increases in rotational speed. It is likely that the first peak is an artifact of the "shard" formation at large particle sizes and is not representative of microsphere powder formation distributions.
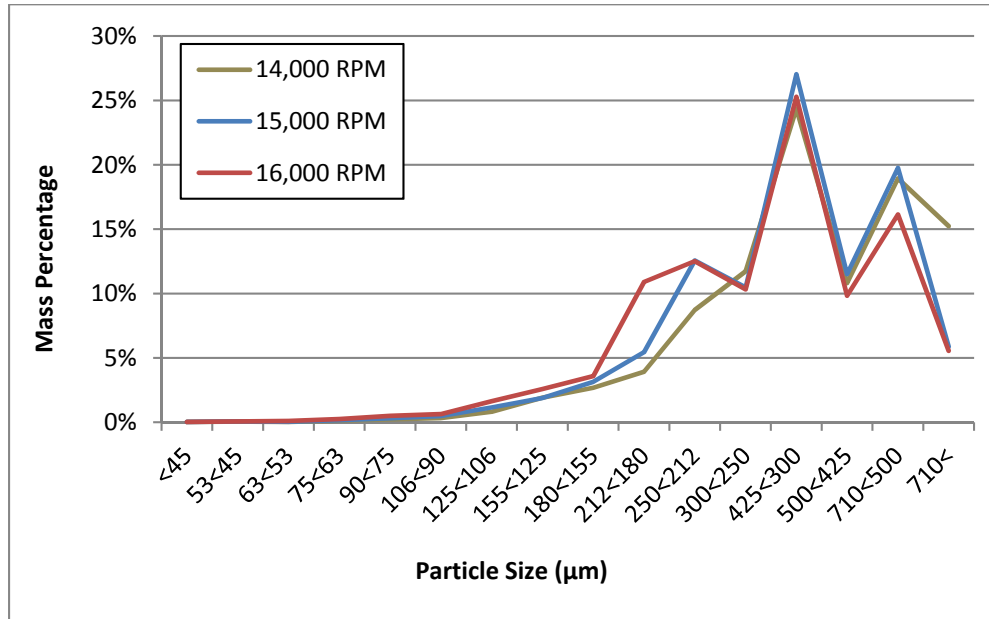
Figure 4-37: Overview of U-10Zr powder production percentage versus powder size at varying rotational speeds

Figure 4-38 shows the evolution of the U-10 Zr powder distribution as rotational speed of the rotating electrode was increased from 14,000 RPM to 16,000 RPM. Notable include the reduction of particles in the greater than 710 μm range and the increase of particles in the 300 to 425 μm and 212 to 250 μm ranges. A notable change between 15,000 RPM and 16,000 RPM was the increase of particles in the 180 to 212 μm range.
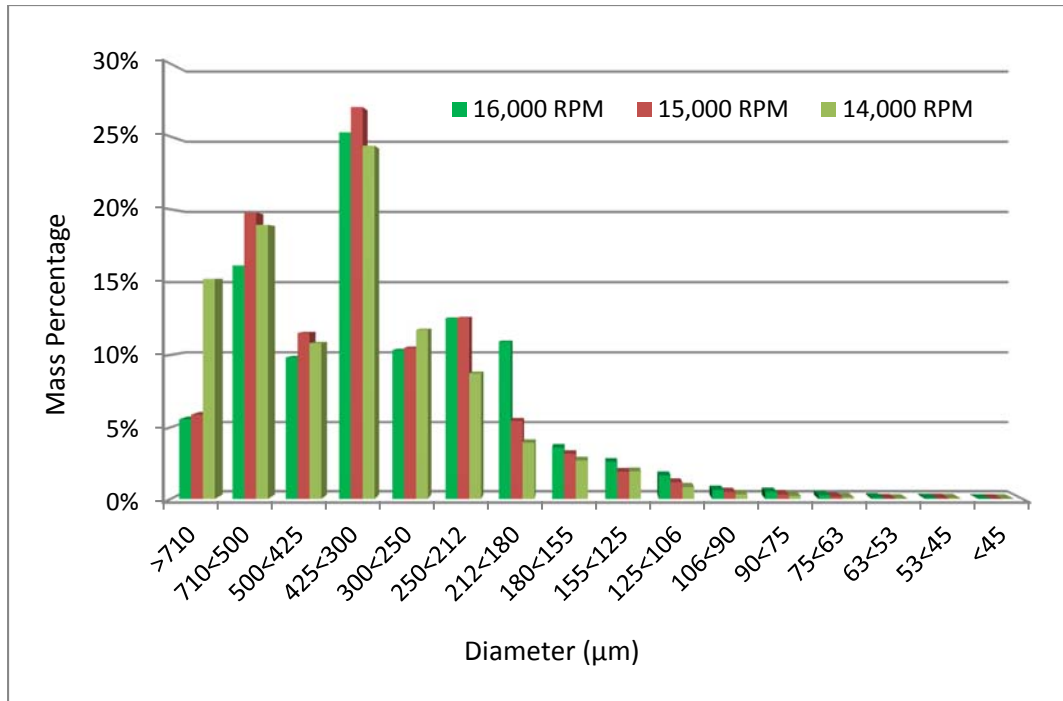
Figure 4-38: Overview of U-10Zr powder yield percentages versus powder size at 14,000, 15,000, and 16,000 RPM

4.3.2   Mass Percent Yield vs. Electrode Rotational Speed

This section presents the results of U-10Zr powder characterization in terms of the rotational speed of the rotating electrode versus the mass percent yields of the total collected powder. Figure 4-39 depicts the mass percentage of every size range as a function of RPM. Size ranges below 180 μm experience very slow growth compared to copper and DU. The only size range that experienced significant growth was 180 to 212 μm. In addition, larger size ranges did not decrease as rapidly as their uranium and copper counterparts, with the fastest decrease occurring in the greater than 710 μm size range. Figure 4-40 isolates and compares the middle size ranges, while Figure 4-41 does the same for the smallest size ranges.
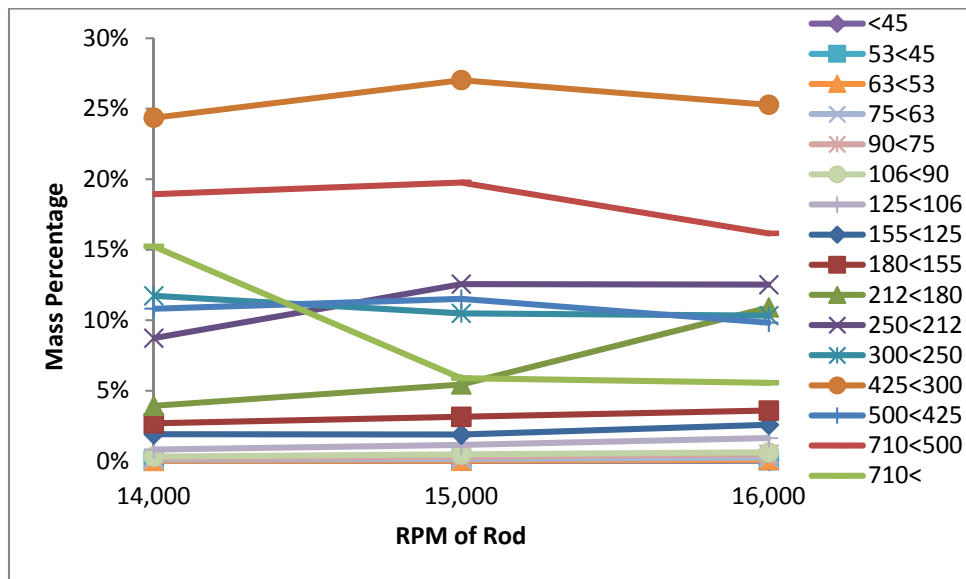
Figure 4-39: Overview of U-10Zr powder production percentages as a function of rotational speed
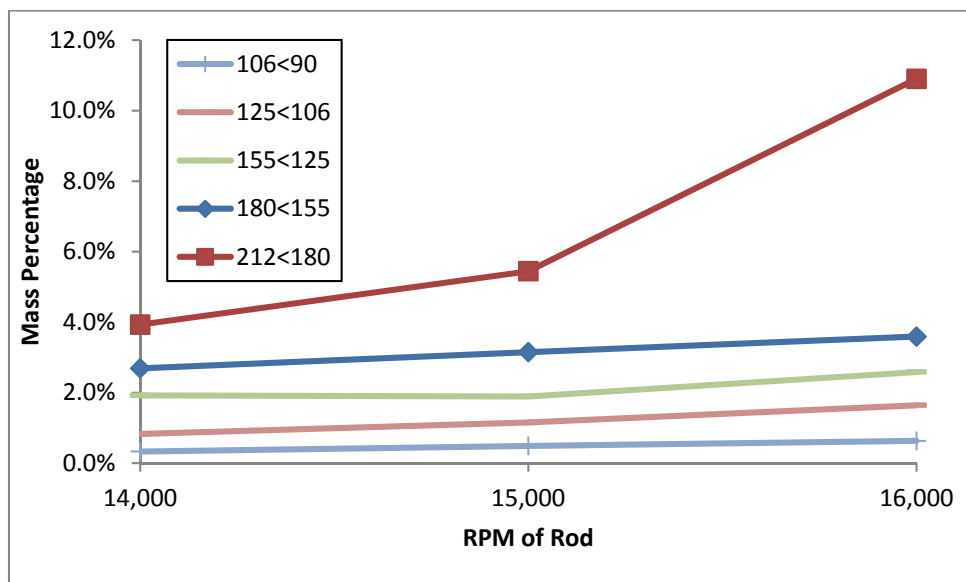
Figure 4-40: Medium size ranges of U-10Zr powders produced as function of rotational speed
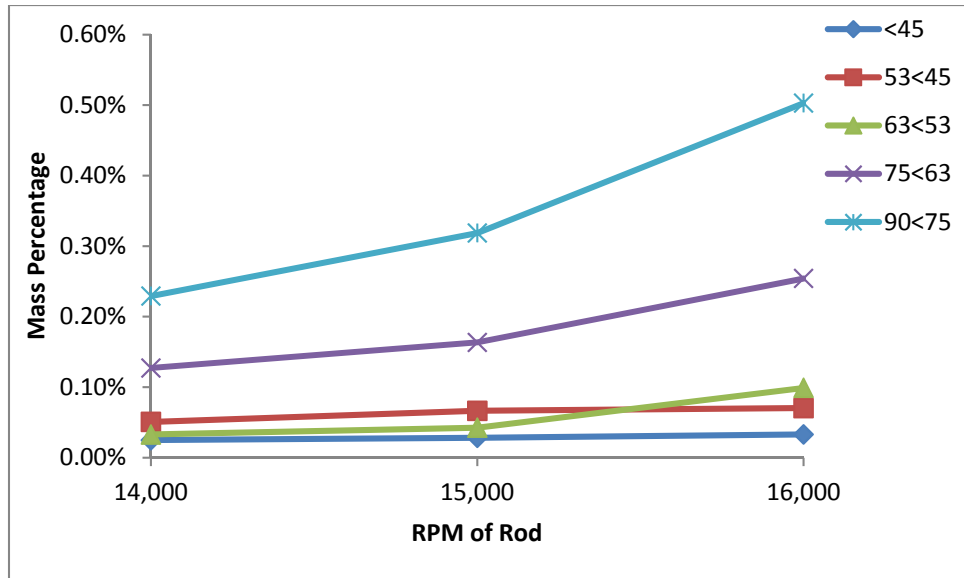
Figure 4-41: Small size ranges of U-10Zr powders produced as function of rotational speed

4.3.3   Imaging Of U-10Zr Microspheres

Despite U-10Zr's propensity to produce larger, rough particles, once filtered and characterized, the microspheres that were produced contained a smaller percentage of non-spherical particles than either copper or uranium. The non-spherical powder shown in Figure 4-42 was produced at 16,000 RPM using 125 A and is from the 180 to 212 μm size range. The non-spherical particles are mainly composed of "slugs" and slightly elongated spheres. Even less non-spherical powder was present in the 53 to 63 μm size range as evidenced in Figure 4-43.
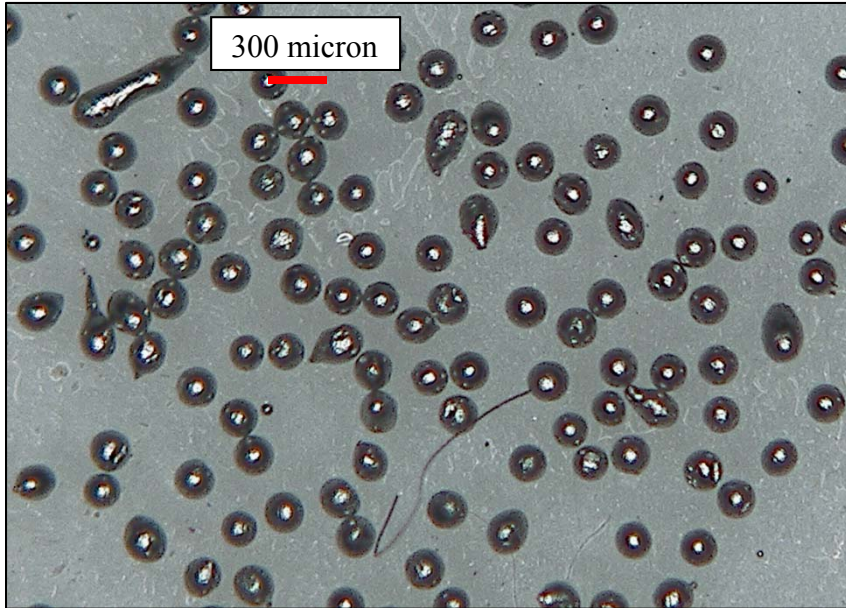
Figure 4-42: 180 to 212 μm U-10Zr powder produced at 16,000 RPM
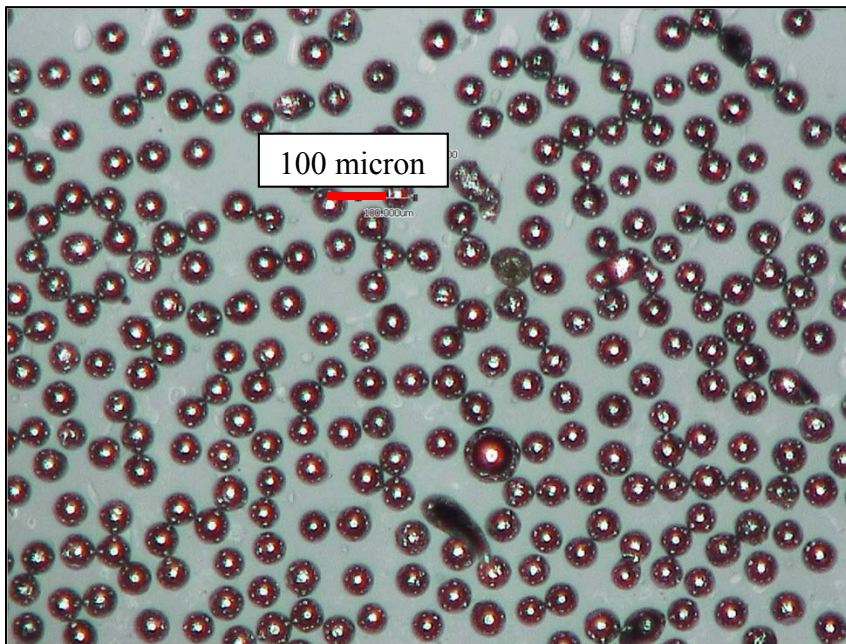
Figure 4-43: 53 to 63 μm U-10Zr powder produced at 16,000 RPM

U-10Zr powder from the 16,000 RPM test exhibited more surface roughness than either copper or uranium as shown in Figure 4-44.
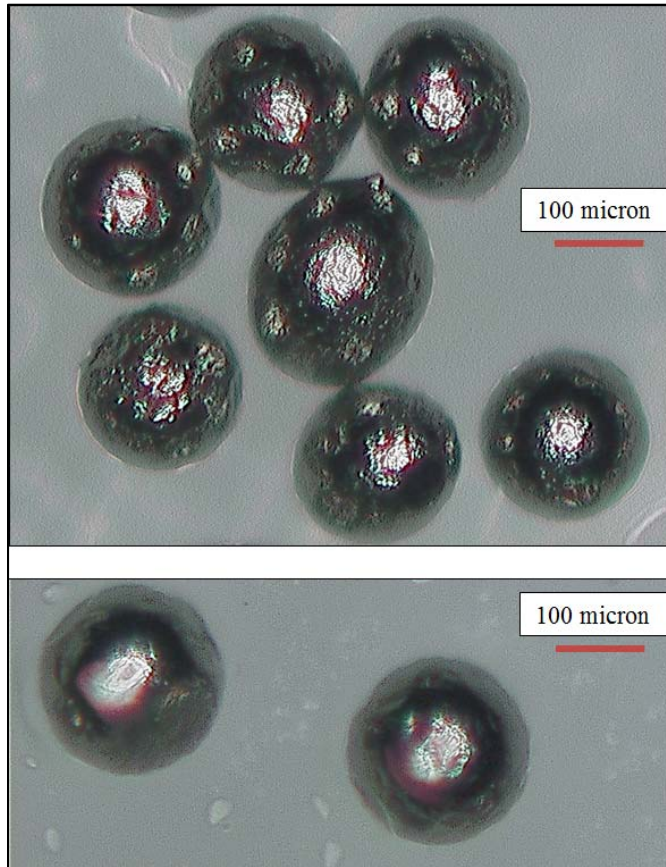
Figure 4-44: 180 to 212 μm U-10Zr powder produced at 16,000 RPM

5. DISCUSSION

Powder produced with the RES displayed the same size distribution trend discovered by Miller et al and Starmet Corporation [22]. As the rotational speed of the melting electrode increases, the average size of the particles produced at that speed decreased. For speeds greater than 12,000 RPM, powder size distributions exhibited a bi-modal characteristic where the majority of powder by mass percentage was produced within two distinct size ranges. This behavior is explained by Neikov et al [23] to be the result of larger spheres forming from and consuming the ligaments of molten metal thrown radially from the pin by centrifugal force, while smaller satellite spheres are formed from leftover ligament material.

The size difference between the primary and secondary spheres produced by ligament disintegration process is dependent on the balance between centrifugal and surface tension forces acting on the molten material. Higher rotational speeds impart more centrifugal force to the molten film at the periphery of the rod and overcome the surface tension forces holding the molten material to itself. This causes the spheres that break away from the ligaments to become more uniform as rotational speed is increased, because less material can be held together by surface tension. Non-uniform spheres can be formed even at high rotational speeds if the melt rate is also high. A high melt rate causes a film of material to form at the rod's periphery and inhibits ligaments from forming and breaking uniformly. U-10Zr powder displayed an additional third peak at large particle sizes (greater than 450 μm). Previous work implies that increasing the angular velocity of the rotating electrode would alleviate this effect.

Copper and uranium powder retained bi-modal size distributions at every rotational speed tested above 12,000 RPM. Higher rotational speeds produced distributions shifted towards

smaller average particle sizes and larger yields in the smaller particle size ranges. Copper displayed a higher tendency to form non-spherical particles than uranium, although the tendency is alleviated by rotating at higher speeds. Molten copper's lower surface tension value of 1.23 N/m [13, 14] (compared to 1.55 N/m for molten uranium [15]) may be a contributing factor to its difficulty in forming spheres before hardening. The uranium and U-10Zr powders relative lack of non-spherical particles is attributed to (assumed) higher surface tension values. Oblong uranium spheres were observed at larger sizes (180 to 250 μm) when rotating at a low speed of 13,000 RPM, while more worm-like particles were discovered in the same size range of powder that had been rotated at 16,000 RPM. The use of helium coolant may have influenced the hardening of melt ligaments at this higher speed to produce the worm-like particles.

It is apparent that the U-10Zr powder yield distributions did not respond to increased rotational speeds to the same degree as their uranium and copper counterparts. A stronger current was required to melt the U-10Zr rods, reflecting the higher melting point and lower electrical resistivity of U-10Zr. The U-10Zr rods also stayed warm to the touch longer than uranium or copper after sanding, confirming its lower thermal conductivity value.

Neither the uranium nor the U-10Zr powder samples showed signs of porosity when polished and viewed under a microscope. The digital Hirox microscope was only capable of resolving features greater than approximately 10 to 20 μm in size. Porosity that may exist below this size range would not be detectable. However, only large bubble pores (greater than100 μm) have been reported to form during the rotating electrode process [21]. It is therefore not likely that either the uranium or U-10Zr powders contain any porosity.

It was observed that uranium and U-10Zr microspheres had rougher surfaces than the copper microspheres. U-10Zr especially exhibited ridges and swirls along the entire surface of the microsphere, with uranium exhibited similar but subdued features. These features could be seen with the microscope but were blurry and could not be further resolved.

6. SUMMARY

6.1   Rotating Electrode Performance

The RES performs well at its new location inside of an argon atmosphere glovebox. The maximum rotational speed demonstrated was 18,000 RPM (1,885 rad/s) with uranium, 19,000 RPM (1,990 rad/s) with copper, and 16,000 RPM (1675 rad/s) with U-10Zr. This speed can be greatly increased to as much as 40,000 RPM if a balanced slip ring is installed and balanced electrodes are selected for atomization. Molten droplets produced during the rotating electrode process are propelled radially away from the electrode and are cooled via forced helium circulation and ambient heat transfer to their argon environment. The electrical and water cooling systems for the RES functioned well, with no leaks either into or out of the glovebox.

The length of each rod of material that can be melted during a single test of the RES is limited the rotational stresses induced on the rod by mechanical imbalances during rotation. Currently, at high RPMs (>15,000) the maximum allowable length of material that can be safely atomized during a single test is about one inch (2.54 cm). This number is dependent on the mechanical stability of the material being rotated. It may be possible to allow more length of a strong, very straight material to extend from the collet during operation.

6.2   Powder Characterization

The TAMU RES was used to create copper, depleted uranium, and U-10 wt% Zr spherical powders. These powders were produced by rotating cylindrical rods of material at high speeds while simultaneously melting them in an argon environment via electric arc. The powders were filtered into discrete size ranges and their size distributions were characterized

by their weight percentage of the total powder produced during a specific production test. Copper was used to demonstrate the system for functionality, while uranium and U-10Zr rods were melted for research purposes. It was found that uranium and U-10Zr both produce very spherical, non-porous powders at all rotational speeds tested, from relatively low (10,000) to high (18,000) RPMs. The non-spherical uranium and U-10Zr particles that were produced either occurred at very large particle sizes (greater than 450 μm) or were consistent in their shape. It is thought that either instance of non-sphericity can be alleviated by melting at higher rotational speeds.

A bi-modal size distribution was observed in all powder sets to occur at rotational speeds above ~12,000 RPM. This distribution feature can be attributed to the direct drop formation (DDF) mode of molten droplet formation described by Champagne et al [24], whereby surface tension forces are greater than centrifugal forces and a primary droplet with a tail is ejected from the periphery of the rotating rod. Surface tension forms the primary droplet into sphere while the tail forms smaller satellite spheres. The bi-modal distribution is predicted to persist at higher RPMs; however, the mass percentage value of the peaks will begin to approach one another.

The RES is a feasible and economical approach to producing highly spherical, non-porous metal powder which can then be used to manufacture materials with highly known smear densities. It can produce alloy metal microspheres by melting a pre-alloyed bar, and the size distributions of copper, depleted uranium, and U-10Zr powder have been characterized for rotational speeds between 10,000 and 18,000 RPM. Future areas of endeavor may include melting larger diameter rods to increase centrifugal force without increasing speed, more fully characterizing U-10Zr powder for density, element segregation,

and rotational speeds, and melting two non-alloyed materials at once to create alloyed microspheres.

REFERENCES

[1] C. Thompson and S. M. McDeavitt, *A Rotating Electrode System for the Generation of Metal Alloy Microspheres,* College Station, TX: Texas A&M University, 2012.

[2] N. Touran, P. Hejzlar and e. al., "Technical Considerations and Capabilities of a Near-Term Deployable Traveling Wave Reactor Core," TerraPower LLC, Bellevue, WA, 2012.

[3] G. L. Hofman and L. C. Walters, "Metallic Fast Reactor Fuels," in *Materials Science and Technology, Vol10A, Nuclear Materials*, VCH Publishers, 1994.

[4] L. C. Walters, B. R. Seidel and J. H. Kittel, "Performance of Metallic Fuels and Blankets in Liquid-Metal Fast Breeder Reactors," *Nuclear Technology,* vol. 65, no. 2, pp. 179-231, May 1984.

[5] N. Touran, P. Hejzlar, S. Mazurkiewicz, R. Petroski, J. Walter and C. Whitmer, "Technical Considerations and Capabilities of a Near-Term Deployable Traveling Wave Reactor Croe," TerraPower LLC, Bellvue, WA.

[6] L. Koch, *Experimental Breeder Reactor-II,* La Grange Park, IL: American Nuclear Society, 1987.

[7] R. J. Anicetti, R. C. Smith and W. J. Bailey, "Ceramic Fuels for Heavy Water Reactors," Battelle Memorial Insitutute, Richland, WA, 1970.

[8] R. G. Pahl, D. L. Porter, D. C. Crawford and L. C. Walters, "Irradiation Behavior of Metallic Fast Reactor Fuels," *Journal of Nuclear Materials,* vol. 188, pp. 3-9, 1992.

[9] D. R. Olander, Fundamental Aspects of Nuclear Reactor Fuel Elements: Solutions to Problems, Springfield, VA: Oak Ridge Tennessee: Energy Research and Development Administratio. Technical Information Center, 1976.

[10] C. J. Humrickhouse-Helmreich, "Measurement of thermal diffusivity of depleted uranium metal microspheres," *Journal of Nuclear Materials,* vol. 446, no. 1-3, pp. 100-105, 2014.

[11] C. J. Humrickhouse, *Characterization of Thermal Properties of Depleted Uranium Metal Microspheres,* College Station: Texas A&M University, 2012.

[12] C. R. Clark, J. F. Jue and B. R. Muntifering, "Production and Characterization of Atomized U-Mo Powder by the Rotating Electrode Process," in *INL?CON-07-13156,* Idaho Falls, 2007.

[13] J. A. Cahill and A. D. Kirshenbaum, "The Density of Liquid Copper from Its Melting Point (1356 K) to 2500 K and an Estimate of Its Critical Constants," *J. Phys. Chem.,* vol. 66, no. 6, pp. 1080-1082, 1962.

[14] D. A. Harrison, S. Blairs and D. Yan, "The Surface Tension of Liquid Copper," *J. Chem. Thermodynamics,* vol. 9, pp. 1111-1119, 1977.

[15] J. A. Cahill and A. D. Kirshenbaum, "The Surface Tension of Liquid Uranium," *J. Inorg. Nucl, Chem.,,* vol. 27, pp. 73-76, 1965.

[16] W. G. Rohr and L. J. Wittenberg, "Density of Liquid Uranium," *J. Phys. Chem,* vol. 74, no. 5, pp. 1151-1152, 1970.

[17] G. L. Hofman, "A Short Note on High Density Dispersion Fuel," Argonne National Laboratory, Argonne, IL, 1996.

[18] C. W. Tucker, "The Crystal Structure of the Beta Phase of Uranium," *Acta Cryst.,* vol. 4, pp. 425-431, 1951.

[19] S. M. McDeavitt and A. A. Solomon, "Hot-isostatic Pressing of U-10Zr by a Coupled Grain Boundary Diffusion and Creep Cavity Mechanism," *Journal of Nuclear Materials,* vol. 228, no. 2, pp. 184-200, 1996.

[20] R. I. Sheldon and D. E. Peterson, "The U-Zr (Uranium-Zirconium) System," *Bulletin of Alloy Phase Diagrams,* vol. 10, pp. 165-171, 1989.

[21] R. German, Powder Metallurgy Science, 2 ed., Princeton, NJ: Metal Powder Industries Federation, 1994.

[22] S. A. Miller and P. R. Roberts, "ASM Handbook, Volume 7: Powder Metal Technologies and Applications," in *Rotating Electrode Proccess*, ASM International, 1998, pp. 97-101.

[23] O. D. Neikov, S. Naboychenko, V. G. Gopienko, I. B. Mourachova, I. V. Frishberg and D. V. Lotsko, Handbook of Non-Ferrous Metal Powders: Technologies and Applications, Elsevier, 2009.

[24] B. Champagne and R. Angers, "Fabrication of Powders by the Rotating Electrode Process," *The International Journal of Powder Metallurgy & Powder Technology,* vol. 16, no. 4, pp. 359-361, 363, 1980.

[25] G. Taylor, "The Instability of Liquid Surfaces When Accelerated In a Direction Perpendicular to Their Planes. I.," *Proceedings of the Royal Society of London. Series A, Mathematical and Physical Sciences,* vol. 201, pp. 192-196, 1950.

[26] B. Champagne and R. Angers, "Size Distributions of Powders Atomized by the Rotating Electrode Process," *Modern Dveelopments in Powder Metallurgy,* vol. 12, pp. 83-104, 1981.

[27] A. R. Kaufman, "Method and Apparatus for Making Powder". U.S. Patent 3099014.

[28] A. R. Kaufman, "Production of Pure, Spherical Powders". U.S. Patent 3802816.

[29] H. J. DeMita and S. A. Miller, "System and Method for Producing Fine Metallic and Ceramic Powders". United States of America Patent 5855642, 1999.

[30] Lincoln Electric, *Precision TIG 225 Operators Manual,* IM895, 2007.

[31] Zena Inc., "ZENA Incorporated," 2002. [Online]. Available: http://www.zena.net/htdocs/FAQ/dutycycle.shtml. [Accessed 15 May 2014].

[32] Lincoln Electric, "Precision TIG Welders," 2014. [Online]. Available: http://www.lincolnelectric.com/en-us/equipment/tig-welders/pages/precision-tig.aspx. [Accessed 15 May 2014].

[33] Mersen U.S.A., "Brushes for Electrical Machines Technical Guide," [Online]. Available: http://www.mersen.com/uploads/tx_mersen/514_3-brushes-for-electrical-machines-en.pdf. [Accessed 16 May 2014].

[34] F. P. Incropera, D. P. Dewitt, T. L. Berman and A. S. Lavine, Fundamentals of Heat and Mass Transfer, John Wiley & Sons, Inc, 2007.

[35] M. S. Bohn, F. Kreith and R. M. Manglik, Principles of Heat Transfer, 7 ed., Pacific Grove, CA: Brooks/Cole, 2010.

[36] MTI Corporation, "MTI Corporation," 2010. [Online]. Available: http://www.mtixtl.com/MSDS/Conductive%20Graphite%20Powder.pdf. [Accessed 19 May 2014].

[37] Thermo Scientific NESLAB ThermoFlex, Installation Operation Basic Maintenance, Newington, New Hampshire: Thermo Fisher Scientific, 2010, pp. 3-10.

[38] Conax Technologies, "Sealing Glands Introduction," conax technologies, 2014. [Online]. Available: http://www.conaxtechnologies.com/sg_intro.shtml. [Accessed 22 May 2014].

[39] Conax Technologies, "EGT Series Single Electrode Sealing (to 8000 Volts)," [Online]. Available: http://www.conaxtechnologies.com/products/pdf/catalogs_us/Conax_Product_Literature_EGT_Glands_32-35_5001C.pdf. [Accessed 22 May 2014].

[40] Conax Technologies, "EG Series Single Electrode Sealing (to 2000 Volts)," [Online].
Available:
http://www.conaxtechnologies.com/products/pdf/catalogs_us/Conax_Product_Literatur
e_EG_Glands_28-31_5001C.pdf. [Accessed 22 May 2014].

[41] Conax Technologies, "PL Series Insulated Leadwire (Power Lead) Sealing," [Online].
Available:
http://www.conaxtechnologies.com/products/pdf/catalogs_us/Conax_Product_Literatur
e_PL_Glands_40-45_5001C.pdf. [Accessed 22 May 2014].

[42] "Dynamicaqua," [Online]. Available: http://www.dynamicaqua.com/soil.html#sieve.
[Accessed 28 July 2014].

[43] Scintag, Inc., "UNM Department of Earth & Planetary Sciences," [Online]. Available:
http://epswww.unm.edu/xrd/xrdbasics.pdf. [Accessed 30 May 2014].

[44] Texas A&M University Geology & Geophysics Department, "X-Ray Diffraction Lab at
Texas A&M University Geology & Geophysics Department," [Online]. Available:
http://geoweb.tamu.edu/RResearch/XRayDiff.html. [Accessed 30 May 2014].

[45] J. M. Wentzell, "Particle Size Prediction from the Spinning Disk Atomizer," *Powder
Mer. Int.,* vol. 18, no. 1, p. 16, 1986.
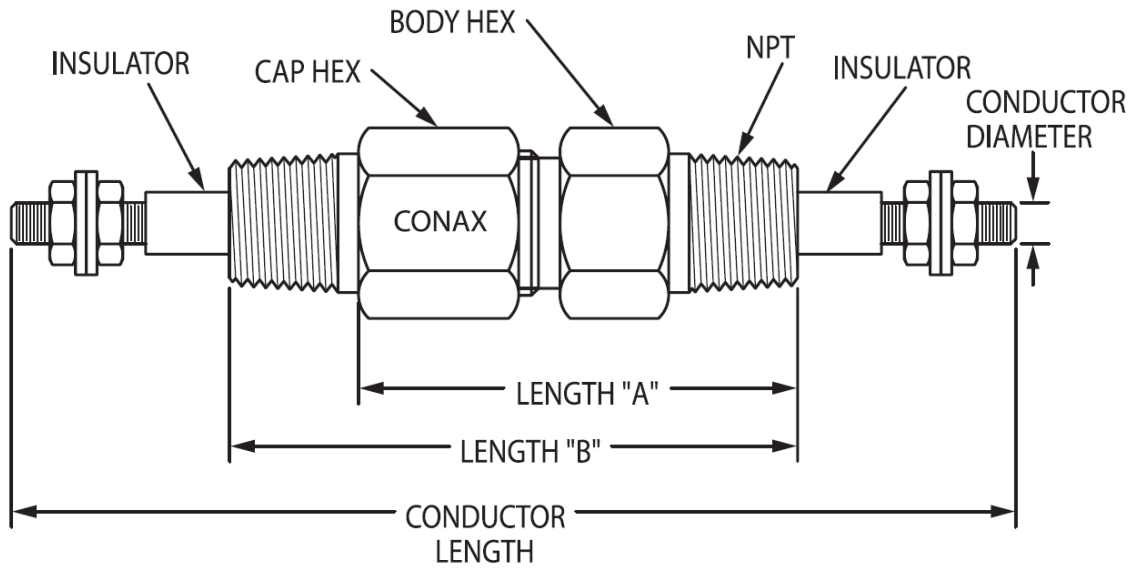
APPENDIX A

Schematics

128

Labels: INSULATOR, CAP HEX, BODY HEX, NPT, INSULATOR, CONDUCTOR DIAMETER, CONAX, LENGTH "A", LENGTH "B", CONDUCTOR LENGTH

Catalog Number	Conductor				Amperage Rating (@ 30°C, 90°C max)			Voltage Rating DC	Length 'A'		Length 'B'		Hex Size				Pressure Rating Teflon	
	Diam. IN	Std. Length IN	Diam. MM	Std. Length MM	CU	NI	SS	DC	IN	MM	IN	MM	Body IN	Cap IN	Body MM	Cap MM	PSIG	BAR
Standard 1 NPT																		
EGT-750	0.745	9.250	18.92	234.95	400	165	60	8000	3.50	88.9	4.50	114.3	1.750	2.000	44.5	50.8	600	41

Catalog Number	Conductor				Amperage Rating (@ 30°C, 90°C max)			Voltage Rating DC	Length 'A'		Length 'B'		Hex Size				Pressure Rating							
	Diam. IN	Std. Length IN	Diam. MM	Std. Length MM	CU	NI	SS	DC	IN	MM	IN	MM	Body IN	Cap IN	Body MM	Cap MM	Neoprene PSIG	BAR	Viton PSIG	BAR	Teflon PSIG	BAR	Lava PSIG	BAR
Standard 3/4 NPT																								
EG-375	0.370	8.500	9.40	215.90	160	65	24	2000	3.31	84.1	4.06	103.1	1.250	1.500	31.8	38.1	600	41	800	55	2500	172	4000	276
EG-500	0.495	8.500	12.57	215.90	200	80	30	2000	3.31	84.1	4.06	103.1	1.250	1.500	31.8	38.1	600	41	600	41	1600	110	1500	103

BODY HEX

CAP HEX

NPT THREAD MOUNT

CONAX

LENGTH "A"
(STANDARD A CAP)

LENGTH "B"
(OPTIONAL B CAP)
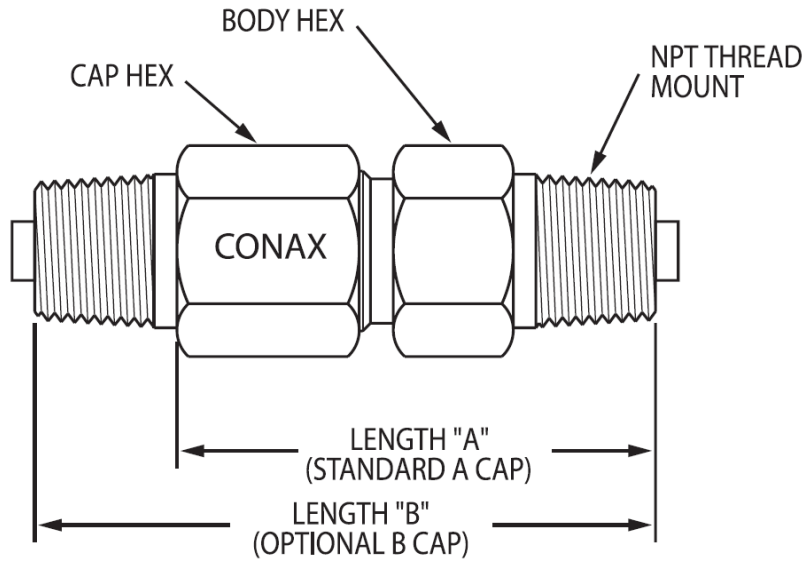
Catalog Number	Wire Gauge	Number of Wires	Rating Per Wire	Length 'A' IN	MM	Length 'B' IN	MM	Body IN	Cap IN	Body MM	Cap MM	Grafoil PSIG	BAR	Teflon PSIG	BAR
Standard 3/4 NPT															
PL-20-6	20	6	9	2.88	73.0	3.63	92.1	1.125	1.250	28.6	31.8	10,000	689	3,200	220
PL-20-8	20	8	9	2.88	73.0	3.63	92.1	1.125	1.250	28.6	31.8	10,000	689	3,200	220
PL-20-18	20	18	9	2.88	73.0	3.63	92.1	1.250	1.500	31.8	38.1	10,000	689	2,400	165
PL-18-6	18	6	13	2.88	73.0	3.63	92.1	1.125	1.250	28.6	31.8	10,000	689	2,700	186
PL-18-8	18	8	13	2.88	73.0	3.63	92.1	1.125	1.250	28.6	31.8	10,000	689	2,700	186
PL-18-10	18	10	13	2.88	73.0	3.63	92.1	1.250	1.500	31.8	38.1	10,000	689	2,100	145
PL-18-12	18	12	13	2.88	73.0	3.63	92.1	1.250	1.500	31.8	38.1	10,000	689	2,100	145
PL-16-6	16	6	17	2.88	73.0	3.63	92.1	1.125	1.250	28.6	31.8	10,000	689	2,700	186
PL-16-8	16	8	17	2.88	73.0	3.63	92.1	1.125	1.250	28.6	31.8	10,000	689	2,700	186
PL-16-10	16	10	17	2.88	73.0	3.63	92.1	1.250	1.500	31.8	38.1	10,000	689	1,700	117
PL-16-12	16	12	17	2.88	73.0	3.63	92.1	1.250	1.500	31.8	38.1	10,000	689	1,700	117
PL-14-6	14	6	24	2.88	73.0	3.63	92.1	1.125	1.250	28.6	31.8	10,000	689	1,600	110
PL-14-8	14	8	24	2.88	73.0	3.63	92.1	1.125	1.250	28.6	31.8	10,000	689	1,600	110
PL-14-10	14	10	24	2.88	73.0	3.63	92.1	1.250	1.500	31.8	38.1	10,000	689	1,400	96
PL-14-12	14	12	24	2.88	73.0	3.63	92.1	1.250	1.500	31.8	38.1	10,000	689	1,400	96
PL-12-2	12	2	30	2.88	73.0	3.63	92.1	1.125	1.250	28.6	31.8	8,800	606	1,200	83
PL-12-3	12	3	30	2.88	73.0	3.63	92.1	1.125	1.250	28.6	31.8	8,800	606	1,200	83
PL-12-4	12	4	30	2.88	73.0	3.63	92.1	1.125	1.250	28.6	31.8	8,800	606	1,200	83
PL-12-6	12	6	30	2.88	73.0	3.63	92.1	1.125	1.250	28.6	31.8	8,800	606	1,200	83

Sketches

Welder-to-EGT Adapter

40.41673°

0.337"

⌀=6.25"

2.275"

2.67"

0.2"

2"

3/8"

134
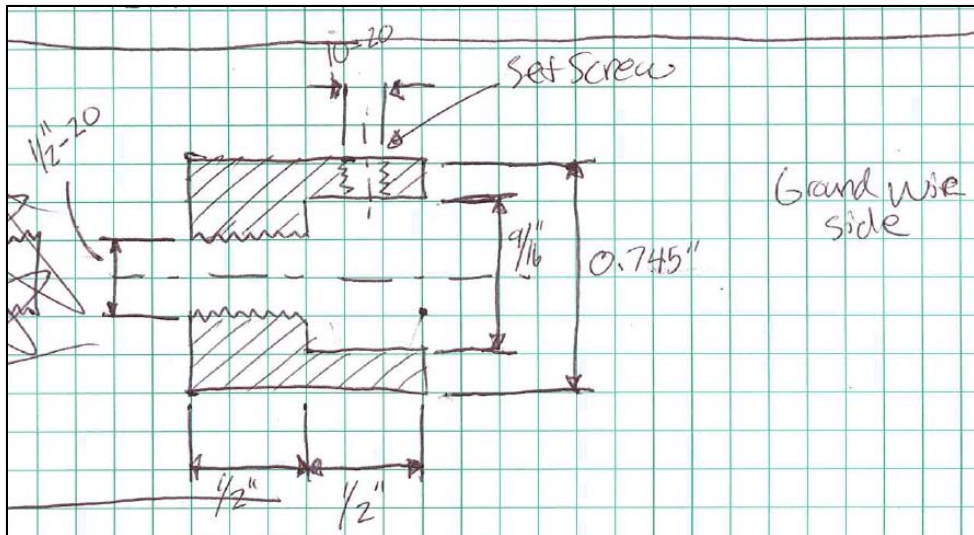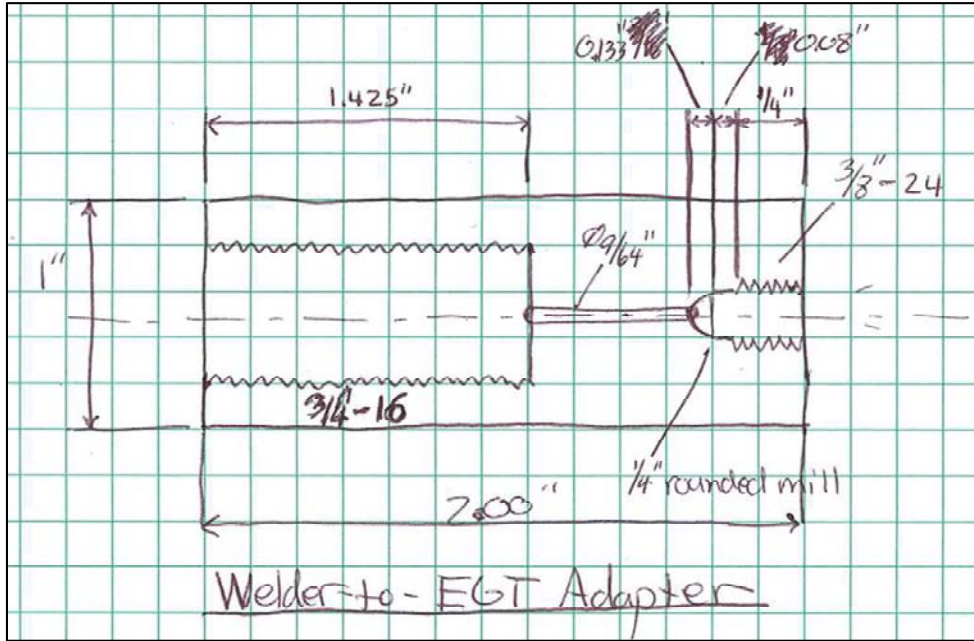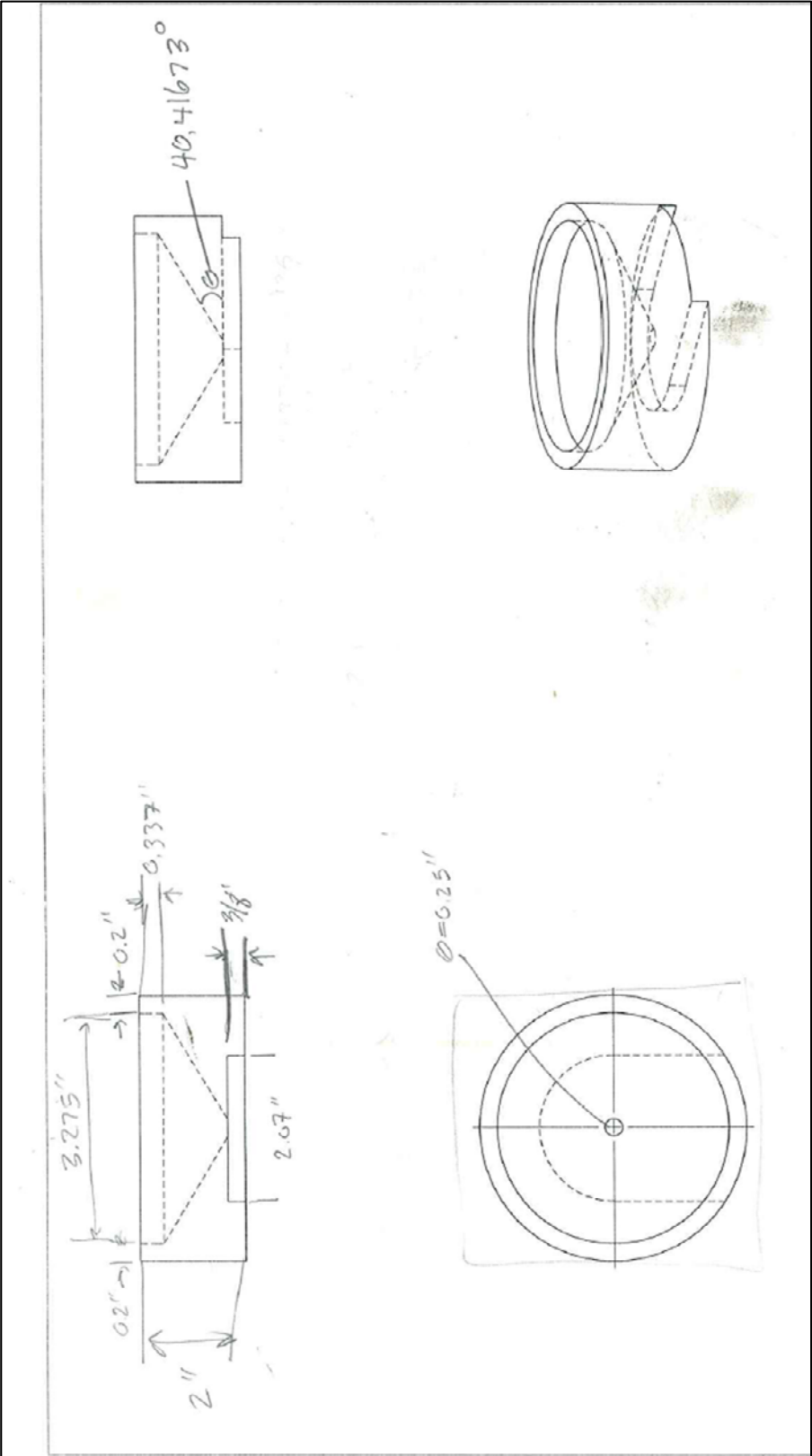
APPENDIX C

Rotating Electrode Material	Date	RPM	Pin Length (in)
Copper 1	05-Oct-12	12,014	5.067
2	05-Oct-12	17,963	5.056
3	18-Oct-12	17,963	-
4	16-Nov-12	9,973	5.085
5	16-Nov-12	11,023	5.048
6	26-Nov-12	13,006	5.305
7	27-Nov-12	13,997	5.146
8	28-Nov-12	15,047	5.042
9	29-Nov-12	16,038	5.125
10	08-Dec-12	10,031	5.069
11	08-Dec-12	12,014	5.038
12	09-Dec-12	17,030	4.987
13	09-Dec-12	18,021	5.033
14	17-Dec-12	19,013	unknown
15	19-Dec-12	20,004	4.988
16	03-May-13	13,006	6.165
17	24-Jun-13	14,988	4.975
18	16-Jul-13	14,988	4.949
19	19-Jul-13	14,988	4.932
20	30-Jul-13	14,988	5.003
DU 1	25-Sep-13	12,014	3.972
2	08-Aug-13	14,988	4.983
3	12-Aug-13	14,988	4.597
4	15-Aug-13	14,988	4.951
5	23-Oct-13	13,997	3.512
6	04-Nov-13	13,006	3.153
7	04-Nov-13	15,980	2.491
U-10Zr 1	05-Dec-13	18,021	3.701
2	09-Jan-14	15,980	2.777
3	21-Jan-14	15,046	3.464
4	24-Jan-14	13,997	2.460

| Rotating Electrode Material	Pin Weight (g)	Pin Length Post-Melt (in)	Pin Weight Post-Melt (g)
Copper 1	-	3.602	57.9190
2	-	3.580	56.9258
3		Broken	Broken
4	82.0148	3.627	57.8212
5	81.4721	3.349	53.0739
6	85.6715	5.345	76.7358
7	82.9488	3.306	52.7615
8	81.3505	3.196	51.4283
9	82.6328	3.325	53.0760
10	81.8648	3.500	54.8391
11	81.2866	3.495	55.7070
12	80.5049	3.485	55.1529
13	81.1637	3.424	54.4328
14	unknown	3.366	54.1652
15	80.3886	Broken	Broken
16	96.1862	4.115	66.1708
17	80.2734	3.363	53.7956
18	79.8906	3.335	47.2295
19	79.5768	3.274	52.7270
20	80.6830	3.442	55.3526
DU 1	145.7484	3.264	136.5471
2	199.5956	4.597	183.2747
3	183.2658	3.146	124.7393
4	203.3743	3.512	144.3433
5	144.2411	2.035	82.9894
6	124.6464	2.491	97.6765
7	97.6139	1.815	70.7562
U-10Zr 1	118.1786	2.774	87.5892
2	87.5884	1.830	56.7314
3	112.8432	2.460	80.0076
4	79.9635	1.456	46.8796

Rotating Electrode Material	Powder Produced (g)	Powder Retrieved (g)	Powder Lost During Collection (g)	Powder Weight After Filtering (g)
Copper 1	-	19.3663	-	-
2	-	25.5467	-	23.6512
3	-	-	-	-
4	24.1936	22.6318	1.5618	(unreliable data)
5	28.3982	28.3858	0.0124	27.9953
6	8.9357	8.8456	0.0901	8.7529
7	30.1873	29.9468	0.2405	29.6561
8	29.9222	29.6236	0.2986	29.4348
9	29.5568	29.4600	0.0968	28.8240
10	27.0257	26.8957	0.1300	26.4167
11	25.5796	25.4416	0.1380	25.1433
12	21.0416	20.8655	0.1761	20.4651
13	26.7309	26.6664	0.0645	26.1576
14	unknown	27.3981	unknown	27.2087
15	-	-	-	-
16	30.0154	29.7520	0.2634	29.5749
17	26.4778	25.3767	1.1011	25.3558
18	32.6611	32.8865	-0.2254	32.8439
19	26.8498	24.3487	2.5011	24.2742
20	25.3304	25.2906	0.0398	unknown
DU 1	9.2013	7.8354	1.3659	7.6508
2	16.3209	15.9822	0.3387	15.8954
3	58.5265	57.8726	0.6539	57.7867
4	59.0310	58.5138	0.5172	58.4816
5	61.2517	60.5472	0.7045	60.4672
6	26.9699	26.8527	0.1172	26.6250
7	26.8677	24.8107	2.0570	24.7026
U-10Zr 1	30.5894	29.8358	0.7536	29.6573
2	30.8570	30.4492	0.4078	30.2851
3	32.8356	32.2892	0.5464	32.2285
4	33.0839	32.5890	0.4949	32.5333

Rotating Electrode Material	Powder Lost During Filtering (g)	Total Powder Lost (g)	Total Powder Lost (%)
Copper 1	-	-	-
2	1.8955	-	-
3	-	-	-
4	(unreliable data)	(unreliable data)	(unreliable data)
5	0.3905	0.4029	1.419%
6	0.0927	0.1828	2.046%
7	0.2907	0.5312	1.760%
8	0.1888	0.4874	1.629%
9	0.6360	0.7328	2.479%
10	0.4790	0.6090	2.253%
11	0.2983	0.4363	1.706%
12	0.4004	0.5765	2.740%
13	0.5088	0.5733	2.145%
14	0.1894	unknown	unknown
15	-	-	-
16	0.1771	0.4405	1.468%
17	0.0209	1.1220	4.238%
18	0.0426	-0.1828	-0.560%
19	0.0745	2.5756	9.593%
20	-	-	-
DU 1	0.1846	1.5505	16.851%
2	0.0868	0.4255	2.607%
3	0.0859	0.7398	1.264%
4	0.0322	0.5494	0.931%
5	0.0800	0.7845	1.281%
6	0.2277	0.3449	1.279%
7	0.1081	2.1651	8.058%
U-10Zr 1	0.1785	0.9321	3.047%
2	0.1641	0.5719	1.853%
3	0.0607	0.6071	1.849%
4	0.0557	0.5506	1.664%

APPENDIX D

The first test of the RES using a uranium rotating electrode was conducted at 12,000 RPM using a current of 40 A. However, the preparation of the first rod differed from that of the rest of the uranium rods. It was soaked overnight in a 50-50 solution of nitric acid and distilled water. By weighing the rod before and after the soak, it was determined that the rod had lost an equivalent of ~18 grams of material during the soak. It is likely that this amount of material could not be just oxidation and that the acid bath had leached some uranium from the rod. This hypothesis was supported by the rough surface texture of the rod following the acid bath, as well as the formation of what appeared to be pores on the faces of the rod. The left image in the figure below depicts the difference in appearance that the rod achieved after soaking by comparing it to an un-soaked, oxidized rod. The right image in the figure below depicts what appear to be pores that resulted after the acid bath. The acid bath also induced a striking color change in the rod, from an oxidized dull gray to a yellow-brown. It is hypothesized that the uranium within the rod reacted with the nitrogen in the acid bath to form a UN coating.
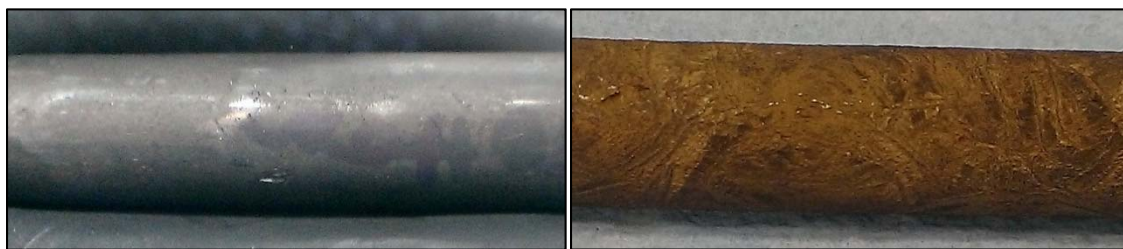

A depleted uranium rod before and after an overnight soak in a 50-50 nitric acid-water solution

Pore-like features introduced into the face of a uranium rod by prolonged nitric acid wash

It is likely that the combined effects of the pores, UN coating, and the mistake of not turning on the helium coolant during the test caused the rod to slump into the slag shape shown in the picture below rather than atomize during the first test of the RES. The test still produced powder, but had to be terminated shortly after beginning due to the destabilizing effects of the slag tip. It was concluded that acid washing the uranium rods was not a viable option for removing their surface oxidation.
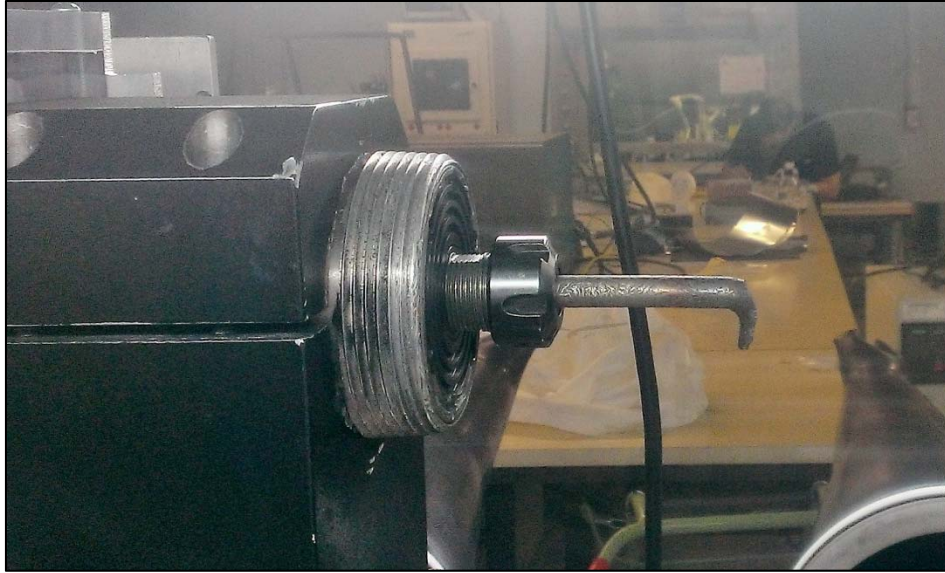
The result of first test of the RES, using an acid-soaked uranium rod